A Study of Hypergiant Mass Loss in the Near-To-Mid Infrared: VY CMa, IRC +10420, μ Cep and ρ Cas

A THESIS
SUBMITTED TO THE FACULTY OF THE GRADUATE SCHOOL
OF THE UNIVERSITY OF MINNESOTA
BY

Dinesh Prabhakar Shenoy

IN PARTIAL FULFILLMENT OF THE REQUIREMENTS
FOR THE DEGREE OF
Doctor of Philosopy

Advisor:
Terry Jay Jones

January, 2016

Acknowledgements

First and foremost I thank my advisors, Terry Jones, Robert Gehrz and Roberta Humphreys.

From Terry Jones I have learned a wealth of techniques, most particularly infrared polarimetry. Working on MMT-Pol has been among the most rewarding experiences in my graduate program, both for the science that is possible with polarimetry and the practical experience of commissioning, operating and upgrading the instrument. Terry helped me shape my approach to physical problems in practical ways. Many were the times that Terry helped me figure out the most direct approach to a problem, a skill that I have come to value highly.

I thank Bob Gehrz for giving me my first research and observing experience. Starting with analyzing Spitzer IRS spectra of old novae, he has included me in numerous research programs and collaborations, in particular the successful SOFIA target of opportunity program to observe novae. Flying on SOFIA to observe Nova Del 2013 was a once-in-a-lifetime opportunity. I am also grateful for the opportunity to learn observing at the Mt Lemmon Observing Facility (MLOF).

From Roberta Humphreys I have learned how very much I still have to learn about hypergiant stars. Time and again as I have prepared this thesis I find the current research referencing her foundational work on these unique objects. I am especially grateful for her support and guidance on navigating the peer review process, and for encouraging me to present my work at the ESO-STEPS conference in Garching.

I thank the past and current Minnesota Institute for Astrophysics graduate students, from whose collective wisdom I have undoubtedly gained far more than I have contributed in return. Equally key to my navigation through this program has been the steady support of the MIFA administrative staff. I thank Russell Penrose for his

generous fellowship, without which I could not have completed this thesis. With great sadness I posthumously thank Al Knutson for teaching me how to troubleshoot and repair the MLOF telescope and control system.

I thank everyone in the MMT-Pol team both past and present: Chris Packham (Co-PI), Enrique Lopez-Rodriguez, Megan Krejny, Craig Warner, Kathleen DeWahl, and Michael Gordon. I hope I contributed at least half as much to the MMT-Pol collaboration as I gained. I also thank the dedicated staff of the MMT Observatory and the Mt Lemmon summit support staff, for their patience and guidance in training this astronomer.

Dedication

I dedicate this thesis to my family, without which nothing in my life is possible.

Abstract

Stars of initial mass greater than 9 $M_{\odot}$ become red supergiants (RSGs), a short-lived stage during which they experience mass-loss that strongly influences their post-RSG evolution and end state. The highest luminosity RSGs, referred to here as hypergiants, experience episodic mass-loss whose mechanism remains poorly understood and motivates observations to help constrain it. This thesis studies mass loss from hypergiant stars with near-to-mid infrared imaging over a range of angular scales. The recent mass-loss history of the extreme red supergiant VY Canis Majoris and the warm hypergiant star IRC +10420 are studied at the sub-arcsecond scale with adaptive optics imaging and imaging polarimetry from $1 - 5$ μm using LMIRCam on the Large Binocular Telescope (LBT) and MMT-Pol at the MMT Observatory. The nebular features of VY CMa are found to be highly polarized at 1.3 and 3.1 μm, with optically thick scattering required to reproduce the observed surface brightness. The flux of VY CMa's peculiar "Southwest Clump" is demonstrated to be due almost entirely to optically thick scattering, with little thermal emission, and with a lower limit mass of 5×10^{-3} $M_{\odot}$ in this single feature. The imaging polarimetry of IRC +10420 at 2.2 μm resolves nebular emission with intrinsic polarization of 30%, with a high surface brightness indicating optically thick scattering largely in the plane of the sky. Using the polarimetry to constrain the scattered light emission, it is shown that the nebula's the emission is mostly thermal with a color temperature well above that for typical astrophysical dust.

To probe further into hypergiants' history of mass-loss, mid-IR imaging with MMT/MIRAC and SOFIA/FORCAST is used to study VY CMa, IRC +10420 and two additional hypergiants: the RSG μ Cep and the warm hypergiant ρ Cas. Using DUSTY 1-D radiative transfer models, μ Cep's mass-loss rate is found to have declined by about a factor of 5 over a 13,000 history, ranging from 5×10^{-6} down to $\sim 1 \times 10^{-6}$ $M_{\odot}$ yr^{-1}. The morphology of VY CMa indicates a cooler dust component coincident with the highly asymmetric reflection nebulae seen in the visual and near-IR. The lack of cold dust at greater distances around VY CMa indicates its mass-loss history is limited to the last $\sim$1200 years, with an average rate of 6×10^{-4} $M_{\odot}$ yr^{-1}. Two distinct periods are found in the mass-loss history of IRC +10420, with a high rate of 2×10^{-3} $M_{\odot}$

yr^{-1} until approximately 2000 yr ago, followed by an order of magnitude decrease in the recent past, with the change indicating its evolution beyond the RSG stage. The new infrared photometry of ρ Cas is consistent with emission from the expanding dust shell ejected in its 1946 eruption, with no evidence of newer dust formation from its more recent events.

Contents

Acknowledgements **i**

Dedication **iii**

Abstract **iv**

List of Tables **ix**

List of Figures **x**

1 Introduction **1**

2 Adaptive Optics Imaging of VY Canis Majoris at 2 - 5 micron with LBT/LMIRCam **4**

2.1 Introduction 5

2.2 Observations and Reduction 7

2.2.1 Observations 7

2.2.2 Reduction 8

2.2.3 Flux Calibration 9

2.3 Results 11

2.3.1 Comparison to Previous Observations 11

2.4 Analysis & Discussion 12

2.4.1 Subtraction of Central Star Flux 12

2.4.2 Constraint on Thermal Flux of the SW Clump 13

2.4.3 Scattered Light Flux of the SW Clump 16

2.4.4 SW Clump: Mass Lower Limit Estimate 19
2.4.5 Other Non-Detected Features 21
2.5 Conclusion & Future Work 21

3 Probing Hypergiant Mass Loss with Adaptive Optics Imaging & Polarimetry in the Infrared: MMT-Pol and LMIRCam observations of IRC +10420 & VY Canis Majoris 23
3.1 Introduction 24
3.2 Observations and Results 26
3.2.1 IRC +10420: 2.2 μm AO Imaging Polarimetry 26
3.2.2 IRC +10420: 3 - 5 μm AO Imaging 29
3.2.3 VY CMa: J$'$ (1.3 μm) and 3.1 μm Imaging Polarimetry 31
3.3 Analysis & Discussion 33
3.3.1 IRC +10420: Nebula's Intrinsic Polarization at K$'$ 33
3.3.2 VY CMa: Intrinsic Polarization of Nebular Features at J$'$ (1.3 μm) and 3.1 μm 37
3.3.3 Fractional Polarization versus Scattering Optical Depth 41
3.3.4 IRC +10420: Comparison of K$'$ Polarimetry with $3 - 5$ μm Images 43
3.4 Conclusions 47
3.5 Acknowledgements 49

4 Searching for Cool Dust in the Mid-to-Far Infrared: the Mass Loss Histories of The Hypergiants μ Cep, VY CMa, IRC+10420, and ρ Cas 50
4.1 Introduction 51
4.2 Observations and Data Reduction 52
4.2.1 SOFIA/FORCAST: Far-IR Imaging ($11 - 37$ μm) 52
4.2.2 MIRAC3/4: Adaptive Optics Mid-IR Imaging ($8 - 12$ μm) . . . 55
4.3 Results & Discussion 57
4.3.1 Method for Estimating Mass-Loss Rates 57
4.3.2 μ Cep 58
4.3.3 VY CMa 66
4.3.4 IRC +10420 71

4.3.5 ρ Cas 76
4.4 Summary & Conclusions 81
4.5 Acknowledgements 83

5 Summary & Future Work **85**

Appendix A. Additional MIRAC4 Observations **95**

List of Tables

3.1 MMT-Pol & LMIRCam Observations of IRC +10420 & VY CMa 27
3.2 Nebular Features' Intrinsic Polarization and Minimum Scattering Optical Depths 43
4.1 List of SOFIA FORCAST Observations 54
4.2 List of MMT/MIRAC Observations 56
4.3 DUSTY Model Inputs & Average Mass-Loss Rates 79

List of Figures

1.1 Upper End of HR Diagram 2
2.1 VY CMa: Early images of SW Clump. 6
2.2 VY CMa: LBT/LMIRCam $2 - 5$ μm adaptive optics images. 10
2.3 VY CMa: Subtracting star's flux from SW Clump. 14
2.4 VY CMa: Observed flux of SW Clump from $2 - 5$ μm. 17
2.5 VY CMa: Modeling SW Clump's brightness as diffuse reflection. 20
3.1 IRC +10420: MMT-Pol observations at $\lambda = \mathrm{K}'$ (2.2 μm). 30
3.2 IRC +10420: 3 - 5 μm adaptive optics images made with LBT / LMIRCam. 32
3.3 VY CMa: MMT-Pol observations at $\lambda = \mathrm{J}'$ (1.3 μm). 34
3.4 VY CMa: Comparison of *HST* 1 μm image and visual polarimetry with MMT-Pol J$'$ (1.3 μm) polarimetry. 35
3.5 VY CMa: MMT-Pol observations at $\lambda = 3.1$ μm. 35
3.6 IRC +10420: Estimating nebula's intrinsic polarization at K$'$ (2.2 μm). 38
3.7 VY CMa: Intrinsic polarization at 1.3 and 3.1 μm. 39
3.8 IRC +10420: Spectral energy distribution of nebula in near-IR. 48
4.1 μ Cep: Mid-IR high resolution AO images made with MIRAC3. 59
4.2 μ Cep: Far-IR SOFIA/FORCAST images. 61
4.3 μ Cep: *Herschel* PACS 70 μm image 62
4.4 μ Cep: Spectral Energy Distribution with DUSTY models. 64
4.5 μ Cep: Comparison of DUSTY model intensity profiles. 65
4.6 VY CMa: Far-IR SOFIA/FORCAST images. 67
4.7 VY CMa: Comparison of 37.1 μm contours with *HST* visual image. . . 68
4.8 VY CMa: Spectral Energy Distribution with DUSTY model. 70
4.9 IRC +10420: Mid-IR high resolution images with MIRAC4. 73

4.10 IRC +10420: Far-IR SOFIA/FORCAST images. 74
4.11 IRC +10420: Comparison of 37.1 μm contours with *HST* visual image. 74
4.12 IRC +10420: Spectral Energy Distribution with DUSTY models. 77
4.13 IRC +10420: DUSTY model intensity and density profiles. 78
4.14 ρ Cas: Far-IR SOFIA/FORCAST images. 80
4.15 ρ Cas: Spectral Energy Distribution with dust shell evolution. 82
A.1 MIRAC4 images of S Per. 97
A.2 MIRAC4 images of T Per. 98
A.3 MIRAC4 images of RW Cep. 99
A.4 MIRAC4 images of BD +24 3902. 100
A.5 MIRAC4 images of RW Cyg. 101
A.6 MIRAC4 images of ρ Cas. 102
A.7 MIRAC4 images of W Per. 103

Chapter 1

Introduction

Massive stars play an important role in the universe. They strongly influence the evolution of their host galaxies, shaping their nearby environments with their strong winds and enriching the interstellar medium with the products of their nucleosynthesis when they end in supernova explosions. As massive stars ($M_{ZAMS} > 9\ M_{\odot}$) evolve off the main sequence (MS) they pass through the red supergiant (RSG) stage, where they can shed a significant fraction of their initial mass. For some massive stars the RSG stage is the final state prior to becoming a supernova, while many will evolve beyond the RSG stage back to warmer temperatures, and are commonly called "yellow" supergiants (YSGs).

At the upper end of the Hertzsprung-Russell (HR) Diagram, a small number of YSGs and RSGs define an empirical upper limit of luminosity for warm and cool stars (Humphreys & Davidson, 1979). See Figure 1.1. These stars are referred to as hypergiants, both due to their very high luminosities (several $\times\ 10^5\ L_{\odot}$) and their large effective radii on the order of $\sim$10 AU. The end fate of such massive stars depends sensitively on several factors, in particular the mass-loss rate during the RSG stage (e.g., Meynet et al., 2015). Yet the mechanism for mass-loss during the RSG stage remains poorly understood, with pulsation, convection, and dust-driven winds advanced as explanations. In the case of hypergiants this problem is particularly acute since hypergiants exhibit episodes of high mass loss lasting decades, such as the 35+ year period of high mass loss by M33 Var A (Humphreys et al., 2006) and VY CMa (O'Gorman et al., 2015). Observations are thus key to constraining the mechanisms of hypergiant

mass-loss.

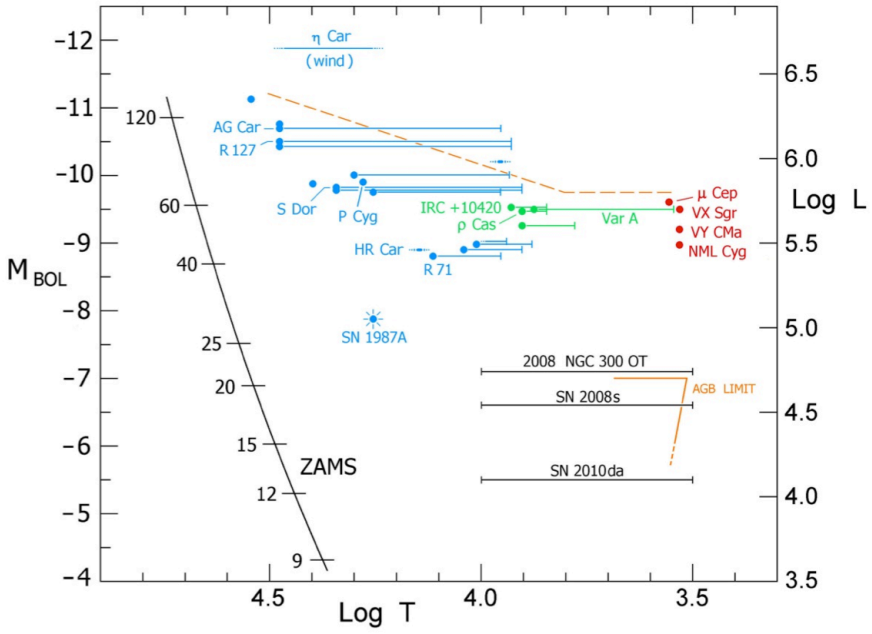

Figure 1.1 – Upper End of the Hertzsprung-Russell (HR) Diagram. The dashed gold line is the empirical limit on luminosity (Humphreys & Davidson, 1979). The cool (red) hypergiants VY CMa and μ Cep and the warm (green) hypergiants IRC +10420 and ρ Cas studied in this thesis are among the few stars that define this limit for effective temperatures below 10,000 K.

The study of hypergiants' mass loss has advanced across a range of wavelengths in recent decades. In the visual, space-based imaging with the *Hubble Space Telescope (HST)* has revealed episodic mass-loss around the famous hypergiants VY CMa and IRC +10420 at the sub-arcsecond level (Smith et al., 2001; Humphreys et al., 2007, 1997; Tiffany et al., 2010). As the ejected gas from oxygen-rich mass losing RSGs cools below $\sim$ 1000 K, it condenses and forms silicate dust. This circumstellar dust emits strongly in the near-to-mid infrared and the mapping of this dust probes the star's mass-loss history. The intensity profile of resolved emission from this dust combined with fitting of the star's spectral energy distribution (SED) may be used to trace the star's mass loss history.

In this thesis I present a study of hypergiant mass-loss in the near-to-mid infrared. In Chapter 2 I present our work using adaptive optics imaging to probe the mass-loss of

the cool hypergiant VY CMa at the sub-arcsecond scale in the 2 -5 μm range (Shenoy et al., 2013). Because evolved stars produce substantial amounts of dust, the spectrum of light from their resolved nebula is a combination of reflected (scattered) light and thermal emission. Therefore in Chapter 3 we combine the sub-arcsecond resolution achieved by adaptive optics with polarimetry at $1 - 3$ μm in studying the nebulae of both VY CMa and the warm hypergiant IRC +10420 (Shenoy et al., 2015). In Chapter 4 we use the new capability of NASA's airborne Stratospheric Observatory for Infrared Astronomy (SOFIA) search further into the past of both these famous hypergiants, as well the red supergiant μ Cephei and the yellow hypergiant ρ Cas (Shenoy et al., 2016, accepted by the Astronomical Journal). A summary and discussion of future work is provided in Chapter 5.

Chapter 2

Adaptive Optics Imaging of VY Canis Majoris at 2 - 5 micron with LBT/LMIRCam

This chapter has been published in the Astronomical Journal with the following bibiliographic reference: Shenoy, D. P., Jones, T. J., Humphreys, R. M., et al., 2013 AJ 146:90.

Abstract

We present adaptive optics images of the extreme red supergiant VY Canis Majoris in the K_s, L′ and M bands (2.15 to 4.8 μm) made with LMIRCam on the Large Binocular Telescope (LBT).[1] The peculiar "Southwest Clump" previously imaged from 1 to 2.2 μm appears prominently in all three filters. We find its brightness is due almost entirely to scattering, with the contribution of thermal emission limited to at most 25%. We model its brightness

[1] The LBT is an international collaboration among institutions in the United States, Italy and Germany. LBT Corporation partners are: The University of Arizona on behalf of the Arizona university system; Istituto Nazionale di Astrofisica, Italy; LBT Beteiligungsgesellschaft, Germany, representing the Max-Planck Society, the Astrophysical Institute Potsdam, and Heidelberg University; The Ohio State University, and The Research Corporation, on behalf of The University of Notre Dame, University of Minnesota and University of Virginia. We thank the LBT staff for their hard work and support of these observations.

as optically thick scattering from silicate dust grains using typical size distributions. We find a lower limit mass for this single feature of 5 $\times$ 10^{-3} $M_{\odot}$ to 2.5 $\times$ 10^{-2} $M_{\odot}$ depending on the assumed gas-to-dust ratio. The presence of the Clump as a distinct feature with no apparent counterpart on the other side of the star is suggestive of an ejection event from a localized region of the star and is consistent with VY CMa's history of asymmetric high mass loss events.

2.1 Introduction

The extreme red supergiant VY Canis Majoris is one of the brightest 5 - 20 μm stellar sources in the sky. Recent observations of SiO masers in its circumstellar envelope place it at a distance of 1.2 kpc using trigonometric parallax (Zhang et al., 2012), with L_{bol} = 2.7 $\times$ 10^5 $L_{\odot}$ (Wittkowski et al., 2012). Space-based observations with the *Hubble Space Telescope (HST)* from 0.4 to 1 μm have catalogued an extensive, highly structured nebula consisting of multiple arcs and knots of material ejected within the past ∼1000 years. This asymmetric nebula is indicative of multiple episodes of localized mass ejections from active regions on its surface (Smith et al., 2001; Humphreys et al., 2005, 2007). Ground-based adaptive optics imaging with the Large Binocular Telescope (LBT) enables us to extend the exploration of VY CMa's mass loss into the near-IR at an angular resolution greater than previous studies, e.g. Cruzalebes et al. (1998); Monnier et al. (1999).

Adaptive optics images of VY CMa made in 1994 with the COME-ON+ AO system at the ESO-La Silla 3.6m telescope found a "quasi-circular clump" of emission in the K-band at approximately 1″ to the southwest of the star (Cruzalebes et al., 1998)(see Figure 2.1a). J-band (1.25 μm) imaging in 1996-97 with the ADONIS SHARPII+ camera showed a similarly bright knot in the same position (Monnier et al., 1999). The clump of material was also observed at 1 μm in *HST* imaging in 1999 (Smith et al., 2001) (hereafter S01), and again in 2005 (Humphreys et al., 2007) (hereafter H07) as part of multi-epoch observations to map the morphology of VY CMa's nebula. S01 & H07 refer to it as the Southwest (SW) Clump (see Figure 2.1b).

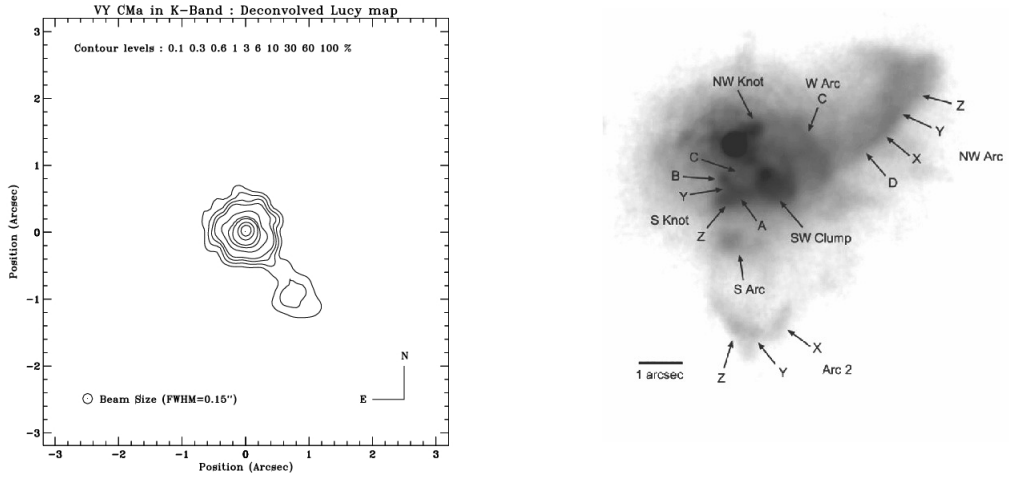

(a) (b)

Figure 2.1 – Early images of SW Clump. **(a):** K-band image of VY CMa from Figure 3 of Cruzalebes et al. (1998), taken in 1994 with the COME-ON+ AO system at the ESO-La Silla 3.6m telescope. The authors noted a "quasi-circular clump" located $\sim 1''$ to the southwest of the star. **(b):** 2005 *HST* F1042M (1 μm) image of VY CMa from Figure 4 of Humphreys et al. (2007), identifying the SW Clump as well as numerous other features of the ejecta. Several of the features at larger separations from the star than the SW Clump are potentially observable with LMIRCam.

Monnier et al. (1999) suggested the SW Clump might be component "B" that had been reported as a possible moving companion star by early observers. However, S01 noted that the SW Clump and another clump directly South were equally close to the position of "B" as reported by Herbig (1972). S01 could not unambiguously identify any of the structures in the HST images with the visual "companions" in the early observations. They concluded that the condensations or knots were either changing their structure and positions in only a few decades or that variable illumination was altering the appearance of the clumps (Wallerstein, 1978).

Combining slit spectroscopy from Humphreys et al. (2005) with the *HST* images across two epochs, H07 computed radial and transverse velocities of numerous components of the ejecta, including the SW Clump. Jones et al. (2007) used imaging polarimetry from the *HST* observations to locate the physical positions of several of the

features in the ejecta including the SW Clump, and independently confirmed the three-dimensional geometry of VY CMa's nebula. There is some ambiguity as to whether the SW Clump is a single feature or a superposed image of two distinct parts of the ejecta moving away from the star along different radial trajectories. H07 observed several knots of ejecta in the *HST* visual images at the same location as the SW Clump in the *HST* 1 μm images and determined them to be moving towards us. In their analysis H07 reasoned that since the SW Clump is highly obscured (appearing only at 1 μm, not in any of the *HST* WFPC2 visual filters), the more redshifted velocities from the slit spectroscopy applied to it. For VY CMa's distance of 1.2 kpc, H07's observations place the SW Clump on a trajectory inclined $+10^{\circ}$ behind the plane of the sky, moving at $\sim$ 14 km/s after having been ejected about 500 years ago.

2.2 Observations and Reduction

2.2.1 Observations

We observed VY CMa on UT 2011 November 16 with LMIRCam (Skrutskie et al., 2010)[2] using a single 8.4 m primary mirror on the Large Binocular Telescope (LBT). At the time of these observations LMIRCam used an HgCdTe array of 1024 $\times$ 1024 pixels, with a pixel scale of 0.011$''$ pix^{-1} for a field of view $\sim$ 11$''$ $\times$ 11$''$ (Leisenring et al., 2012). Images were made in the K_s ($\lambda_0 = 2.15$ μm), L$'$ ($\lambda_0 = 3.8$ μm) and M ($\lambda_0 = 4.8$ μm) filters.

To assess the point spread function and the orientation of the images, the binary star HD 37013 was observed in the L$'$ filter. The PSF exhibited astigmatism in the form of a "cross" pattern, which has been attributed to poor mounting of the dichroic (Rodigas et al., 2012). The LBT's first-light adaptive optics (AO) system (Esposito et al., 2012) provided near-diffraction-limited imaging, with the first minimum in the Airy disk pattern of the primary star in HD 37013 at L$'$ occuring at 0$''$.14 (compared to the theoretical minimum of 0$''$.11 computed from $\theta = 1.22\lambda/D$).

We imaged VY CMa at four dither positions on the array. Images at each dither position were taken in sets of 10 frames with 2.9 seconds per frame. The 2.9 second exposure time allowed fainter regions at greater than about 0$''$.5 from the star to be

[2] LMIRCam is funded by the National Science Foundation under grant NSF AST-0704992.

imaged at the expense of saturating closer to the star. Shorter length calibration exposures of 0.29 seconds were taken through a neutral density (ND) filter which attentuates the transmitted light by a factor of 100. These exposures provided unsaturated images of the star to use for flux calibrating ADUs, as well as for alignment of the saturated images. Nearby sky images were taken for both sets of exposure times for background subtraction.

2.2.2 Reduction

We examined the individual sets of ten frames obtained in each dither position, discarding frames in which it appeared that the AO lock had broken during an exposure. The remaining images were coadded to make a single image of VY CMa in each of the four dither positions. The nearby sky images were similarly coadded. Bad pixels were masked by mean combining dark images and masking pixels whose value deviated by $> 3\sigma$ from the median in the combined dark image. Masked pixels were replaced with the median value of the 8 surrounding pixels. We removed most of the sky background and offset level by subtracting the nearby sky images from each VY CMa image, matching filters and exposure times and selecting the sky image which had been taken closest in time. Subtracting pairs of dither positions to remove the background offset level and hot pixels was not possible because the angular extent of VY CMa's nebula is comparable to LMIRCam's $11'' \times 11''$ field of view. To bring the background of the four images in each filter (eight images in the M filter) closer to a mean value of zero, we subtracted the average of the sky background counts in four regions around VY CMa (separated from the star by several arcseconds).

LMIRCam was fixed to the telescope during the observations with the rotator turned off, resulting in the field of view rotating in the time between dithers. Therefore we rotated each dither position's image by the parallactic angle computed for the mean time of observation at that position. To verify the accuracy of the rotation, we applied the same calculation to the image of binary star HD 37013 that was observed on the same night. When rotated to take out the parallactic angle so that the image displays with North up and East to the left, the position angle of the SW Clump on the sky in each image agrees with the Clump's position in the *HST* 1 μm image. In the absence of any other identifying features in the images, final adjustment of the alignment of the

images across the three filters was done by sighting on the distinct triangular shape of the SW Clump itself and assuming it centers on the same position at all three wavelengths. With the images in each dither position aligned, the four dithered images (eight in the M filter) were coadded. We show our resulting images in the top row of Figure 2.2.

2.2.3 Flux Calibration

We used the shorter 0.29s exposures taken through the neutral density (ND) filter to flux calibrate the ADUs (counts) in the 2.9s images. We obtained background-subtracted counts of the star at K_s from aperture photometry on the ND images with the same $0\farcs4$ diameter aperture used by S01 on their 2.14 μm adaptive optics ADONIS/SHARP II+ images of VY CMa made with the ESO 3.6 m telescope. This aperture diameter equals $\sim 4\sigma$ of the star radial profile in the K_s ND image and thus encloses essentially all the flux of the star, as the same diameter did on the ESO images. The counts in this aperture were scaled to account for the difference in integration time and the attenuation by the ND filter. We cross-checked the accuracy of this scaling by comparing the average brightness of the SW Clump at M in the 2.9s images with its average brightness in the shorter exposures through the ND filter, where it is marginally visible. The scaled counts were calibrated to the upper-limit flux in W cm^{-2} at K_s attributed to the star by S01 (the thin solid curve below the total continuum curve at the top of Figure 2.4). To determine the flux of the star in counts in the L$'$ and M ND images, we selected aperture diameters to be 4σ of the star profile at each of those wavelengths, as was done at K_s. This ensured these apertures ($0\farcs49$ at L$'$ and $0\farcs63$ at M) enclosed the same fraction of total flux as the fraction enclosed at K_s. These counts were likewise scaled up and calibrated to the upper-limit fluxes in W cm^{-2} at L$'$ and M attributed to the star. Uncertainties in the calibration factors, estimated from the scatter in the total star counts from each of the 3 to 4 dithered images taken through the ND filter at each wavelength, are negligible in comparison to the uncertainty in the flux of the SW Clump as discussed in § 2.4.1.

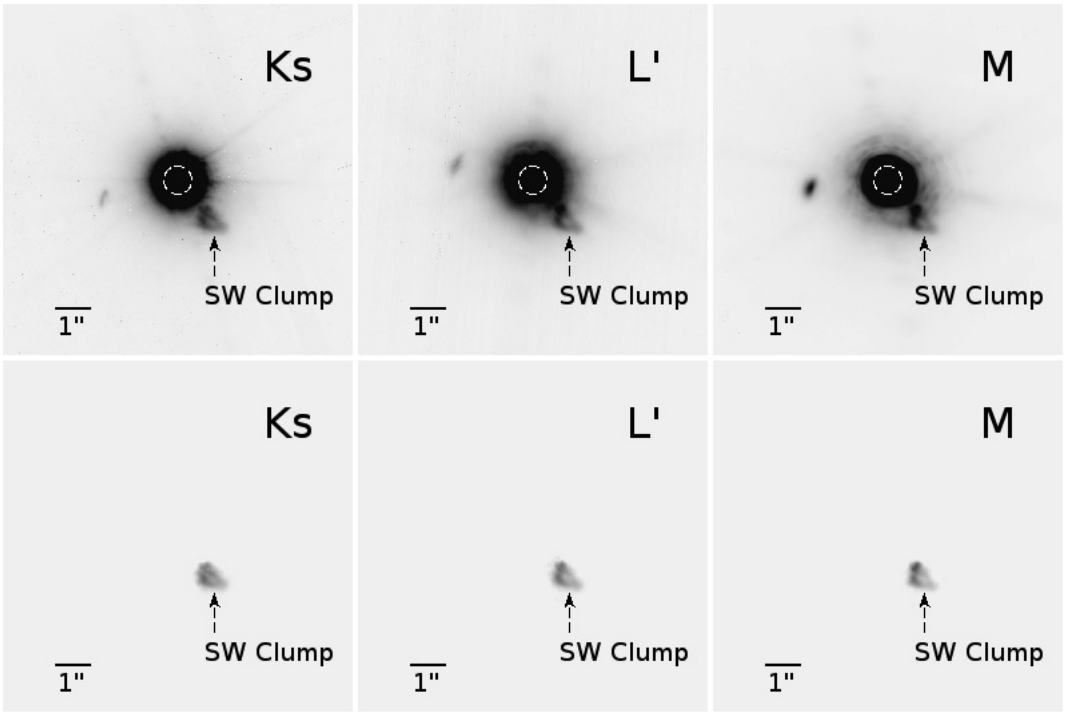

Figure 2.2 – LBT/LMIRCam $2 - 5$ μm adaptive optics images of VY CMa. **Top row**: VY CMa imaged with LMIRCam for 2.9s through the K_s filter ($\lambda_0 = 2.15$ μm), L$'$ filter ($\lambda_0 = 3.8$ μm) and M filter ($\lambda_0 = 4.8$ μm). Each image is a $10'' \times 10''$ FOV oriented North up, East left with linear greyscaling. The bar in the lower left of each image measures $1'' = 1200$ AU at a distance of 1.2 kpc. The beam size at L$'$ is $0\farcs12$ (measured FWHM of a point source). The dashed circle in the center indicates where the image is saturated out to a radius of $\sim 0\farcs4$ around the star. The SW Clump appears bright in all three filters. The patch of light appearing to the East of the star in each image is presumed to be from to an internal reflection rather than part of VY CMa's ejecta, due to its shifting positions relative to the star between dither positions and between filters. **Bottom row**: Images of SW Clump after subtracting a projected 2-D profile of the star's flux into the region covering the Clump (see § 2.4.1).

2.3 Results

2.3.1 Comparison to Previous Observations

The SW Clump appears bright in all three LMIRCam filters, measuring about 1″ across. Although its appearance overall is generally smooth, there is some variation in brightness across it. In all three filters the Clump appears somewhat dimmer in its center than at its edges (see Figure 2.2, bottom; see also the radial profiles in Figure 2.3). As noted earlier, H07 observed several knots at visible wavelengths which are in the same location as the SW Clump but which are moving towards instead of away from us. It is possible that the SW Clump as it appears in the LMIRCam filters is a projection of two distinct parts of VY CMa's ejecta which happen to lie along the same line of sight. On the other hand, J07 found the SW Clump to be a separate feature in their polarimetry map. In J07's polarimetry map the SW Clump was about 40% polarized, twice as polarized as the surrounding nebulosity. This suggested that the SW Clump is a distinct feature. In our analysis below we adopt the view that the SW Clump is a single feature observed moving along a trajectory inclined +10° behind the plane of the sky.

Four other features of VY CMa's ejecta identified in previous observations are located at angular separations from the star greater than that of the SW Clump and are therefore potentially observable with LMIRCam. These features were labeled by H07 as the NW Arc, the W Arc, the S Arc, and Arc 2 (see Figure 2.1b). The portions of Arc 2 which H07 designated as X, Y and Z are marginally observed in the LMIRCam K_s image (S/N $\sim$ 2-3). The portions of the NW Arc designated D, X, and Y are possibly visible in the K_s filter as well, but are extremely faint. We do not observe the S Arc and W Arc above the background level in the K_s image. None of these four features are observed in the L′ or M images.

Previous ground-based IR images at M, at 8.4 μm, and at 9.7 μm obtained by S01 with the TIMMI instrument at ESO-La Silla in 1996 appeared to show an axis of extended emission running east-west, with peaks at about 1″ from the star (their Figure 5.) While noting that these twin emission peaks could be accounted for with thermal emission from dust grains (using VY CMa's then-accepted distance of 1.5 kpc), S01 cautioned that the extended structure could be an artifact of defective PSF subtraction at those wavelengths. Our higher resolution M-band image with LMIRCam finds no

twin peaks of emission present at radii of 1″ to the east and west of the star.

2.4 Analysis & Discussion

2.4.1 Subtraction of Central Star Flux

To quantify the flux of the SW Clump relative to VY CMa's observed SED we first needed to remove the contribution of the star's flux in the region of the SW Clump. The proximity of the SW Clump to the star complicates this subtraction. Furthermore, at L′ the profile of the star's flux is not well represented by the PSF of either of the stars in the HD 37013 binary pair. The profile of the star's light at L′ is broader in the southeast and southwest than other directions, presumably due in part to emission from unresolved ejecta at less than 1″ from the star. At M the star's profile is similarly extended towards the southwest and would be poorly represented by scaling the PSF at L′.

We therefore used two alternate methods for subtracting the star's flux from the Clump, and took the average of the two methods as the Clump's flux for analysis. While the fluxes of the Clump from the two methods differ by as much as 50% at M, this difference between the two methods does not change our finding that the Clump's flux at M can be largely accounted for by scattered light alone.

In the first method, we created an azimuthal average of the radial profile of the central region containing the star in each filter. The range of azimuth covering the SW Clump (position angles from 200° to 230° E of N) was excluded from this average, as was the range containing the "ghost" in the East of the images that is assumed to be due to an internal reflection. We then rotated the profile of this azimuthal average to make a circularly symmetric image to represent the star's light and subtracted it from the image.

In the second method, we masked out the region containing the SW Clump and replaced it with a 2-D surface that approximates the shape of the star's 2-D profile into the region covering the Clump in each filter. The 2-D star profile surface was made using IDL's TRI_SURF routine, which uses linear interpolation to create a surface filling in the masked out region. We subtracted this projected image from the image in each filter. The subtracted images are displayed in the bottom row of Figure 2.2.

Figure 2.3 compares the two subtraction methods for a cut through the SW Clump. At each wavelength, subtracting the 2-D projected star profile (red dashed line) results in a lower flux from the Clump than subtracting the azimuthally averaged star profile (blue dashed line). At K_s and L' the 2-D projected star profile provides a better match to the likely profile of the star in the region of the Clump, though it may slightly oversubtract at radii close to the star. The difference in the flux of the SW Clump at K_s and L' for the two methods is $\sim 20\%$. At M the azimuthally averaged star profile is substantially lower than the likely profile of the star in the region of the Clump, which the 2-D projected star profile follows more closely. The difference in the flux of the SW Clump measured from the two methods is $\sim 50\%$ at M.

While these differences may be substantial, they do not affect our conclusion that the Clump's brightness can be accounted for largely with scattered light alone. For the following analysis of the SW Clump we adopt the average flux from the two star subtraction methods. In Figure 2.4 we plot the flux of the SW Clump from the average of the two subtraction methods on VY CMa's SED. As a check on our calculation, we compared our flux values with those obtained by S01 from their lower resolution ADONIS/SHARP II+ ESO image of VY CMa at 2.14 μm. Our flux-calibrated average brightness of the SW Clump from the LMIRcam K_s image agrees to within a factor of 2-3 with the surface brightness at the matching location of the SW Clump in the ESO images.

2.4.2 Constraint on Thermal Flux of the SW Clump

LMIRCam's K_s, L' and M filters sample the wavelength range where emission from dust grains may be due to either scattering, thermal emission, or a combination of both. Over most of the likely range of the Clump's temperature, we find that thermal emission contributes negligibly to its flux in all three filters. This conclusion is driven by two factors: the very bright fluxes at K_s and L' which are due to scattered light, and the far-IR flux of the entire system, which constrains the thermal contribution from the Clump.

We determine an upper limit on the grains' thermal flux by assuming them to be silicates and computing their equilibrium temperature T_{eq} for their distance d from the star. In computing T_{eq}, we include the grains' wavelength dependent absorption

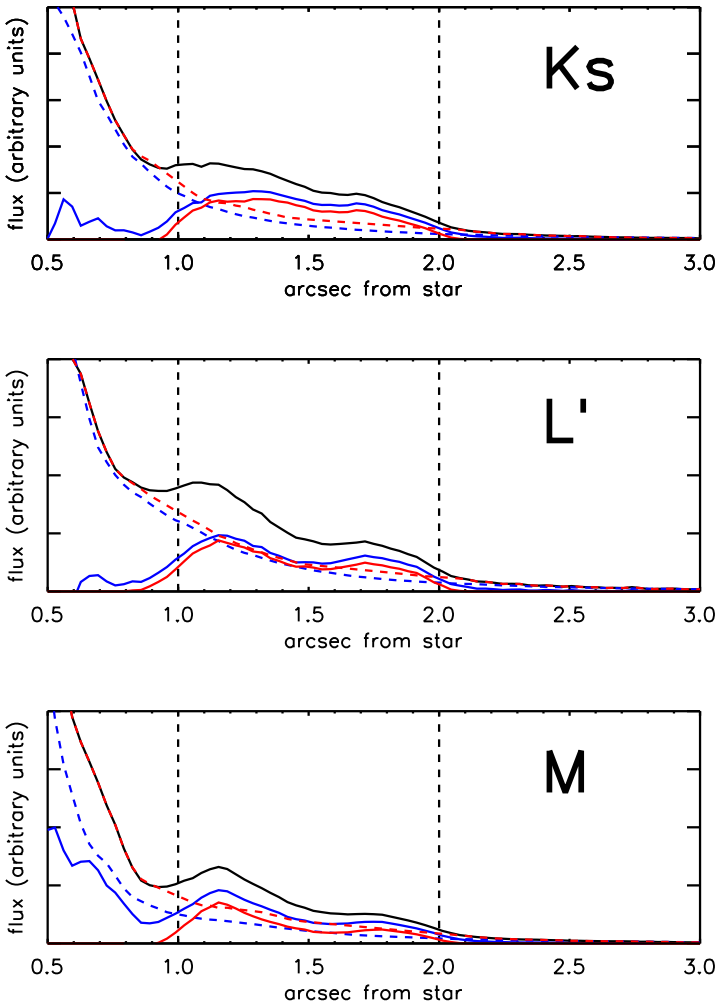

Figure 2.3 – Subtracting star's flux from SW Clump. The dashed vertical black lines mark the radial range in which the Clump appears. The solid black curve is the radial profile of the image (star and SW Clump combined). The dashed blue curve is the profile of an azimuthal average of the combined image. The solid blue curve is the profile of the combined image minus the azimuthal average image. The dashed red curve is the profile of a linearly interpolated surface that projects the star's light into the region containing the SW Clump. The solid red curve is the profile of the combined image minus the 2-D projected image. Subtracting the 2-D projected image yields an integrated flux of the SW Clump which is $\sim 20\%$ lower at K_s and L', and is $\sim 50\%$ lower at M, as compared to the Clump's flux when subtracting the azimuthal average image.

efficiency $Q_{abs}(\lambda)$ when balancing the power from the star absorbed by a grain with the power emitted by the grain. We use $Q_{abs}(\lambda)$ for silicate grains of mean radius $\overline{a} = 0.3$ μm, which is a typical size for circumstellar environments (see § 2.4.3). Parts of the Clump could be at distances varying as much as from 1200 AU to 2400 AU from the star, corresponding to equilibrium temperatures from 170 K down to 130 K. A distance measured to the middle of the face of the Clump puts it at roughly $d = 1\farcs4 = 1600$ AU from the star. For this average distance the grains' equilibrium temperature is $T_{eq} =$ 150 K. This is slightly higher than the blackbody equilibrium temperature of 140 K at $d = 1600$ AU since $Q_{abs}(\lambda) < 1$ makes the grains less-than-ideal radiators. Including $Q_{abs}(\lambda)$ does not raise their equilibrium temperature much, however. If the grains were subjected to the flux of a star whose SED peaked in the visible where $Q_{abs}(\lambda)$ is closer to 1, they might reach a higher equilibrium temperature than 150 K. Varying $\overline{a}$ over a reasonable range changes Q_{abs} somewhat, but the resulting T_{eq} is essentially the same.

Given the complexity of VY CMa's circumstellar environment, the temperature of the dust grains may lie within a wider range than the 130 K to 170 K obtained from simply placing grains in clear sight of the star and having them freely re-emitting into space. In the 8.4 and 9.8 μm images obtained by S01 the respective brightnesses at the location of the SW Clump yield a color temperature of 210 K (their Figure 5). In view of our finding further below that the fluxes at K_s and L' are dominated by scattered light and given that the star's SED continues to rise from K_s through ~ 8 μm, the infrared color at 8.4 μm must include a significant scattered light component. If the 8.4 μm brightness is partly due to scattered light, that would lower the $S_{8.4}/S_{9.8}$ color temperature at the Clump's location to below 210 K, though it might still be higher than 150 K.

The grains could be cooler than $T_{eq} = 150$ K as well. Recent millimeter wavelength observations of VY CMa's molecular emission have been used to derive gas temperatures which, at the SW Clump's distance from the star, range from 150 K down to as low as 80 K (Muller et al., 2007; Fu et al., 2012). Grains with temperatures as cold as 80 K cannot contribute to the Clump's observed flux in the M filter because the extrapolated flux at longer wavelengths would far exceed what is observed for the entire system. For completeness we consider the impact of a grain temperature between 80 K to 210 K on the Clump's observed flux at M.

The contribution of thermal flux to the Clump's brightness in the M filter is constrained by the grains' temperature as well as by the wavelength at which the Clump becomes optically thin in emission. For temperatures from 80 K to 210 K the Clump's $B_\lambda(T_{eq})$ thermal spectrum rises through the M filter to a peak at a longer wavelength. This thermal spectrum cannot exceed VY CMa's observed far-IR spectrum, which was measured out to 200 μm by ISO (Harwit et al., 2001). In the next subsection we find that the Clump is optically thick at K_s, L$'$ and M. If the Clump becomes optically thinner in emission at longer wavelengths, the spectrum of its thermal emission would be reduced to $(1 - e^{-\tau_{abs}(\lambda)}) \cdot B_\lambda(T_{eq})$ at those longer wavelengths. Depending on the wavelength at which this transition occurs, this permits a higher thermal flux at M without exceeding VY CMa's far-IR SED.

To keep it simple, consider the transition to occur when the absorption optical depth τ_{abs} drops by a factor of 2, with the scaling given by: $\tau_{abs}(\lambda) = \tau_{abs}(M) \cdot Q_{abs}(\lambda)/Q_{abs}(M)$. For our grain parameters we find this transition occurs at $\lambda \approx 45$ μm. In Figure 2.4 we plot two $\lambda B_\lambda(T_{eq})$ curves for thermal emission that is optically thick out to this wavelength. One curve is for our adopted value of $T_{eq} = 150$ K (dotted line) and the other is for the upper end $T_{eq} = 210$ K (dot-dashed line). Ignoring any contribution from the rest of VY CMa's nebula to the flux at 45 μm, these curves constrain the maximum thermal flux from the Clump at M for each of these temperatures. For $T_{eq} = 150$ K the thermal flux at M would be only 0.2% of the Clump's observed flux at M. For the upper end $T_{eq} = 210$ K the thermal flux at M would optimistically be 25% of the Clump's observed flux at M. Thus even if the Clump's total extinction optical depth at M is no greater than order unity, three-quarters of its flux must be attributed to non-thermal emission, i.e., to scattered light.

2.4.3 Scattered Light Flux of the SW Clump

In modeling the brightness of the Clump as due to scattering, we first consider the possibility that the Clump is optically thin at K_s, L$'$ and/or M. Surface brightness at a given wavelength due to optically thin scattering may be computed with

$$S_\lambda = \frac{\omega \tau_{ext} F_\lambda^\star \sin^2\theta}{4\pi\phi^2} \Phi(\theta, \lambda) \tag{2.1}$$

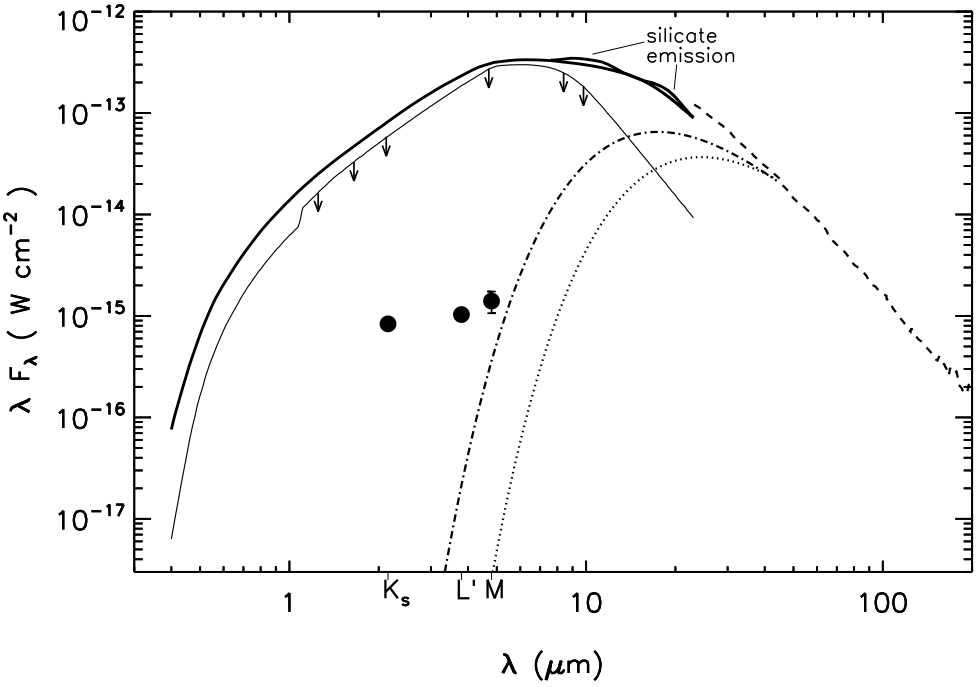

Figure 2.4 – Observed flux of SW Clump in LMIRCam filters, plotted on the spectral energy distribution of VY CMa. The solid thick curve at the top is the total continuum flux of VY CMa (the star and nebula combined) from the *HST* and ground-based photometry by Smith et al. (2001) (S01). The thin solid line below it indicates the flux which S01 attributed to the star/inner dust shell, which are upper limits at IR wavelengths due to limits in spatial resolution. The discontinuity in the star's flux at $\sim$ 1 μm resulted from the different aperture sizes used by S01 to measure the flux of the star, corresponding to the difference in resolution between their *HST* and ground-based observations. The dashed line from 23 μm to 200 μm is a portion of the ISO spectrum of VY CMa from Harwit et al. (2001). The discontinuity in VY CMa's continuum flux at 23 μm (a factor of $\sim$ 1.4) may be due ISO's larger beam size. The solid circles are the flux of the SW Clump in the LMIRCam K_s, L', and M filters (this work). The uncertainty in its flux in each filter is taken to be the difference of the two methods of star flux subtraction discussed in § 2.4.1. The uncertainty in its flux at K_s and L' is smaller than the plotted circle. The dotted curve is a $\lambda B_\lambda(T_{eq})$ thermal emission spectrum for grains at T_{eq} = 150 K, the temperature we adopt for grains in the SW Clump. The dot-dash curve is for an upper limit temperature of T_{eq} = 210 K. The thermal emission curves are plotted out to λ = 45 μm, the wavelength through which VY CMa's far-IR spectrum constrains the contribution of thermal emission to the Clump's observed flux (see § 2.4.2). For even the upper limit temperature of T_{eq} = 210 K, three-quarters of the Clump's flux at M must be due to non-thermal emission.

where $\omega\tau_{ext} = \tau_{sc}$ is the scattering optical depth at λ, $F^{\star}_{\lambda}$ is the flux of the star at λ, θ is the scattering angle, $\Phi(\theta, \lambda)$ is a wavelength-dependent phase function accounting for the variation with θ of the intensity of scattered light from silicate spheres, and ϕ is the angular distance between the star and a position on the Clump (Sellgren et al., 1992). Taking $\tau_{sc} \lesssim 0.2$ as a reasonable upper limit for being optically thin, we find the brightness across the SW Clump is an order of magnitude brighter at K_s than can be explained by optically thin scattering. At L' and M as well the Clump is brighter than optically thin scattering of the star's light can account for, even at the Clump's upper limit temperature of $T_{eq} = 210$ K for which thermal emission would supply a quarter of its brightness at M.

We adopt the view that the SW Clump is moving away from the star and behind the plane of the sky. We may therefore treat it as a plane parallel atmosphere whose surface brightness arises from optically thick scattering (diffuse reflection). Surface brightness at a given wavelength due to diffuse reflection from a plane parallel atmosphere may be expressed as:

$$S_{\lambda} = \frac{\overline{\omega_0}(\lambda) F^{\star}_{\lambda} \sin^2\theta}{4\pi\phi^2} \left(\frac{\mu_0}{\mu + \mu_0} \right) H(\mu) H(\mu_0) \tag{2.2}$$

where $\overline{\omega_0}(\lambda)$ is the particles' single scattering albedo at λ, $F^{\star}_{\lambda}$, θ and ϕ are the same as in the previous equation, μ_0 and μ are respectively the direction cosines of the incident and reflected beams measured from the normal to the plane parallel atmosphere, and the H terms are numerically integrated functions whose value range from 1 up to $\sim$3 for increasing μ and albedo (Chandrasekhar, 1950). The angles of the incident and reflected beams of light in/out of the Clump are assumed to be equal ($\mu_0 = \mu = \cos 40^{\circ}$, based on the inclination of the Clump's trajectory at $+10^{\circ}$ behind the plane of the sky.)

We idealize the grains to be silicate spheres of radius a, with the distribution of grain radii following either a power law distribution $n(a)da \propto a^{-p}da$, or a Gaussian distribution with mean radius $\overline{a}$ and standard deviation σ_a. Using the BHMIE subroutine[3] of Bohren & Huffman (1983), we compute the grains' extinction and scattering efficiencies numerically from Mie theory using optical constants $n(\lambda)$ and $k(\lambda)$ taken from the literature, and then compute the albedo with $\overline{\omega_0}(\lambda) = Q_{sc}(\lambda)/Q_{ext}(\lambda)$. The optical constants n and k are the wavelength-dependent real and imaginary parts of

[3] http://www.met.tamu.edu/class/atmo689-lc/bhmie.pro

silicates' complex index of refraction $m(\lambda) = n + ik$. With the computed albedo $\overline{\omega_0}(\lambda)$ for a chosen power law or Gaussian distribution we compute a model SED of the SW Clump at each wavelength using Equation (2). This model SED is then scaled to fit the observed flux of the Clump at either K_s and/or M.

In Figure 2.5 we have plotted examples of these diffuse reflection SEDs fitted to the Clump's observed flux at either K_s and/or M for selected power law and Gaussian distributions of the grain radii. Using optical constants $n(\lambda)$ and $k(\lambda)$ for "astronomical" silicates from Draine (2003) we can fit the flux at K_s or at M with power law and Gaussian size distributions, but not at both wavelengths (Figure 2.5, top). We obtain a better fit when using the optical constants $n(\lambda)$ and $k(\lambda)$ computed by Suh (1999) for silicate grains in the dusty envelopes around AGB stars. With these constants we can fit the Clump's flux at both K_s and M using a single power law or single Gaussian size distribution, for both of which $\overline{a} \approx 0.3$ μm (Figure 2.5, bottom). For the high-end $T_{eq} = 210$ K at which thermal flux would supply a quarter of the total observed flux at M, a slightly tighter grain size distribution fits the lowered diffuse reflection flux at M. The difference in size distributions is minor and the mean radius remains $\overline{a} \approx 0.3$ μm. In all cases fitting a diffuse reflection SED to the flux at M within the range of its uncertainty results in overpredicting the flux at L$'$. Nonetheless, the reasonably good agreement between the predicted diffuse reflection fluxes for these typical grain sizes and the observed flux at K_s and M indicates that the Clump's brightness in all three filters is due largely or solely to scattered light.

2.4.4 SW Clump: Mass Lower Limit Estimate

We compute a lower limit estimate of the mass of the SW Clump by multiplying the mass of a spherical dust grain of average radius $\overline{a}$ with a lower limit number N of grains in the Clump. The number N of grains in the Clump is at least the ratio of the total flux of the Clump at K_s to the flux of scattered light from a single spherical grain with effective cross-section $Q_{sc}(K_s) \cdot \pi\overline{a}^2$. For a power law distribution of grain sizes which produces the dotted curve in the bottom plot of Figure 2.5, the average grain radius is $\overline{a}$ = 0.28 μm and the scattering efficiency of the distribution is $Q_{sc}(K_s) = 0.64$. Assuming a gas-to-dust mass ratio of 100:1 (e.g., Knapp et al. (1993)) and a typical silicate mass density of $\rho = 3$ gm cm^{-3}, we find the Clump's mass to have a lower limit of $M \gtrsim$

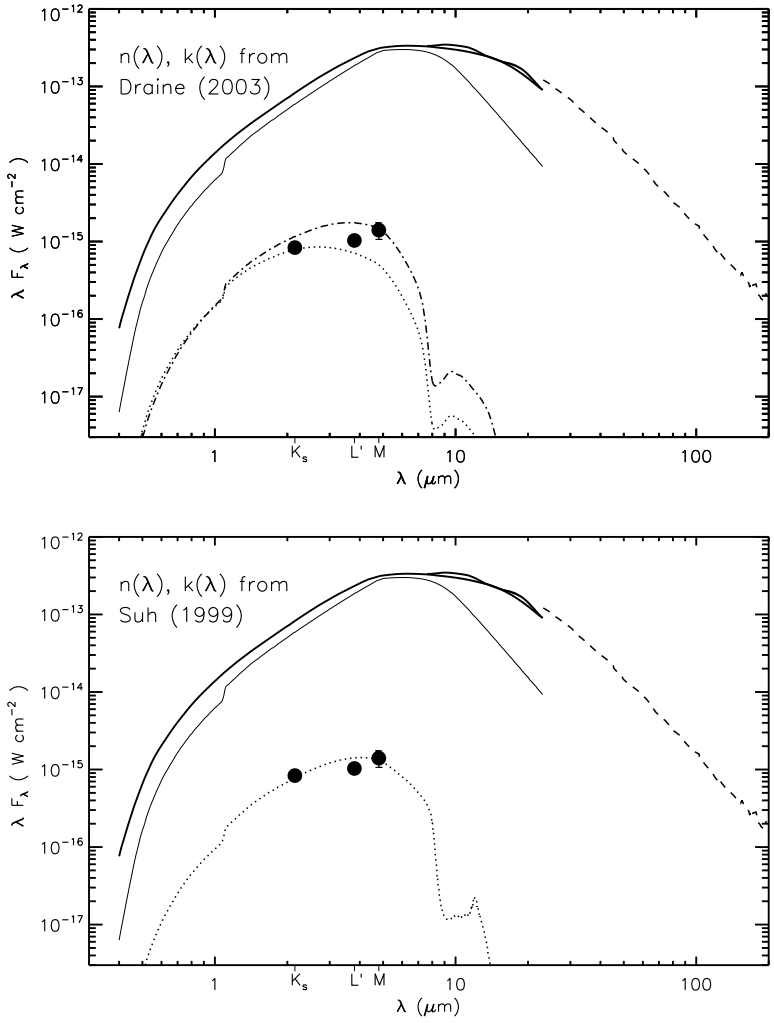

Figure 2.5 – Modeling SW Clump's brightness as diffuse reflection from silicate grains with a distribution of radii. *Top:* Models using "astronomical silicate" optical constants $n(\lambda), k(\lambda)$ from Draine (2003) for power law distributions with index $p = -3.0$. Minimum and maximum radii for the distributions have been chosen to fit the Clump's K_s flux (dotted curve) and M flux (dash-dotted curve). For these n, k no distribution was found which fit the flux at both K_s and M. *Bottom:* Model using $n(\lambda)$ and $k(\lambda)$ from Suh (1999) for silicate grains in the dust shells of AGB stars. A power law distribution of grain radii with index $p = -3.0$ over the range $a_{min} = 0.2$ μm to $a_{max} = 0.5$ μm is able to fit the Clump's at both K_s and M (dotted curve). For both sets of optical constants, Gaussian distributions of the grain radii with mean radius $\overline{a} \approx 0.3$ μm are able to produce essentially the same results.

5×10^{-3} $M_{\odot}$. If we assume the 500:1 gas-to-dust mass ratio found by Decin et al. (2006) for VY CMa, this lower limit increases to 2.5×10^{-2} $M_{\odot}$. We emphasize that these are only lower limits on the Clump's mass; since the Clump is optically thick, its total mass is higher. Compared to VY CMa's normal mass loss rate of $\sim 10^{-4}$ $M_{\odot}$ yr^{-1}, such a large mass in a single distinct feature is strongly indicative of an event involving ejection from a localized region of the star.

2.4.5 Other Non-Detected Features

As noted above, the feature designated as the S Arc by H07 is not detected in the K_s image. This places an upper limit of ~ 0.06 for its scattering optical depth at K_s. Portions of the feature designated Arc 2 are marginally visible above the noise level at K_s. Their brightness corresponds to an optical depth no greater than about 0.2. These optical depths are consistent with J07's finding these portions of Arc 2 to be optically thin in the visible. In future observations, longer integration times might be able to detect scattered light emission from these features.

2.5 Conclusion & Future Work

The *HST* images of VY CMa made by S01 and H07 found the SW Clump to be completely obscured at visible wavelengths, emerging only at 1 μm. If the SW Clump were the product of a bipolar outflow with a similar feature opposite it in the heavily obscured region to the northeast of the star, such a feature would be more likley to appear in LMIRCam's K_s, L$'$ or M filters. The absence of any obvious feature in the northeast opposite the Clump is consistent with VY CMa exhibiting a history of localized mass ejections from active regions on its surface, regions which are not strongly aligned with a presumed axis or equator. H07 argued that the many features of VY CMa's ejecta may be the result of localized activity on the star related to convection and magnetic fields. The distinct shape of the SW Clump is suggestive of a short-lived, localized event and may be analogous to a coronal mass ejection (CME) from a single location on the Sun's surface. A short-lived ejection event is consistent with the SW Clump appearing as a confined, coherent shape several hundred years after ejection. Adaptive optics imaging at wavelengths longer than 5 micron such as with NOMIC (8 - 25 μm camera on the

LBT, (Hinz et al., 2012)) would better constrain the SED of the SW Clump and confirm whether its brightness at longer wavelengths is due to scattered light alone.

Chapter 3

Probing Hypergiant Mass Loss with Adaptive Optics Imaging & Polarimetry in the Infrared: MMT-Pol and LMIRCam observations of IRC +10420 & VY Canis Majoris

This chapter has been published in the Astronomical Journal with the following bibiliographic reference: Shenoy, D. P., Jones, T. J., Packham, C., & Lopez-Rodriguez, Enrique, 2015 AJ 150:15.

Abstract

We present $2 - 5$ μm adaptive optics (AO) imaging and polarimetry of the famous hypergiant stars IRC +10420 and VY Canis Majoris. The imaging

polarimetry of IRC +10420 with MMT-Pol[1] at 2.2 μm resolves nebular emission with intrinsic polarization of 30%, with a high surface brightness indicating optically thick scattering. The relatively uniform distribution of this polarized emission both radially and azimuthally around the star confirms previous studies that place the scattering dust largely in the plane of the sky. Using constraints on scattered light consistent with the polarimetry at 2.2 μm, extrapolation to wavelengths in the $3-5$ μm band predicts a scattered light component significantly below the nebular flux that is observed in our LBT/LMIRCam $3-5$ μm AO imaging. Under the assumption this excess emission is thermal, we find a color temperature of $\sim$ 500 K is required, well in excess of the emissivity-modified equilibrium temperature for typical astrophysical dust. The nebular features of VY CMa are found to be highly polarized (up to 60%) at 1.3 μm, again with optically thick scattering required to reproduce the observed surface brightness. This star's peculiar nebular feature dubbed the "Southwest Clump" is clearly detected in the 3.1 μm polarimetry as well, which, unlike IRC+10420, is consistent with scattered light alone. The high intrinsic polarizations of both hypergiants' nebulae are compatible with optically thick scattering for typical dust around evolved dusty stars, where the depolarizing effect of multiple scatters is mitigated by the grains' low albedos.

3.1 Introduction

Hypergiant stars are located near the upper limit of luminosity in the HR Diagram, with typical luminosities of $L_\star \sim 5 \times 10^5$ $L_\odot$ and effective photosphere radii of several AUs. They exhibit very high mass loss rates of as much as 10^{-4} $M_\odot$ yr^{-1} (Danchi et al., 1994) with some experiencing even greater discrete eruptions. Here we present new adaptive optics (AO) infrared observations of two famous hypergiant stars IRC +10420 and VY Canis Majoris.

[1] Observations reported here were obtained at the MMT Observatory, a joint facility of the Smithsonian Institution and the University of Arizona.

IRC +10420 is a yellow hypergiant, in the rare short-lived evolutionary stage experienced by massive stars transiting to or from the red supergiant stage. *Hubble Space Telescope (HST)* visual imaging revealed a very complex circumstellar nebula with numerous condensations arrayed in jet-like structures, rays and arcs (Humphreys et al., 1997). *HST* long-slit spectroscopy (Humphreys et al., 2002) combined with second epoch *HST* imaging found that we view the star nearly pole-on, looking down on its equatorial plane (Tiffany et al., 2010). Recent VLTI observations of neutral and ionized gas around IRC +10420 have confirmed this geometry (Oudmaijer & de Wit, 2013).

VY CMa is a cool, red hypergiant. Multi-epoch *HST* imaging and polarimetry found extensive episodic mass loss with no preferred axis of symmetry (Humphreys et al., 2007; Jones et al., 2007). Ground-based 2 - 5 μm AO imaging with LMIRCam (Skrutskie et al., 2010) on the Large Binocular Telescope (LBT)[2] previously reported by Shenoy et al. (2013) found VY CMa's peculiar "Southwest Clump" to be a particularly dense, optically thick condensation of the ejecta. Most recently, ALMA sub-millimeter observations have found further discrete, dense ejecta in the very close environment of the star (Richards et al., 2014; O'Gorman et al., 2015). The mechanisms for such discrete mass loss are not understood. Magnetic field activity analogous to coronal mass ejections may be responsible (Humphreys et al., 2007). Although recent $XMM-Newton$ X-ray observations of VY CMa placed constrains on the magnetic field strength at the star's surface, the star may have simply been in state of lower magnetic activity than during previous mass loss events (Montez et al., 2015).

Because of the high contrast ratio between the star's light profile and the surface brightness of nebular material, separating infrared nebular emission from the star presents considerable difficulty. Imaging polarimetry is a powerful technique for studying nebular emission in this regime. Dust in the nebula scatters light from the star and polarizes it. If the star's light is unpolarized or weakly polarized compared to the fractional polarization of the scattered star light, then imaging polarimetry can cleanly separate the faint polarized light from the star's dominating light. We present new

[2] The LBT is an international collaboration among institutions in the United States, Italy and Germany. LBT Corporation partners are: The University of Arizona on behalf of the Arizona university system; Istituto Nazionale di Astrofisica, Italy; LBT Beteiligungsgesellschaft, Germany, representing the Max-Planck Society, the Astrophysical Institute Potsdam, and Heidelberg University; The Ohio State University, and The Research Corporation, on behalf of The University of Notre Dame, University of Minnesota and University of Virginia.

observations of these two hypergiant stars made with MMT-Pol, the $1 - 5$ μm imaging polarimeter custom designed for the 6.5 m MMT observatory on Mt. Hopkins (Packham et al., 2012) and with LBT/LMIRCam on Mt. Graham, AZ . The observations are summarized in Table 3.1.

3.2 Observations and Results

3.2.1 IRC +10420: 2.2 μm AO Imaging Polarimetry

We observed IRC +10420 on 2012 Sep 26 (UT) with MMT-Pol (Packham et al., 2012) during its commissioning run. MMT-Pol operates at the Cassegrain focus, where the AO-corrected beam from the secondary mirror enters the instrument with no prior off-axis reflections that might introduce spurious polarization. A rectangular mask in the focal plane provides a $20'' \times 40''$ field of view. The beam passes through a half-wave retarder (or half-wave plate, hereafter HWP), after which a Wollaston prism splits the light into orthogonal components. These two components are referred to as the ordinary and extraordinary rays, or o and e rays. Rotating the HWP from 0° to 45° swaps the o and e rays. Comparison of the two rays allows Stokes parameter Q to be extracted while canceling out any differences in throughput between the two rays and/or differences in detector response where the rays are detected. Similarly, rotating the HWP from 22.5° to 67.5° yields Stokes parameter U. MMT-Pol's pixel scale is $0.043''$ pix^{-1}.

We imaged IRC +10420 through the K$'$ ($\lambda_0 = 2.20$ μm, $\Delta\lambda = 0.12$ μm) filter at two dithered positions separated by $20''$ on the detector array. At each dither position images were taken as correlated double-sample (CDS) pairs, with the subtracted difference of each CDS pair yielding a single 1.33 s exposure. For each HWP position angle 50 exposures were taken. For image quality and flux calibration, a polarized standard star (HD 29333) and unpolarized standard star (HD 224467) were observed. The FWHM of the PSF was $0.2''$. The flux calibration factors (ADUs to W cm^{-2}) computed using these two standards agree to within 5%. The instrumental polarization determined from the unpolarized standard star was $0.47\% \pm 0.07\%$.

Each 1.33 s exposure was examined individually. On occasion when an increase in the width of the star profile indicated potential loss of AO lock, those exposures were discarded. The remaining useable frames were mean combined to yield a single image in

Table 3.1 – MMT-Pol & LMIRCam Observations of IRC +10420 & VY CMa

Date (UT)	Instrument	Filter(s) (μm)	On-Source Time (s)
		IRC +10420	
2011 May 25	LMIRCam	PAH1 (3.29)	186
		PAH2 (3.40)	220
		L′ (3.83)	154
		M (4.9)	107
2012 Sep 25	MMT-Pol	K′ (2.2)	254
		VY CMa	
2013 Oct 22	MMT-Pol	J′ (1.3)	36
2014 Jan 16		J′ (3.1)	320

each HWP position for each of the two dithers. The sky background and array structure were removed by subtracting dithered images; this subtraction removed many hot pixels as well. Remaining hot pixels were replaced with the median of the surrounding 8 pixels. The *o*-ray and *e*-ray images were extracted from these images. The central point source of IRC +10420 in each exposure saturates the images out to a radius of $\lesssim 0.4''$. For each dither position, the 8 images (2 per HWP position) were aligned using the IRAF[3] XREGISTER task. The images were then smoothed with a Gaussian of FWHM = $0.2''$ (the beam size as estimated from the PSF star).

The normalized Stokes parameters $q \equiv Q/I$ and $u \equiv U/I$ were computed using the

[3] IRAF is distributed by the National Optical Astronomy Observatory, which is operated by the Association of Universities for Research in Astronomy (AURA) under cooperative agreement with the National Science Foundation.

ratio method of Tinbergen (1996):

$$q = \frac{R_q - 1}{R_q + 1} \text{ , for } R_q \equiv \sqrt{\frac{I^o_{00}/I^e_{00}}{I^o_{45}/I^e_{45}}} \tag{3.1}$$

$$u = \frac{R_u - 1}{R_u + 1} \text{ , for } R_u \equiv \sqrt{\frac{I^o_{22}/I^e_{22}}{I^o_{67}/I^e_{67}}} \tag{3.2}$$

where the o and e superscripts on each of the intensities I refer to the ordinary and extraordinary rays emerging from the Wollaston prism, and the subscripts refer to the four HWP orientation angles 00.0°, 45.0°, 22.5°, and 67.5°. Dividing the intensities to form ratios R_q and R_u minimizes potential differences in the Wollaston prism's relative throughput on the two rays, relative differences in the response of the array locations where the two rays are detected and variations of sky transmission during the time between when the images are taken through the paired orientations of the HWP. The normalized Stokes parameters q and u computed with this ratio method are algebraically equivalent to the standard definitions:

$$q = \frac{Q}{I} \equiv \frac{I_0 - I_{90}}{I_0 + I_{90}} \quad ; \quad u = \frac{U}{I} \equiv \frac{I_{45} - I_{135}}{I_{45} + I_{135}} \tag{3.3}$$

where I_ϕ are the intensities transmitted through a linear polarizer (analyzer) with its transmission axis at angles $\phi = 0°$, 90°, 45° and 135°, and I is the total intensity. The fractional polarization p and position angle (PA) θ are then computed with:

$$p = \sqrt{q^2 + u^2} \quad ; \quad \theta = \frac{1}{2} \tan^{-1}\left(\frac{u}{q}\right) \tag{3.4}$$

The polarized intensity is the product of the fractional polarization and total intensity: $I_P = p \cdot I$. An S/N cut of 4-σ or 8-σ with respect to background fluctuations in polarized intensity off the source was selected as the cut-off for the display of polarization vectors. A 4-sigma cut is equivalent to de-biasing by a factor of less than 0.03 (see Equation (A3) of Wardle & Kronberg (1974)), which has no impact on our science.

The position angle θ computed using Equation (4) is in array coordinates. To convert to degrees East-of-North on the sky requires the addition of a calibration offset angle $\Delta\theta$, which is normally determined from observations of one or more polarized standard stars. Observations of the polarized standard star HD 29333 during the commissioning run did not provide a meaningful calibration offset due to non-photometric conditions at the

time the standard was observed and inadequate integration time. For our observations of IRC +10420 the uncorrected polarization vectors' orientation is physically implausible. Dust distributed around and illuminated by a single central source is expected to show a centro-symmetric scattering pattern, and previous observations of IRC +10420 by Kastner & Weintraub (1995) find such a pattern. An offset of $\Delta\theta_{K'} = 58°$ when added to each of our uncorrected polarization vectors achieves a centro-symmetric pattern in all directions around the star. We have therefore adopted this offset value.

In Figure 3.1(a) we display our resulting p^{raw}, the raw polarization around IRC +10420 prior to separation into stellar and nebular components. By "raw" we mean uncorrected for any underlying flux from the star in the wings of the PSF. With the adopted PA offset, the raw polarization is consistent with the centro-symmetric pattern characteristic of scattering of light from the central star by circumstellar dust. The raw percentage of polarization increases with radius, rising to a maximum of 15% at $1.7''$. This suggests the central star profile dilutes a higher intrinsic polarization of the nebula; this effect is corrected for in §3.3.1 below. In Figure 3.1(b) we display a flux-calibrated image of the raw intensity I^{raw} with the color scale in mag arcsec^{-2} for comparison with the contours in 1(a). In Fig. 3.1(c) we display the product of these two images, which is the polarized intensity $I_P^{raw} = p^{raw} \cdot I^{raw}$. While the raw intensity is dominated by the star and thus drops off smoothly with radius, the raw polarized intensity image shows a region of relatively flat, extended emission from $0.5''$ out to a radius of $\sim 2.5''$. This corresponds to emission from extended nebular material, not the stellar PSF.

3.2.2 IRC +10420: 3 - 5 μm AO Imaging

IRC +10420 was observed on 2011 May 25 UT during the commissioning of LMIRCam, the $2 - 5$ μm high-resolution camera on the Large Binocular Telescope (LBT) (Skrutskie et al., 2010). During commissioning a single 8.4 m primary mirror was used, in conjunction with the deformable AO secondary. This system achieves near-diffraction limited imaging and high sensitivity in the thermal infrared due to minimizing the number of reflecting surfaces and keeping all mirrors after the tertiary mirror at cryogenic temperatures. IRC +10420 was observed through two narrow-band filters: PAH1 ($\lambda_0 =$ 3.29 μm, $\Delta\lambda = 0.02$ μm), PAH2 ($\lambda_0 = 3.40$ μm, $\Delta\lambda = 0.02$ μm) as well as two broad-band filters: L$'$ ($\lambda_0 = 3.8$ μm, $\Delta\lambda = 0.3$ μm) and M ($\lambda_0 = 4.9$ μm, $\Delta\lambda = 0.3$ μm).

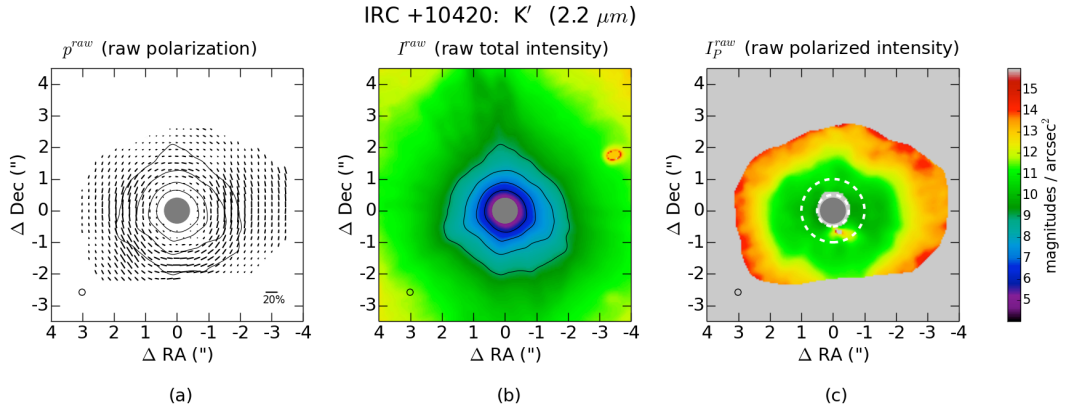

Figure 3.1 – MMT-Pol observations of IRC +10420 at λ = K′ (2.2 μm). North is up and East is left. The center is masked out to a radius of 0.4″ where the images saturated. The circle in the lower left is the beam size (0.2″ = FWHM of PSF). **(a):** The vectors are the raw polarization p^{raw} for a cut in polarized intensity of 4-σ with respect to background fluctuations off the source. The overlaid contours show the raw total intensity (total = unpolarized + polarized) from 9 to 6 mag arcsec^{-2}, progressing inwards in steps of -1 mag arcsec^{-2}. A portion of the image was masked in the south where faint artifacts which appear to have been caused by internal reflections of the heavily overexposed central point source within the instrument optics cause spurious polarization. The vectors show a centro-symmetric pattern characteristic of scattering by circumstellar dust. The raw polarization rises to about 15% at a radius of $\sim$ 1.7″ around most of the star. A length scale for the polarization vectors is given in the lower right of the image. **(b):** Raw total intensity I^{raw} in mag arcsec^{-2}, with the same overlaid contours as left image. **(c):** Raw polarized intensity $I_P^{raw} = p^{raw} \cdot I^{raw}$ in mag arcsec^{-2}. The dashed-line annulus indicates the region of overlap-of-coverage (OCR) with the $3-5$ μm LMIRCam observations (Fig. 3.2). A colorbar for the surface brightnesses is on the far right.

LMIRCam has a field of view approximately $10'' \times 10''$, with a pixel scale of $0.011''$ pixel^{-1}. The images of IRC +10420 were dithered for background sky subtraction. For the two PAH filters, the star η Aquilae provides a PSF (η Aql is point-like in the 3 - 8 μm range (Barmby et al., 2011)), while for the L$'$ filter the star BD +35 2435 is the PSF.

In Figure 3.2 we display the four LMIRCam images of IRC +10420 along with the PSF stars for comparison. In the bottom row of the figure, we have subtracted a scaled Moffat profile fitted to the PSF at each wavelength. For the M filter we radially scaled the L$'$ PSF profile by the ratio of λ_M to $\lambda_{L'}$. In all four filters IRC +10420 is substantially extended compared to the PSF.

We used two methods to determine a mean flux calibration factor in each filter. For the first method we equated the integrated intensity in ADUs per second out to the 3-σ level in each image (i.e., entire source = star + extended emission) with the specific flux F_ν from the ISO SWS spectrum for IRC +10420. For the second method, we calibrated the ADUs per second against those of the observed standard stars. For the flux of the standard star η Aql at the PAH1 & PAH2 filter wavelengths we interpolated between its reported magnitudes in the 2MASS Ks filter and IRAC Band 1 (Marengo et al., 2010). For the flux of the standard star BD +35 2435 at L$'$ we interpolated between its WISE W1 and W2 magnitudes. In the absence of a standard star observation in the M filter, we repeated the first method with comparison to IRC +10420's magnitude at M from the large, single aperture photometry of Jones et al. (1993). For each filter we use the mean calibration factors from the two methods, with estimated uncertainties of 15%, 10%, 10% and 5% in the PAH1, PAH2, L$'$ and M filters respectively.

3.2.3 VY CMa: J$'$ (1.3 μm) and 3.1 μm Imaging Polarimetry

We observed VY CMa with MMT-Pol on 2013 Oct 22 UT through a narrow-band J$'$ (λ_0 = 1.3 μm, $\Delta\lambda = 0.1$ μm). Six sets of dithered images were taken with a 1 s exposure time per HWP position. Data reduction was performed as discussed above for the MMT-Pol images of IRC +10420. The unpolarized standard star HD 224467 provided the PSF and flux-calibration. The offset $\Delta\theta_{J'}$ added to all polarization vectors was chosen to yield a centro-symmetric scattering pattern consistent with the *HST* visual polarimetry in Jones et al. (2007). We estimate our photometric uncertainty in the flux-calibration

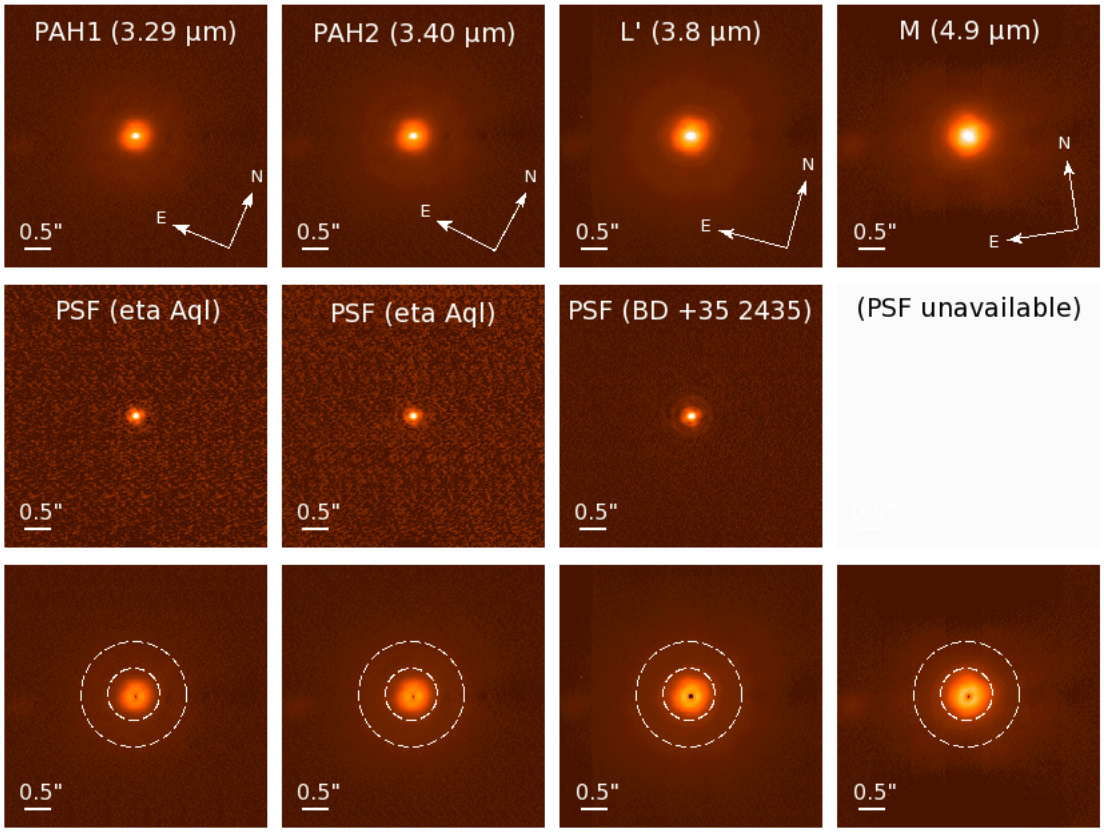

Figure 3.2 – IRC +10420: 3 - 5 μm adaptive optics images made with LBT / LMIRCam. **Top Row:** IRC +10420, with the filter for each column of images as indicated. Each FOV is $5'' \times 5''$, with square-root scaling to emphasize the extended nebular emission. **Middle Row:** PSF stars. For filters PAH1 and PAH2 the PSF is the star η Aql (FWHM = $0.10''$ in each filter), while at L$'$ the PSF is BD +35 2435 (FWHM = $0.11''$). There is no PSF image for the M filter from that night. **Bottom Row:** Same as the top-row images, after subtracting a scaled Moffat fit to each filter's PSF. To simulate a PSF for the M filter, the FWHM of the Moffat function used at L$'$ was scaled by the ratio $\lambda_M/\lambda_{L'}$. The top and middle row images are each stretched to the maximum pixel value at the center. The subtracted images of IRC +10420 in the bottom row are stretched to the same maximum value as the top row images. The dashed-line annulus on the subtracted images is the region of overlap-of-coverage (OCR) with the 2.2 μm polarimetry. It spans from $0.5''$ (where the 2.2 μm polarimetry is outside the saturated stellar image) out to $1.0''$, the 3-σ level in the PAH1 (3.29 μm) and M images.

from the two standards at 7%. We display our J′ polarimetry in Figure 3.3, and a comparison to the *HST* visual polarimetry in Figure 3.4.

We subsequently observed VY CMa through MMT-Pol's narrow-band 3.1 μm filter ($\Delta\lambda = 0.1$ μm) on 2014 Jan 16 UT. The PSF and flux-calibration were obtained from observations of HD 104624 and HD 29333. We estimate our photometric uncertainty in the flux-calibration from these two standards at 5%. For the 3 - 5 μm range, MMT-Pol uses a retarder which provides a retardance of 180° (half-wave) at 3.6 μm. For 3.1 μm light, the waveplate's retardance is 209°. Defining efficiency as the ratio of the input polarized intensity to the measured polarized intensity, the difference in retardance lowers the efficiency of the polarization measurement at 3.1 μm by a factor of 0.94. We have corrected the raw polarized intensity by this 6% factor during the reduction of the 3.1 μm images. The data reduction is otherwise the same as for IRC +10420, except we applied a S/N cut-off of 8-σ in polarized intensity to mitigate faint artifacts from the heavily over-exposed central star. A polarization vector offset has been added which achieves a centro-symmetric pattern. We display our result in Figure 3.5.

3.3 Analysis & Discussion

3.3.1 IRC +10420: Nebula's Intrinsic Polarization at K′

In their large-aperture polarimetry of IRC +10420 Jones et al. (1993) observed a fractional polarization of 1% at K′ for the combined star plus any unresolved nebula. The sub-arcsecond resolution now possible with MMT-Pol allows us to resolve nebular emission for radii greater than about 0.4″ (2000 AU), limited mostly by the exceedingly bright central star, which necessarily saturates in the integration times required to bring up the nebulosity. In our image the raw fractional polarization p^{raw} varies with radius, rising with increasing distance from the star up to a peak of about 15% at 1.7″ and then dropping off. This behavior indicates that flux in the PSF from the weakly polarized central star is diluting a higher intrinsic polarization of the nebula nearer the star.

To assess the nebula's intrinsic polarization, we first estimate the nebula's total (unpolarized + polarized) intensity I^{neb} by subtracting a representative star profile from the raw intensity I^{raw}. On the left-hand side of Figure 3.6 we plot the azimuthal

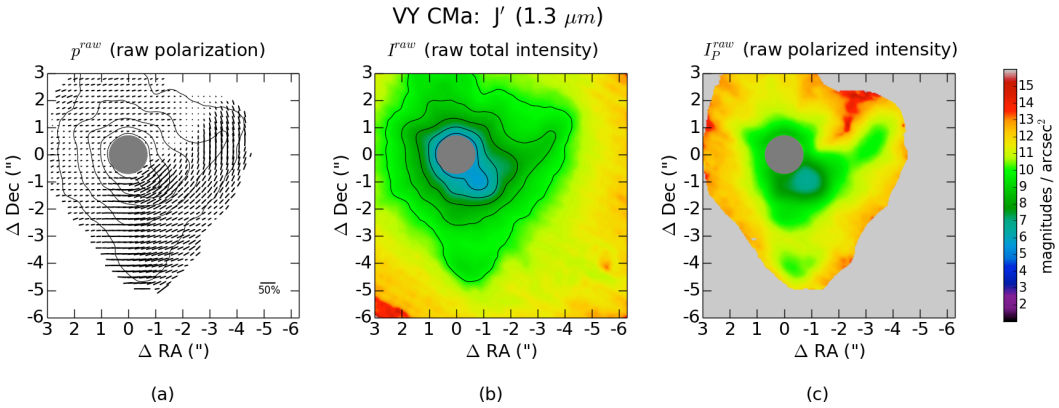

Figure 3.3 – MMT-Pol observations of VY CMa at $\lambda = \mathrm{J}'$ (1.3 μm). North is up and East is left. The center is masked out to a radius of 0.6″ where the star saturates. **(a):** The vectors are the raw polarization p^{raw} for a cut in polarized intensity of 4-σ with respect to background fluctuations off the source. The overlaid contours show the raw total intensity (total = unpolarized + polarized). The outermost contour is 10 mag arcsec^{-2}, with contours progressing inwards in steps of -1 mag arcsec^{-2}. The extended shape of the outermost contour towards the North is due to a faint artifact which appears to have been caused by internal reflections of the heavily overexposed central point source within the instrument optics. In contrast the extension to the South is real, coinciding with the location of the distinct component of the ejecta previously identified as Arc 2 by Humphreys et al. (2007) (see Fig. 3.4(a) below). The polarization vectors show a centro-symmetric pattern characteristic of scattering by circumstellar dust. **(b):** Raw total intensity I^{raw} in magnitudes arcsec^{-2}, with the same overlaid contours as left image. **(c):** Raw polarized intensity $I_P^{raw} = p^{raw} \cdot I^{raw}$ in mag arcsec^{-2}. A colorbar for the surface brightnesses is on the far right.

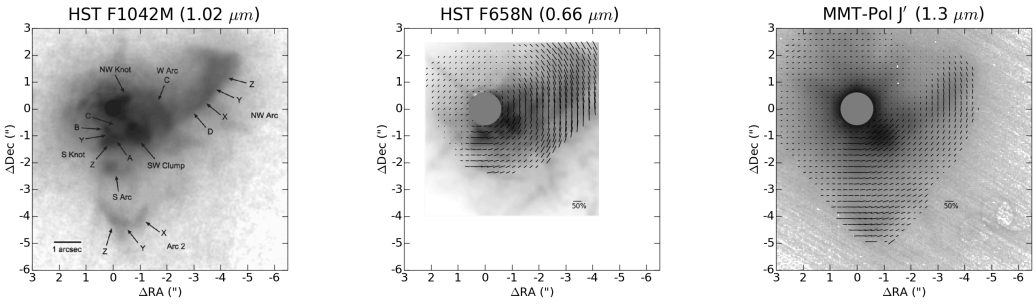

(a) (b) (c)

Figure 3.4 – VY CMa: **(a)** *HST* F1042M (1 μm) image reproduced from Humphreys et al. (2007) identifying the NW Arc, Arc 2, S Knot, S Arc and SW Clump. **(b)** *HST* visual (0.66 μm) polarimetry replotted using data from Jones et al. (2007). **(c)** MMT-Pol J′ (1.3 μm) polarimetry (this work).

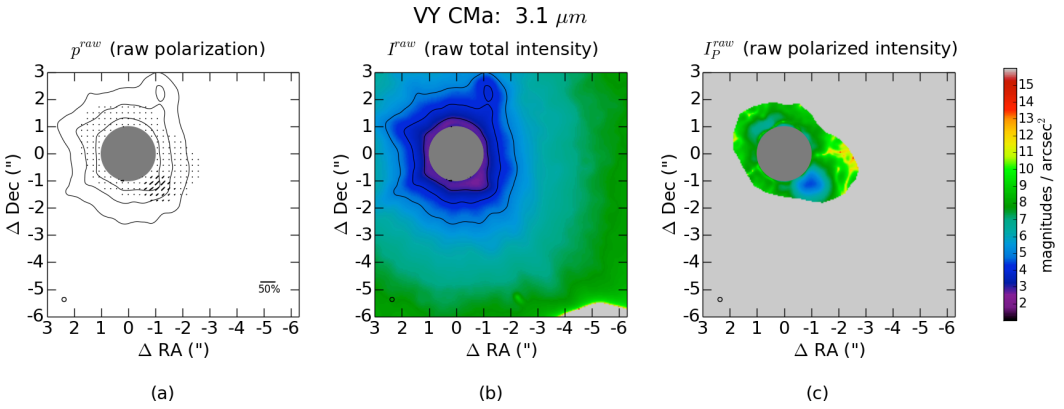

Figure 3.5 – MMT-Pol observations of VY CMa at $\lambda = 3.1$ μm. North is up and East is left. The center is masked out to a radius of 1.0″ where the star saturates. **(a):** The vectors are the raw polarization p^{raw} for a cut in polarized intensity of 8-σ with respect to background fluctuations off the source. The overlaid contours show the raw total intensity (total = unpolarized + polarized). The outermost contour is 5 mag arcsec^{-2}, with contours progressing inwards in steps of -1 mag arcsec^{-2}. **(b):** Raw total intensity I^{raw} in magnitudes arcsec^{-2}, with the same overlaid contours as left image. **(c):** Raw polarized intensity $I_P^{raw} = p^{raw} \cdot I^{raw}$ in mag arcsec^{-2}. A colorbar for the surface brightnesses is on the far right. The raw polarization at the location of the SW Clump is 20%.

average profile of I^{raw} for the regions to the East and West of the star, excluding the regions to the North and South where faint artifacts from the star are present. The star's light profile $I^{\star}$ is made using a Moffat function fitted to the PSF so that $I^{\star}$ can be extended out into the nebula. The fitted star profile has been scaled vertically so that it does not over-subtract by a radius of about $0.5''$. This scaling consistent with the difference in observed K magnitudes of the PSF star and IRC +10420, assuming K = 3.5 for the latter (Oudmaijer et al., 2009). The difference of the observed and star profiles is deemed to be the nebula's total intensity: $I^{neb} \equiv I^{raw} - I^{\star}$, which is depicted in Figure 3.6 with open circles.

For the nebula's polarized intensity I_P^{neb} we assume that all of the raw polarized emission in Figure 3.1(c) is entirely from the nebula: $I_P^{\star} \ll I_P^{neb}$ so that $I_P^{raw} \longrightarrow I_P^{neb}$. This only slightly overestimates I_P^{neb} within a radius of about $1''$ and becomes increasingly accurate as radius increases. For example with a 1% polarized star whose profile follows the PSF profile, by a radius of $1''$ the star's polarized intensity $I_P^{\star}$ is $\sim$ 10% of I_P^{raw} and falls off rapidly as the star's light profile descends going farther into the nebula region. The radial profile of I_P^{neb} is plotted with open squares in the upper right of Figure 3.6 along with the nebula's total intensity I^{neb}. The ratio of these intensities is used to compute the nebula's intrinsic fractional polarization, which by definition is $p^{neb} \equiv I_P^{neb} \ / \ I^{neb}$. This intrinsic polarization p^{neb} is plotted with solid black squares in the lower right of Figure 3.6. This removal of the star's light profile indicates that the nebula's intrinsic polarization is about 30% over a broad radial range from $0.5''$ to $\sim 2''$.

Based on radial velocity and proper motion measurements, Tiffany et al. (2010) found that the ejecta seen in *HST* visual images is moving mostly in the plane of the sky, and concluded that IRC+10420 is nearly pole-on and we are looking down onto an equatorial dust distribution. The relatively high fractional polarization (30%) at K$'$ that we find for the nebulosity surrounding the star is consistent with this model. For pure Rayleigh singly scattered light (size parameter $2\pi a/\lambda \ll 1$), polarization as high as 100% could in principle be expected for optically thin dust located exactly in the plane of the sky with respect to the star (scattering angle $\Theta = 90°$). Realistically the maximum possible polarization is likely lower for one or more reasons. For a distribution of grain sizes that includes larger grains with $2\pi a/\lambda$ on the order of 1, Mie theory applied to

spherical grains indicates the maximum polarization decreases below 100%. Consider for example a Gaussian distribution of grain sizes with mean radius $\bar{a} = 0.3$ μm and standard deviation $\sigma_a = 0.15$ μm, with astronomical silicate optical constants at 2.2 μm of $n = 1.72$, $k = 0.035$ (Draine & Lee, 1984). Computing the maximum polarization for such a distribution with the BHMIE subroutine (Bohren & Huffman, 1983) yields a maximum polarization of $\sim 60°$, occurring at a scattering angle slightly behind the plane of the sky. Alternately, for a distribution of scattering angles about 90° (a flared disk, for example) and multiple scatters, one would expect a lower fractional polarization than the ideal maximum. Since the nebulosity as seen in polarized intensity is distributed in a nearly circular pattern around the star and has a near constant fractional polarization, it can not be in a disk or torus that is tilted to the line of sight. For such a disk or torus the projected shape would be elliptical and the scattering angles would vary with azimuthal angle. The only other possible geometry that could explain the observed morphology and polarization of the nebulosity surrounding IRC+10420 is a thin cone opening towards (or away) from us at a uniform scattering angle and surface brightness with distance from the star. We find this to be implausible in light of the radial velocity measurements, although not ruled out by our polarimetry.

3.3.2 VY CMa: Intrinsic Polarization of Nebular Features at J′ (1.3 μm) and 3.1 μm

The polarized intensity images of VY CMa in Figures 3.3(c) & 3.5(c) reveal several distinct features of its complex nebula. Using the names designated by Humphreys et al. (2007) in their *HST* F1042M (1 μm) image (reproduced in Figure 3.4a), at J′ we observe the Northwest Arc, Arc 2, the Southwest Clump, the South Knot, and the South Arc. The first two features are located sufficiently distant from the star that their raw polarization is taken to be their intrinsic polarization. The raw polarimetry at J′ (1.3 μm) shows the NW Arc is ∼35% polarized, while Arc 2's polarization rises as high as 45%. These and subsequently discussed values are summarized in Table 3.2.

For the SW Clump, S Knot and S Arc, the intrinsic polarization of each is diluted by the star to varying extents. Applying the same procedure as in §3.3.1, we assume the raw polarized intensity is solely from the nebular feature so that $I^{raw}_{\lambda,P} \longrightarrow I^{neb}_{\lambda,P}$. We estimate the feature's total intensity I^{neb}_{λ} by subtracting from the raw intensity the

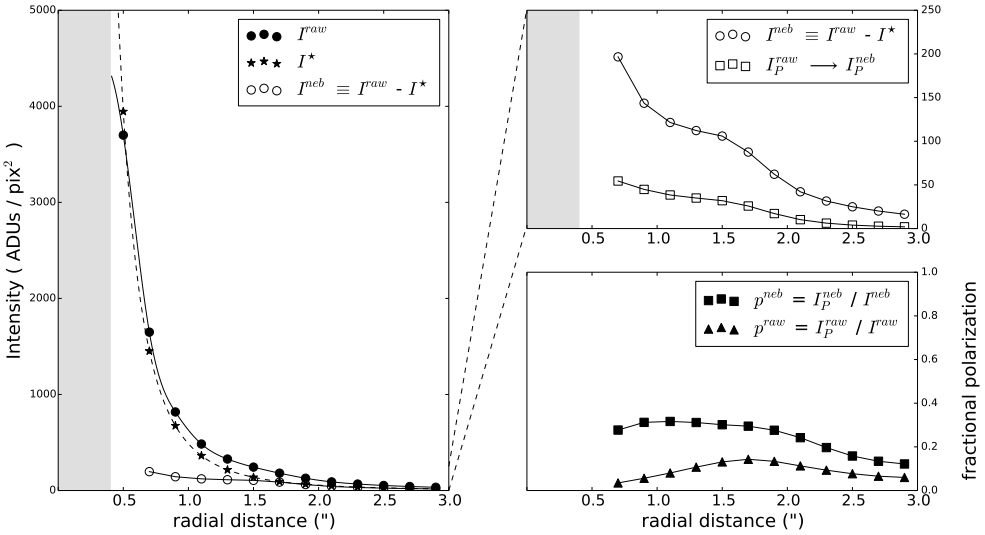

Figure 3.6 – Estimating the intrinsic polarization of IRC +10420's nebula at K′ (2.2 μm). **Left:** The filled circles are the azimuthal average of the raw intensity I^{raw} to the East and West of IRC +10420, using radial bins equal to the beam size (0.2″). The dashed line is a Moffat profile fitted to the PSF, scaled to represent the star's profile $I^{\star}$. The difference (open circles) is deemed to be the nebula's average profile I^{neb}. **Upper Right:** A zoomed view of the nebula's average profile I^{neb} (open circles). The open squares are the average profile of the raw polarized intensity I_P^{raw} (see Figure 3.1(c)), which is then assumed to be solely nebular emission: $I_P^{raw} \longrightarrow I_P^{neb}$. **Lower Right:** The nebula-only polarized intensity is then divided by the calculated nebula's total intensity to yield the nebula's intrinsic polarization $p^{neb} = I_P^{neb} \; / \; I^{neb}$ (filled squares), compared to the raw polarization p^{raw} (triangles). This removal of the star's light profile shows that on average the nebula's intrinsic polarization is at least a factor of 2 higher than the raw polarization and relatively constant from $0.5'' - 2''$.

profile of the star's light, which we represent using a photometric cut at position angle +148° East of North. Each nebular feature's intrinsic polarization is the ratio: $p_\lambda^{neb} \equiv I_{\lambda,P}^{neb} \; / \; I_\lambda^{neb}$. For the SW Clump as shown in Figure 3.7(a) for example, this raises its J′ raw fractional polarization slightly to an intrinsic polarization of 40%. For the S Knot and S Arc the same procedure raises the raw polarization of each from 40% to an intrinsic polarization of as much as 60%.

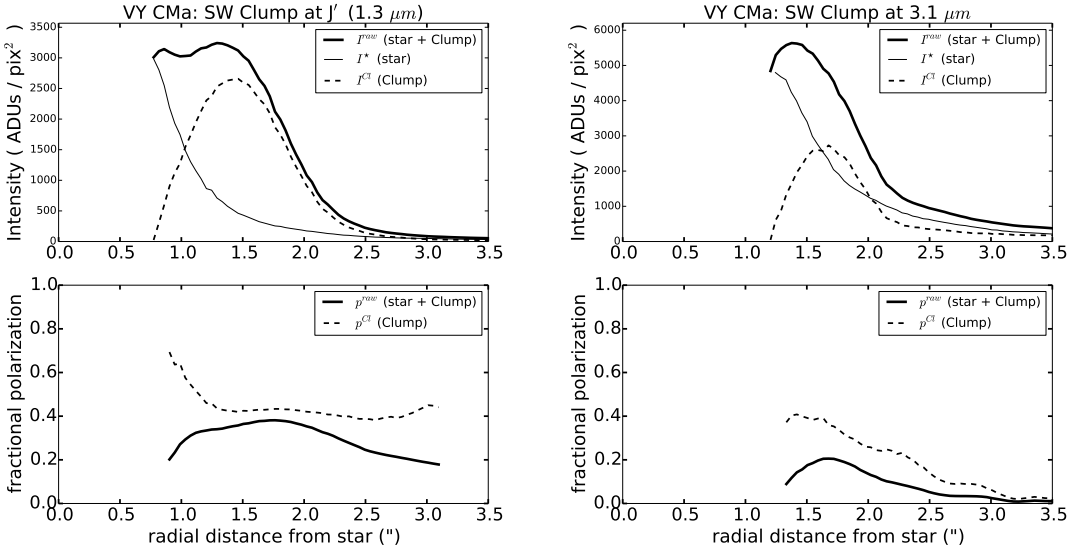

(a) (b)

Figure 3.7 – VY CMa intrinsic polarization: Photometric cuts through the SW Clump at J′ (1.3 μm) (left column) and 3.1 μm (right column). The SW Clump's proximity to the star results in the star's light profile diluting the Clump's intrinsic polarization. **Top row of (a) & (b)**: For each indicated filter the thick solid line is the raw (total) intensity along a cut through the Clump at a position angle of −135° E of N. The thin solid line is a cut at a position angle of +148° E of N, which is taken to represent the star's light profile into the region of the Clump. The dashed line is the difference of the two. **Bottom row of (a) & (b)**: For each filter the thick solid line is the raw fractional polarization p^{raw} along the same cut through the location of the Clump. The Clump's intrinsic fractional polarization p^{Cl} is estimated from scaling up p^{raw} by the ratio of $I^{raw} \; / \; I^{Cl}$ from the plot above.

At 3.1 μm the SW Clump is the sole feature observed in polarized intensity (Figure 3.5(c)). Per Figure 3.7(b) subtracting the star profile in that filter indicates the SW

Clump's intrinsic polarization is a factor of about 2 higher than the raw polarization, increasing from 20% to $\sim$ 40%. The SW Clump is a particularly curious feature in the ejecta of VY CMa. Humphreys et al. (2007) found it to be moving slowly away from the star with its motion largely in the plane of the sky. Previously reported AO imaging with LMIRCam has demonstrated that the Clump's $2 - 5$ μm emission must be due largely to diffusely reflected (i.e., optically thick) scattered light (Shenoy et al., 2013).

A silicate grain model fitted to the Clump's $2 - 5$ μm flux by Shenoy et al. (2013) indicated a dust mass lower limit of 5×10^{-5} $M_\odot$, with a temperature constrained to be between $80 - 210$ K. Interestingly, subsequent ALMA millimeter-range (mm) observations of VY CMa reported by O'Gorman et al. (2015) did not detect the Clump at 321 & 658 GHz. For the lower-limit dust mass computed from the $2 - 5$ μm scattered light, those authors find it would require the SW Clump to have an unusually low temperature (<20 K) to be undetected by ALMA. Alternately, given the 3-σ sensitivity limit of their observations, for a temperature between 80 - 210 K they find a dust-mass upper limit of $3 - 7 \times 10^{-6}$ $M_\odot$ within a single $0.229'' \times 0.129''$ elliptical beam. In the infrared the Clump spans an area roughly $\sim 1'' \times \sim 0.5''$. For the area spanned by the beam size of the mm observations, the mass lower limit from scattered light would decrease by a factor of about 3. Although that brings the infrared and mm mass estimates to within about a factor of 2, some discrepancy between these mass estimates remains. One possible explanation is the assumed wavelength dependence of the dust emissivity. Typically the emissivity is parameterized with a power-law form where the emissivity $\varepsilon_\lambda = (\lambda/\lambda_0)^{-\beta}$. For the diffuse ISM, β takes on the value of 1.6 (Planck Collaboration et al., 2014). O'Gorman et al. (2015) use a lower value of $\beta = 0.7$ based on their own spectral index fits and previous work on mm emission from VY CMa and similar late type stars (e.g. Knapp et al. (1993)). Kamiński et al. (2013) find $\beta \sim -0.5$ for VY CMa's $279 - 355$ GHz continuum emission. They do not see the SW Clump in their continuum map, however they do detect it in their line maps of H_2S (300.5 GHz) and CS (293.9 GHz). The absence of mm thermal dust continuum emission from the SW Clump could be due to a value of β that is much closer to the ISM value. The MMT-Pol observations reported here independently reconfirm the previous finding that the Clump is optically thick in the $1 - 3$ μm range (see next subsection), reaffirming the 5×10^{-5} $M_\odot$ *minimum* mass for the SW Clump and underscoring the need for

further investigation of this peculiar hypergiant.

3.3.3 Fractional Polarization versus Scattering Optical Depth

Our polarimetry of IRC +10420 and VY CMa show their nebulae exhibit fairly high intrinsic fractional polarizations in the infrared, with values for the various features ranging from 30% to 60% (see Table 3.2 summary). High fractional polarization is most easily reconciled with scattering by optically thin dust close to the plane of the sky. Here we assess whether the polarimetry is consistent with optically thin scattering. We conservatively define the cut-off for the transition to optical thickness at $\tau_\lambda^{sc} \geq 0.1$. For reflected light from optically thin dust, the scattering optical depth τ_λ^{sc} of each feature may be computed with:

$$\tau_\lambda^{sc} = \frac{4\pi \cdot I_\lambda^{neb} \cdot \phi^2}{F_\lambda^\star \cdot \sin^2(\Theta) \cdot \Phi(\Theta)} \tag{3.5}$$

(Sellgren et al., 1992). In this expression ϕ is angular radius on the sky, $F_\lambda^\star$ is the flux of the star at λ, Θ is the scattering angle and $\Phi(\Theta)$ is a phase function between 0 and 1 that accounts for the variation with scattering angle Θ of the intensity of scattered light from a sphere with assumed optical properties. Since moderately high intrinsic fractional polarizations indicate scattering close to the plane of the sky, we adopt a scattering angle of $\Theta = 90^\circ$ (plane of the sky) for simplicity. Assuming astronomical silicate spheres of size $\bar{a} \lesssim 0.3$ μm, $\Phi(\Theta = 90^\circ) \approx 0.4$ (Shenoy et al., 2013).

For each feature, we use its raw polarized intensity for I_λ^{neb} because this is a reliable lower-limit on the total scattered light intensity of the feature. The resulting τ_λ^{sc} lower limits discussed here are summarized in Table 3.2. For IRC +10420's nebula at 2.2 μm, at the peak of the azimuthal average of the polarized intensity at radius $1.7''$ we find $\tau_\lambda^{sc} \sim 0.4$. For VY CMa, although the star is saturated in the J$'$ images we can estimate its flux $F_{J'}^\star$ accurately enough in order to estimate the scattering optical depth of each of the five features discussed in the previous subsection. We fit a Moffat profile to the unsaturated portion of the star's light profile at a position angle +148° E of N, which avoids faint artifacts. The flux $F_{J'}^\star$ obtained from this fit agrees to within $\sim 35\%$ with the star's flux estimated from comparison of the narrow aperture photometry ($0.4''$ diameter) of VY CMa by Smith et al. (2001) with the unpolarized standard star HD 224467. We find $\tau_{J'}^{sc}$ values of 0.7 for the NW Arc, 1.0 for Arc 2, 0.8 for the S Knot, and

0.5 for the S Arc. For the SW Clump, we find $\tau_{J'}^{sc} > 1$ and $\tau_{3.1}^{sc} = 0.3$. We emphasize that these are *lower limits*, since the polarized intensity of each feature is a lower limit on its total scattered light intensity.

In all cases the computed lower limit to the scattering optical depth is above a purely optically thin regime. For grains with very high albedo, it would be expected that multiple scatterings of the light would depolarize it and thus prevent the relatively high intrinsic fractional polarizations seen in both hypergiants' nebulae. It has been shown in the visual, however, that for reflection from optically thick slabs relatively distant from the illuminating star, the depolarizing effect of multiple scatterings on linear polarization is less than expected at first glance (White, 1979). The maximum linear polarization of scattered optical light from an optically thick slab is on average within a factor of 0.7 of the polarization for singly scattered light. White demonstrated that dust grains with albedos of $\omega \lesssim 0.4$ could produce fractional polarizations of 40% in visual light scattered off of an optically thick slab. For spherical dust grains of radius $a \approx 0.1$ μm composed of astronomical silicate (Draine & Lee, 1984), the albedo is about 38% at 2.2 μm. For spherical dust grains used in modeling dusty oxygen rich, late type stars (Suh, 1999), albedos are well below 40% at near IR wavelengths. Our polarization observations are thus consistent with optically thick nebulosity for typical dust.

Table 3.2 – Nebular Features' Intrinsic Polarization and Minimum Scattering Optical Depths

Feature	PA[†] (° E of N)	distance from ⋆ (″)	λ (μm)	p_λ^{raw}	intrinsic p_λ^{neb}	minimum[‡] τ_λ^{sc}
			IRC +10420			
Azimuthal Avg.	- -	1.7	2.2	15%	30%	0.4
			VY CMa			
NW Arc	−80	3.4	J′ (1.3)	35%	35%	0.7
Arc 2	−175	4.1	"	45%	45%	1.0
S Knot	+180	1.3	"	40%	60%	0.8
S Arc	+180	2.4	"	40%	60%	0.5
SW Clump	−135	1.6	"	35%	40%	1
"	−135	1.6	3.1	20%	40%	0.3

[†] Location of feature with respect to the star.

[‡] Scattering optical depths are lower-limits, computed using polarized intensity as a reliable lower-limit on total scattered light intensity (see §3.3.3).

3.3.4 IRC +10420: Comparison of K′ Polarimetry with 3 − 5 μm Images

Here we use the image of IRC +10420's nebula as revealed by the K′ (2.2 μm) polarimetry to help interpret the extended emission seen in the LMIRCam 3 − 5 μm images. We assess whether the nebula's emission at these longer wavelengths is primarily scattered or thermal light or a combination of both. The K′ polarimetry overlaps with the LMIRCam images starting at a radius $\geq 0.5''$. The 3-σ levels in the PAH1, PAH2, L′ and

M images lie at radii of 1.0″, 1.2″, 1.8″, and 1.0″ respectively. To obtain the broadest wavelength coverage we select an outer radius of 1.0″ for the overlap-of-coverage region (hereafter OCR) that we examine. The PSF FWHM is $\lesssim 0.15''$ in all four LMIRCam filters and therefore in the OCR the star's light profile is negligible. This is in contrast to the MMT-Pol observations at K′, where it was necessary to heavily saturate the star image in order to bring up the much fainter nebulosity. The OCR is depicted with annuli on the LMIRCam images in the bottom row of Figure 3.2 and on the K′ image in Figure 3.1(c).

The nebula's emission from K′ through M in the OCR may be a combination of thermal emission and scattered light. The thermal component is assumed to be unpolarized, while the scattered light can have both unpolarized and polarized components:

$$I_\lambda^{neb} = I_\lambda^{neb,therm} + I^{neb,scat} \tag{3.6}$$

$$I_\lambda^{neb} = I_\lambda^{neb,therm} + (I_{\lambda,U}^{neb,scat} + I_{\lambda,P}^{neb,scat}) \tag{3.7}$$

Subscript P refers to the polarized intensity, and U refers to the unpolarized intensity in the scattered light. We first consider the minimum and total scattered light flux at K′ from the OCR. As in §3.3.1, the raw polarized intensity at K′ (Fig. 3.1(c)) must be scattered light from the nebula: $I_{K',P}^{raw} \longrightarrow I_{K',P}^{neb,scat}$. This provides a lower limit on $I_{K'}^{neb,scat}$, since the nebula must be less than 100% polarized. Assuming that thermal emission at K′ is negligible in comparison to the scattered light intensity, then the total scattered light intensity at K′ is simply this lower limit divided by the nebula's intrinsic fractional polarization: $I_{K'}^{neb,scat} = I_{K',P}^{raw} \;/\; p_{K'}^{neb}$. Per §3.3.1, $p_{K'}^{neb} \sim 0.3$, and therefore $I_{K'}^{neb,scat} \sim 3 \times I_{K',P}^{neb,scat}$. The lower-limit and estimated total scattered intensities integrated over the OCR are plotted as fluxes $F_{K',P}^{raw}$ and $F_{K'}^{neb,scat}$ respectively on the star's spectral energy distribution in Figure 3.8.

We next consider an upper limit on the contribution of unpolarized thermal emission to the nebular flux at K′. Given the polarimetry of VY CMa described in §3.3.2 and at visual wavelengths in Jones et al. (2007) (reproduced in Fig. 3.4b), the maximum fractional polarization of the scattered light from IRC +10420's nebula at K′ we would expect in the OCR is about 60%:

$$p^{neb,scat} = \frac{I_P^{neb,scat}}{I_U^{neb,scat} + I_P^{neb,scat}} \leq 0.6 \tag{3.8}$$

$$= \frac{I_P^{neb,scat}}{I^{neb,scat}} \leq 0.6 \tag{3.9}$$

The nebula's intrinsic fractional polarization of 30% (§3.3.1) is determined by the nebula's total scattered plus thermal emission:

$$p^{neb} = \frac{I_P^{neb,scat}}{I^{neb,scat} + I^{neb,therm}} = 0.3 \tag{3.10}$$

Comparing the maximum and intrinsic polarizations, we can write:

$$I^{neb,therm} \leq I^{neb,scat} \tag{3.11}$$

Thus, the maximum contribution of unpolarized thermal emission to the observed flux from the OCR in the K' filter would be roughly equal to the scattered light contribution.

The intensity of scattered light at a given wavelength is directly proportional to the illuminating star flux, which we designate as $F_\lambda^\star$, and the grains' albedo ω_λ. We scale $I_{K'}^{neb,scat}$ from K′ to the four longer wavelengths λ = PAH1, PAH2, L′ and M using ratios for the illuminating flux and grain albedo at the two wavelengths. We are assuming the OCR is outside of the region producing the bulk of the emission that makes up the SED of IRC+10420. In this way we can take the observed SED as the illuminating flux $F_\lambda^\star$ and express the following relationship:

$$I_\lambda^{neb,scat} = I_K^{neb,scat} \left(\frac{F_\lambda^\star}{F_K^\star}\right) \left(\frac{\omega_\lambda}{\omega_K}\right) \tag{3.12}$$

Note that the effects of interstellar reddening on the star's SED and the nebula are the same, so the extrapolation from K′ to the longer wavelengths can be done directly with the reddened (observed) SED. The ratio of the observed fluxes is $F_\lambda^\star / F_{K'}^\star \sim 2$ for all four LMIRCam filters.

Assuming silicate grains of radius $a \ll \lambda$ (e.g., $a \lesssim 0.1$ μm) the ratio of the albedos $\omega_\lambda/\omega_{K'}$ for the four filters are 0.39, 0.36, 0.26, and 0.13. These albedo ratios are typical ratios for astronomical silicates for the interstellar medium (Draine & Lee, 1984) and oxygen rich mass-loss winds (Suh, 1999). With these values in Equation (12), we predict the $3 - 5$ μm scattered light fluxes depicted with open blue circles in Figure 3.8. On the SED in Figure 3.8, the nebula's integrated $3 - 5$ μm fluxes for the OCR from $0.5''$ to $1.0''$ are plotted as grey circles. The open red circles are the excess flux in each of these

3 filters (total − predicted scattered). As can be seen in Figure 3.8, the total nebular emission at $3 - 5$ μm is about a factor of 10 brighter than scattered light alone can account for. It is most likely the nebula's emission at ~ 3 μm and beyond is primarily thermal in origin. However, we have just shown that at most half of the flux at 2.2 μm can be thermal, and this puts strong constraints on any explanation for the surprisingly large $3 - 5$ μm fluxes.

On the SED in Figure 3.8 we plot the spectrum of a 500 K emissivity-modified blackbody which passes through the L′ excess flux. This choice of temperature was chosen to prevent too much thermal flux at 2.2 μm (a higher temperature) and too much flux in the mid-IR (a lower temperature) which would compete with or exceed the observed mid-IR flux from the entire system. A lower temperature such as 400 K, for example, would require fully half of the entire 10 μm silicate feature to arise from the OCR alone, which seems unlikely. The blackbody equilibrium temperature is 120 K, assuming $L^{\star}_{bol} = 5 \times 10^5\ L_{\odot}$ and $D = 5$ kpc. Factoring in wavelength-dependent emissivity Q^{abs}_{λ} to account for less efficient emission in the infrared, the dust equilibrium temperature is $T_{eq} = (\langle Q_{UV,vis} \rangle / \langle Q_{IR} \rangle)^{1/4}\, T_{bb}$, where $\langle Q_{UV,vis} \rangle$ and $\langle Q_{IR} \rangle$ are the Planck-averaged emissivities for the wavelength ranges where the grains absorb and emit, respectively. For the typical silicate grains we have been using (Draine & Lee, 1984; Suh, 1999) this factor raises the equilibrium temperature to ~ 210 K. Although warmer than blackbody equilibrium, this is still too cool to be compatible with the observed mid-IR flux.

The ~ 500 K color temperature we require is 2 to 3 times higher than the expected equilibrium temperature. One possibility is emission from transiently heated small dust grains, which can temporarily reach much higher equilibrium temperatures from absorption of a single stellar photon with an energy comparable to the grain's heat capacity. These grains are usually associated with reflection nebulae illuminated by a source of near-UV photons, e.g., Sellgren et al. (1983). However, the spectrum of emission from these very small grains corresponds to color temperatures much higher than the 500 K we require to explain the emission from the OCR. For example, Draine & Li (2007) compute SEDs for $a = 5$ Å silicate grains exposed to the interstellar radiation field (roughly equivalent to an F0 star, similar to the IRC+10420). They find such a tiny grain's spectrum to be relatively flat from $2.2 - 5$ μm (see their Figure 10), which is

incompatible with our observations. We do note that our 500 K color-temperature is close to with the **gas** temperature at this radius ($r \sim 0.75'' = 5.6 \times 10^{16}$ cm) modeled by Castro-Carrizo et al. (2007) in their study of CO emission around IRC +10420. These authors modeled the CO emission as arising from two spherical shells, with the inner shell spanning from 0.3″ to 1.7″ in radius, very similar to our OCR. At the 0.75″ mean radius of the OCR we examine, their best-fit model predicts a **gas** temperature of T_{eq} = 460 K. While our polarimetry observations clearly require a nebular material lying largely in the plane of the sky as opposed to a shell, the similarity in their gas temperature and the dust color temperature we derive indicates that higher than equilibrium temperatures are physically real.

3.4 Conclusions

1. We present images of the nebulosity surrounding the hypergiant VY CMa in polarized light with a resolution of 0.2″ at 1.3, and 3.1 μm. Many nebular features are seen in polarized intensity at 1.3 μm and one feature, the SW Clump, is very prominent at 3.1 μm as well.

2. Extended emission around VY CMa shows both high fractional polarization and high scattering optical depths. The surface brightness is consistent with scattered light alone. The high fractional polarization is consistent with grain albedos considerably less than 1. The required albedos are easily compatible with the typical silicate grains used to model dusty stars.

3. The polarimetry of VY CMa independently confirms that its Southwest (SW) Clump is optically thick from 1.3 − 3.1 μm. This affirms the minimum mass of the SW Clump computed by Shenoy et al. (2013) from its scattered light in the infrared. Absence of thermal dust emission at mm wavelengths from the SW Clump presents a puzzle.

4. We present images of the nebulosity surrounding IRC+10420 in polarized light at 2.2 μm with a resolution of 0.2″ and total flux at 3.3, 3.4, 3.8, and 4.9 μm with a resolution of 0.1″ − 0.15″.

5. The polarized intensity image of IRC+10420 at 2.2 μm shows a relatively uniform nebula largely in the plane of the sky extending from 0.5″ − 2.5″ radius (2500 − 12500

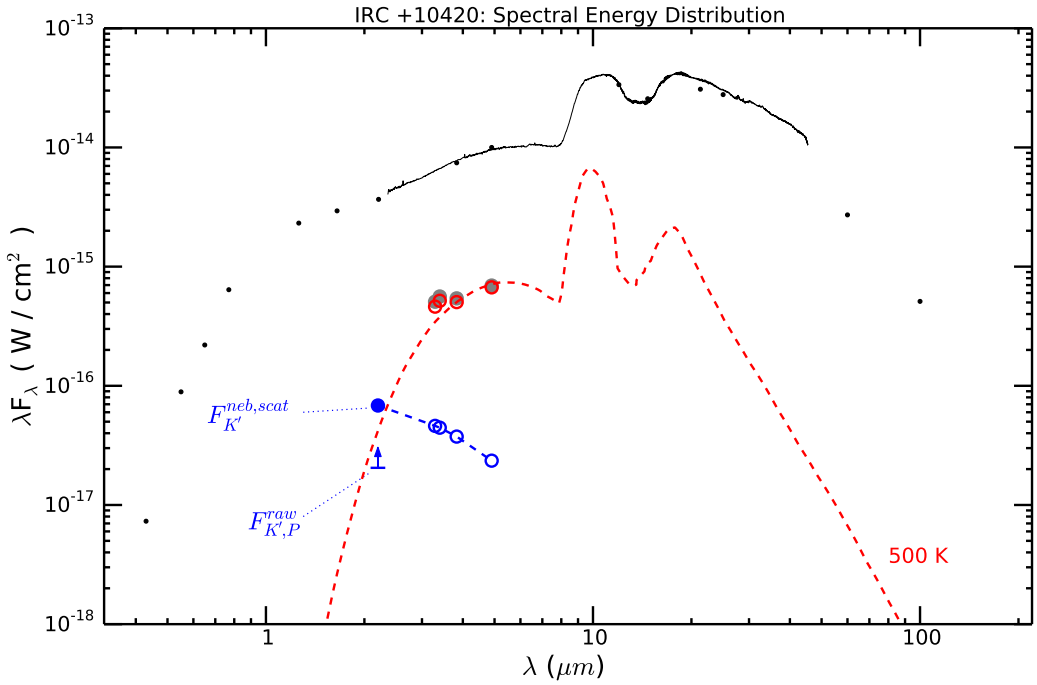

Figure 3.8 – Spectral energy distribution of IRC +10420. The black dots are point-source photometry compiled from Jones et al. (1993), Oudmaijer et al. (1996) and the IRAS and MSX Point Source Catalogs (with color correction). The thin black line is the ISO SWS spectrum. $F_{K',P}^{raw}$ is the polarized intensity at $\lambda = \mathrm{K}'$ (2.2 μm) integrated over the overlap-of-coverage region (OCR, the annulus depicted in Figure 3.1(c) and the bottom row of Figure 3.2). This is a lower limit on the scattered light flux at K$'$ from this region. The filled blue circle $F_{K'}^{neb,scat}$ is the estimated total (unpolarized + polarized) scattered light flux for $p_{K'}^{neb} \sim 0.3$ (§3.3.1). The blue dashed line scales this total scattered light flux to λ = PAH1 (3.29 μm), PAH2 (3.40 μm, L$'$ (3.83 μm) and M (4.9 μm) using Equation (12) in order to predict the nebula's scattered light flux at those wavelengths (open blue circles). The filled grey circles are the nebula's total 3 − 5 μm fluxes in those filters, with uncertainty smaller than the symbol size for all except the PAH1 filter. The open red circles are the excess flux (total − scattered). The red dashed line is an emissivity-modified $\lambda B_\lambda(T_{eq})$ curve for T_{eq} = 500 K.

AU for D = 5 kpc). The surface brightness of this low-latitude ejecta is compatible with optically thick scattering and, similar to VY CMa, grain albedos compatible with typical astronomical silicates.

6. In the $3 - 5$ μm band, images of IRC+10420 show a strong extended component that overlaps with the nebula seen in polarized intensity at 2.2 μm. The flux from this extended component is an order of magnitude brighter than can be explained by simple extrapolation of the scattered light seen at 2.2 μm. We hypothesize grains warmed to a temperature higher than the expected grain equilibrium temperature, but consistent with the local gas temperature in this region.

3.5 Acknowledgements

The authors thank the referee Dr. Geoffrey Clayton for his thoughtful comments which have helped us to improve this manuscript. We also thank Dr. Roberta M. Humphreys for many illuminating discussions and her insights on the nature and history of these fascinating targets. We gratefully acknowledge the steady support of the staffs of the MMT and LBT Observatories in making these observations possible. MMT-Pol is funded by the National Science Foundation under grant NSF AST-0705030. LMIRCam is funded by the National Science Foundation under grant NSF AST-07049992.

Chapter 4

Searching for Cool Dust in the Mid-to-Far Infrared: the Mass Loss Histories of The Hypergiants μ Cep, VY CMa, IRC+10420, and ρ Cas

This chapter has been accepted for publication in the Astronomical Journal with the following author list: Shenoy, D. P., Humphreys, R. M., Jones, T. J., Marengo, M., Gehrz, R. D., Helton, L. A., Hoffmann, W. F., Skemer, A. J., Hinz, P. M.

Abstract

We present mid- and far- IR imaging of four famous hypergiant stars: the red supergiants μ Cep and VY CMa, and the warm hypergiants IRC +10420 and ρ Cas. Our 11 to 37 μm SOFIA/FORCAST imaging probes cool dust not detected in visual and near-IR imaging studies. Adaptive optics (AO) 8 - 12 μm imaging of μ Cep and IRC +10420 with MMT/MIRAC reveals

extended envelopes that are the likely sources of these stars' strong silicate emission features. We find μ Cep's mass-loss rate to have declined by about a factor of 5 over a 13,000 history, ranging from 5×10^{-6} down to $\sim 1 \times 10^{-6}$ $M_{\odot}$ yr^{-1}. The morphology of VY CMa indicates a cooler dust component coincident with the highly asymmetric reflection nebulae seen in the visual and near-IR. The lack of cold dust at greater distances around VY CMa indicates its mass-loss history is limited to the last $\sim$1200 years, with an average rate of 6×10^{-4} $M_{\odot}$ yr^{-1}. We find two distinct periods in the mass-loss history of IRC +10420 with a high rate of 2×10^{-3} $M_{\odot}$ yr^{-1} until approximately 2000 yr ago, followed by an order of magnitude decrease in the recent past. We interpret this change as evidence of its evolution beyond the RSG stage. Our new infrared photometry of ρ Cas is consistent with emission from the expanding dust shell ejected in its 1946 eruption, with no evidence of newer dust formation from its more recent events.

4.1 Introduction

The fate of massive stars is strongly affected by their mass-loss rates and mass-loss histories. The majority of stars above 9 $M_{\odot}$ will pass through the RSG stage, during which they shed large amounts of mass. Depending on the duration and rate of mass-loss, the total mass shed during the RSG stage can represent a significant fraction of the initial mass of the star and influences its terminal state, whether as a supernova or in post-RSG evolution. However, the mechanism by which RSGs lose mass remains uncertain. For some RSGs and post-RSGs we find evidence of discrete, episodic mass-loss. For example, high resolution optical imaging and spectroscopy of the warm OH/IR post-red supergiant (RSG) IRC +10420 and the peculiar OH/IR M-type supergiant VY CMa have yielded surprising results about their complex circumstellar environments, with evidence for asymmetric ejections and multiple high mass-loss events (Smith et al., 2001; Humphreys et al., 2005, 2007; Jones et al., 2007; Tiffany et al., 2010; Shenoy et al., 2013).

Since a substantial portion of the emission from dusty ejected material is thermal, observations in the infrared are important for mapping the extent of mass loss and the

mass-loss history. In this paper we report on a search over a range of wavelengths for extended warm and cold dust around four famous hypergiant stars: the RSGs μ Cep and VY CMa and the warm hypergiants IRC +10420 and ρ Cas. Thermal emission from dust in their circumstellar environment may be evidence of recent high mass loss episodes or may be a fossil record of earlier mass loss. We extend the study of these stars' mass-loss into the mid-IR, reporting new SOFIA/FORCAST (Herter et al., 2012) 11 - 37 μm imaging, combined with publicly available *Herschel*[1] (Pilbratt et al., 2010) PACS (Poglitsch et al., 2010) images. We also include sub-arcsecond resolution 8 - 12 μm observations of μ Cep, IRC +10420, and ρ Cas made with MMT/MIRAC (Hoffmann et al., 1998; Hinz et al., 2000). The observations are described in §2 and are summarized in Tables 1 and 2. We discuss our results in §3 and summarize them in Table 3 and in the last section.

4.2 Observations and Data Reduction

4.2.1 SOFIA/FORCAST: Far-IR Imaging (11 − 37 μm)

We observed μ Cep, VY CMa, IRC +10420 and ρ Cas with SOFIA/FORCAST during Cycle 2 (OBS ID 02_0031, PI: R.M. Humphreys). FORCAST is a dual-channel mid-IR imager covering the 5 to 40 μm range. Each channel uses a 256 × 256 pixel blocked-impurity-band (BiB) array and provides a distortion-corrected $3\farcm2 \times 3\farcm2$ field of view with a scale of $0\farcs768$ pixel^{-1}. FORCAST achieves near-diffraction limited imaging, with a point-spread function (PSF) full-width-at-half-maximum (FWHM) of $\sim 3\farcs7$ in the longest filters. The images were obtained in single-beam mode to maximize throughput for detecting faint extended emission. The observations were made in standard two-position chop-and-nod mode with the direction of the nod matching the direction of the chop. The data were reduced by the staff of the SOFIA Science Center using the FORCAST Redux v1.0.1 pipeline. After correction for bad pixels and droop effects, the pipeline removed sky and telescope background emission by first subtracting chopped

[1] *Herschel* is an ESA space observatory with science instruments provided by European-led Principal Investigator consortia and with important participation from NASA. The *Herschel* data used in this paper are taken from the Level 2 (flux-calibrated) images provided by the Herschel Science Center via the NASA/IPAC Infrared Science Archive (IRSA), which is operated by the Jet Propulsion Laboratory, California Institute of Technology, under contract with NASA.

image pairs and then subtracting nodded image pairs. The resulting positive images are aligned and merged. The details of the FORCAST pipeline are discussed in the Guest Investigator Handbook for FORCAST Data Products, Rev. A2.[2]

Bright point sources cause cross-talk in the horizontal direction on the FORCAST array. To mitigate this effect, chop angles were selected so that the cross-talk pattern from one chop position did not overlap with the other chop position. Additionally, the FORCAST pipeline applies a correction that reduces the effect, although some of the pattern remains for some targets. The effect is most noticeable for the two brightest targets, VY CMa and IRC +10420; it is less for μ Cep and is not present in the images of ρ Cas. For VY CMa and IRC +10420 we avoid the array horizontal direction when examining the images for evidence of extended emission. For μ Cep where the effect is less apparent, we have marked on the images where the faint pattern is present. Calibrator star observations from each flight were obtained from the SOFIA Science Archive for comparison. We display the calibrators observed on the same flight as our science targets and in the same filter with the four-position slide in either the mirror position (for the short wavelength channel) or the open position (for the long wavelength channel). In some instances the merging of the two chop beams by the FORCAST data reduction pipeline imparted an extended shape to the calibrator star that is not present in at least one or sometimes both of the two individual pre-merge images of the calibrator star. When this effect was apparent we have displayed one of the pre-merge images for comparison. This blurring effect during this merging of the two chop beams does not appear to have occurred in our final merged science images, for which we compared each of the pre-merge images to the merged image as well. In particular, the extended shapes of both VY CMa and IRC +10420 discussed below are not an effect of the merging step since the extended shape is clearly seen in the individual chop beams.

The FORCAST pipeline coadds the merged images. To determine a 1-σ uncertainty in our quoted fluxes, for each of our targets we computed the standard deviation of the mean of fluxes extracted from the merged images prior to coadding. For the fluxes of the bright targets μ Cep, VY CMa and IRC +10420, the fractional variation in total ADUs in each filter is negligible compared to the 6% uncertainty in the flux calibration per the GI Handbook §4.1 (Herter et al., 2013). Therefore for those targets we adopt

[2] Available at http://www.sofia.usra.edu/Science/index.html under “SOFIA Data Products”

Table 4.1. List of SOFIA FORCAST Observations

Target	Date Obs (UT)	Filters[a]	Int Time (s)	PSF FWHM (arcsec)
μ Cep	2014 05 03	F111, F197, F253 F315, F348, F371	14, 12, 343 521, 1034, 1865	2.″6, 2.″6, 3.″6 3.″2, 3.″5, 3.″7
VY CMa	2014 03 22	F197, F253 F315, F348, F371	36, 284 320, 856, 392	2.″7, 2.″9 3.″2, 3.″5, 3.″7
IRC +10420	2014 06 06	F197, F253 F315, F348, F371	18, 215 283, 592, 989	3.″2, 3.″2 3.″5, 3.″7, 3.″8
ρ Cas	2014 03 27	F197, F253 F315, F348, F371	42, 237 319, 848, 1821	3.″0, 3.″3 3.″4, 3.″7, 4.″0

[a] The effective wavelengths of the SOFIA FORCAST filters are: F111 = 11.1 μm ($\Delta\lambda$ = 0.95 μm), F197 = 19.7 μm ($\Delta\lambda$ = 5.5 μm), F253 = 25.3 μm ($\Delta\lambda$ = 1.86 μm), F315 = 31.5 μm ($\Delta\lambda$ = 5.7 μm), F348 = 34.8 μm ($\Delta\lambda$ = 3.8 μm), F371 = 37.1 μm ($\Delta\lambda$ = 3.3 μm). Source: SOFIA Observer's Handbook v4.1.0 §7.1.3.

6% as the 1-σ uncertainty. For ρ Cas the fractional variations are between $1-6\%$ and are added in quadrature with the 6% uncertainty from the flux calibration to be the 1-σ uncertainty. The band-passes of the selected FORCAST filters are such that only small color corrections are required. Based on the mostly $\lambda F_\lambda \propto \lambda^{-3}$ spectral shapes of our targets in the relevant range, we have applied small color corrections[3] of 1.004, 1.071, 1.004, 1.044, 1.025, and 1.025 to fluxes extracted from the F111, F197, F253, F315, F348 and F371 images respectively. The FORCAST observations are summarized in Table 4.1.

[3] Obtained from http://www.sofia.usra.edu/Science/DataProducts/FORCAST_ColorCorrecns_OC1.pdf

4.2.2 MIRAC3/4: Adaptive Optics Mid-IR Imaging (8 − 12 μm)

Three of our SOFIA targets were also observed at high angular resolution in the 8 − 12 μm range using the MIRAC3/4 cameras on the 6.5-m MMT (Hoffmann et al., 1998; Hinz et al., 2000). μ Cep was observed on UT 2006 July 22 with MIRAC3, while ρ Cas, IRC +10420 and additional RSG targets were observed with MIRAC4 (Skemer et al., 2008) between 2006 November 05 and 2009 October 02. Both MIRAC configurations achieved very high Strehl-ratios (approx. 0.95), providing diffraction-limited imaging and stable PSFs (e.g., Biller et al., 2005). MIRAC3 and MIRAC4 employed Si:As arrays with 128 × 128 and 256 × 256 pixels respectively. Observations were made with a standard chop-and nod sequence to remove IR background emission. Cross-talk in the array electronics introduced faint artifacts in the horizontal and vertical directions that were not completely removed by chop-and-nod subtraction. For the MIRAC4 images the horizontal cross-talk is mitigated during the data reduction with a code written by M. Marengo (Skemer et al., 2008). Extension in directions other than array vertical and horizontal are not affected by cross-talk. The PSF-subtracted images of μ Cep presented here are reproduced from Schuster (2007), while the images of IRC +10420 are previously unpublished. The additional RSG targets[4] RW Cep, RW Cyg and BD +24 3902 resemble IRC +10420 with a similar extended appearance that is azimuthally symmetric, while ρ Cas and W Per are point-like with no noticeable extension compared to the PSF stars. S Per is extended at 8.9 and 9.8 micron with an elliptical envelope oriented in a NNE-SSW direction similar to extension seen in the *HST* visual images (Schuster et al., 2006). T Per is marginally extended at 11.9 μm. Flux calibration for the 9.8 and 11.7 μm images of μ Cep was done using observations of the PSF standard γ Dra taken immediately afterward, with an estimated uncertainty of 10% in the calibration. Flux calibration of the ρ Cas observations was done using the standard stars β And, α Aur and β Peg, with an estimated uncertainty of 10% as well. The MIRAC observations are summarized in Table 4.2.

[4] See Appendix A.

Table 4.2. List of MMT/MIRAC Observations

Target	Date Obs (UT)	Filter(s)[a] (μm)	Int Time (s)	PSF FWHM (arcsec)	Extension evident?
μ Cep	2006 07 23	8.8, 9.8, 11.7	272, 362, 483	0.″34, 0.″38, 0.″45	Yes (Fig 4.1)
ρ Cas	2006 11 05	8.9, 9.8	156, 331	0.″34, 0.″37	No
S Per	2006 11 05	8.9, 9.8	26, 260	0.″34, 0.″37	Yes
IRC +10420	2008 06 16	8.9, 9.8, 11.9	289, 313, 337	0.″34, 0.″37, 0.″47	Yes (Fig 4.9)
RW Cep	2009 09 30	8.7, 9.8, 11.9	1094, 1094, 1064	0.″38, 0.″43, 0.″52	Yes[b]
W Per	2009 09 30	8.7, 9.8, 11.9	1117, 764, 265	0.″38, 0.″43, 0.″52	No
RW Cyg	2009 10 01	8.7, 9.8, 11.9	1324, 1204, 1385	0.″39, 0.″42, 0.″53	Yes[b]
BD +24 3902	2009 10 02	8.7, 9.8, 11.9	1440, 1440, 1140	0.″39, 0.″42, 0.″53	Yes[b]
T Per	2009 10 02	8.7, 9.8, 11.9	202, 193, 101	0.″39, 0.″42, 0.″53	Yes[b]

Note. — The 2006 July observations of μ Cep were made with the MIRAC3 instrument. Observations starting 2006 November were made with the successor instrument MIRAC4. See §2.2 for details.

[a] The bandwidths of the MIRAC3 8.8, 9.8 and 11.7 μm filters are $\Delta\lambda = 0.88$, 0.98 and 1.12 μm respectively. The bandwidths of the MIRAC4 8.9, 9.8 and 11.9 filters are $\Delta\lambda = 1.22$, 0.91, and 1.14 μm respectively.

[b] The extended shape apparent after PSF subtraction is azimuthally symmetric, resembling that of IRC +10420 in Figure 4.9 (bottom row).

4.3 Results & Discussion

4.3.1 Method for Estimating Mass-Loss Rates

We compute mass-loss rates for the resolved targets μ Cep, VY CMa and IRC +10420 using the DUSTY radiative transfer code (Ivezic & Elitzur, 1997) to model the stars' spectral energy distributions (SEDs) and azimuthal average intensity profiles at one or more wavelengths. DUSTY solves the radiative transfer equation for a spherically symmetric dust distribution around a central source. The user specifies the spectrum of the illuminating source, the optical properties and size distribution of the dust grains, the dust temperature at radius r_1 (the inner boundary of the shell), a functional form for the radial profile of the dust density $\rho(r)$ throughout the shell from inner radius r_1 to outer radius r_2, and the total optical depth at a chosen wavelength for a line of sight through the shell directly to the central source. For a given set of these inputs, DUSTY outputs a model SED and a radial profile of the intensity of the shell at desired wavelengths.

Assuming spherical symmetry is a simplification that cannot capture the full 3-D spatial distribution of asymmetric circumstellar ejecta, which is known to be particularly complex in the optical and near-infrared in the cases of VY CMa (Smith et al., 2001; Humphreys et al., 2005, 2007; Shenoy et al., 2013) and IRC +10420 (Humphreys et al., 1997; Tiffany et al., 2010; Shenoy et al., 2015). The effect of asymmetry is less influential at lower optical depths, which is the case for μ Cep (see §3.2.2 below). The advantage gained by the use of a radiative transfer code such as DUSTY is a relatively consistent treatment across our targets, allowing for comparison of the results for similar assumptions about the dust responsible for their infrared SEDs and intensity profiles.

For a fitted model's optical depth τ_λ, the grain opacity κ_λ specifies the dust mass density $\rho(r)$ in g cm^{-3} throughout the shell. If the expansion velocity is constant throughout the shell, the mass-loss rate at a time t in the past is the rate at which gas and dust pass radius $r = v_{exp} \cdot t$. This may be written as $\dot{M}(t) = g_d \cdot 4\pi r^2 \cdot \rho(r) \cdot v_{exp}$ where g_d is the gas-to-dust mass ratio, which we assume to be 100:1.[5] For this constant expansion velocity case, a model with density distribution $\rho(r) \propto r^{-q}$ with power law

[5] The gas-to-dust mass ratios assumed or derived for these targets typically range from 100:1 (e.g., Knapp et al., 1993; Verhoelst et al., 2009) to 200:1 (e.g., Mauron & Josselin, 2011; Cox et al., 2012; Oudmaijer et al., 1996).

index $q < 2$ indicates a gradual decline in the mass-loss rate over the dynamical age of the shell.

If the expansion velocity has not been constant at all times throughout the shell, we compute an average mass-loss rate. We multiply the density distribution $\rho(r)$ by the same assumed 100:1 gas-to-dust mass ratio and integrate to compute M, the total mass of gas and dust in the shell. We assume an average expansion velocity to compute the dynamical age of the shell $\Delta t = r_2 \ / \ v_{exp}$ where r_2 is the outer radius of the shell for the model. The average mass loss rate is then $\langle \dot{M} \rangle = M \ / \ \Delta t$. The particular choices for grain type, size distribution, shell radii and dust density distribution are discussed in the sections specific to each target below, as well as the limitations on assuming a single average expansion velocity in the cases of VY CMa and IRC +10420. The $\langle \dot{M} \rangle$ values determined for μ Cep, VY CMa and IRC +10420 are summarized in Table 3.

4.3.2 μ Cep

Mid-IR Imaging

The combination of adaptive optics mid-IR imaging with MIRAC3 and wide-field far-IR imaging with SOFIA/FORCAST allow us to probe μ Cep's circumstellar environment over a broad time-scale. We first consider its close environment. *HST*/WFPC2 images found no evidence of scattered light within $0\farcs1 - 0\farcs2$ of the star (Schuster et al., 2006). De Wit et al. (2008) obtained ground-based diffraction-limited ($0\farcs6$) 24.5 μm images of μ Cep over multiple nights with COMICS on the 8.2 m Subaru telescope. They detected a roughly spherical circumstellar nebula out to a radius of at least $6''$ with an asymmetric bipolar-type geometry extending to a radius of $2\farcs2$ from the star, oriented roughly NNE−SW (see their Fig. 2). In Figure 4.1 we display PSF-subtracted 8 − 12 μm MIRAC3 images reproduced from Schuster (2007). These images probe the sub-arcsecond scale closer to the star, within the region masked out in de Wit et. al's PSF-subtracted 24.5 μm image. Schuster found an extended envelope around the star in all three filters. The envelope has a position angle of $\sim 105°$ East of North, which is roughly perpendicular to the 24.5 μm bipolar-type nebula. As Schuster noted, this envelope is the likely source of μ Cep's 10 μm silicate emission feature.

On the arcminute scale, we can trace μ Cep's earlier mass loss detected in cooler

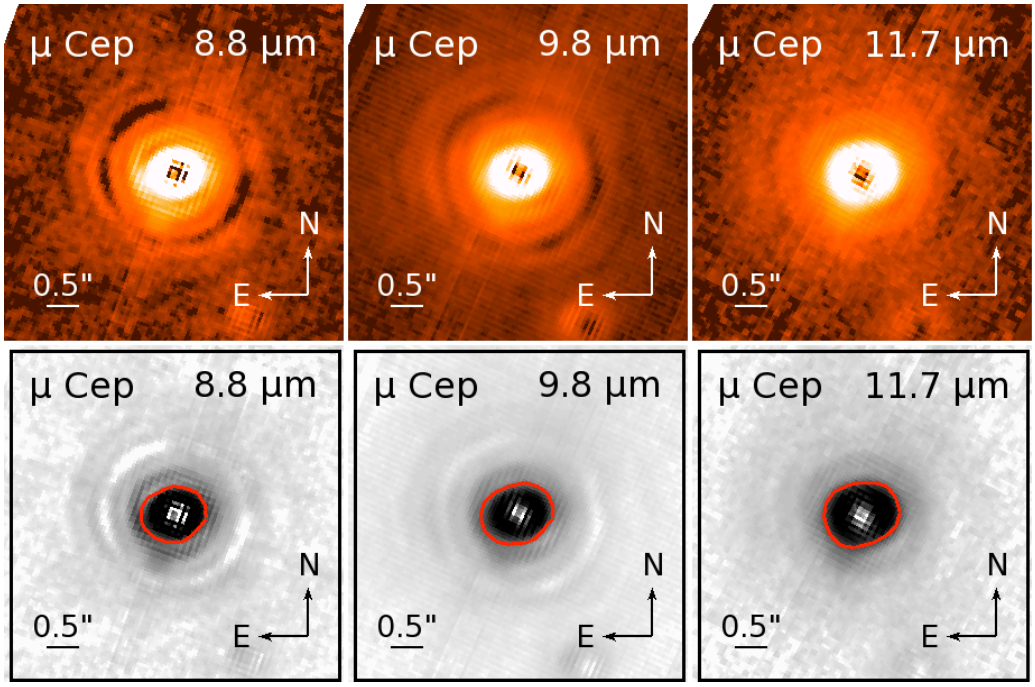

Figure 4.1 – μ Cep: Mid-IR high resolution AO images. **Top row:** PSF-subtracted MIRAC3 images at 8.8, 9.8 and 11.7 μm reproduced from Figure 4.3 of Schuster (2007). The images have been rotated to display North up, East left and the intensity is square-root scaled to emphasize extended emission. **Bottom row:** Same images in grey-scale, each with an overlaid contour indicating an extended envelope at a position angle of $\sim$ 105° (roughly East-West).

dust. Our SOFIA/FORCAST images in Figure 4.2 show extended emission out to a radius of 20″ around the star, with a particularly noticeable extension to the East out to about 25″. This extension is in the same direction as the larger nebula around μ Cep seen in the *Herschel* PACS images at 70 and 160 μm presented by Cox et al. (2012). In Figure 4.3 we overlay contours from our 37.1 μm FORCAST image on the 70 μm image, in which the nebula extends out to about 1.′5 to the southeast. Cox et al. analyzed this nebula as a bow-shock caused by μ Cep's stellar wind interacting with the ISM. Given the traditional assignment of μ Cep to membership in the Cep OB2 association (Humphreys, 1978), an alternate possibility is that its wind may be shaped by the UV flux from nearby OB stars, as for example is the case with the bean-shaped circumstellar nebula of NML Cyg (Schuster et al., 2009). However, de Zeeuw et al.'s (1999) analysis of *Hipparcos* proper motions in the region containing Cep OB2 excluded μ Cep from membership in the association. The extent of the nebula indicates that μ Cep has lost mass over at least the past several thousand years.

Mass-Loss Rate

We combine our SOFIA/FORCAST 37.1 image with DUSTY models in order to compute μ Cep's mass-loss rate. For the stellar spectrum we use a Castelli & Kurucz (2004) ATLAS9 model stellar atmosphere with $T_\star = 3750$ K and surface gravity $\log g = 0$ appropriate for a red supergiant. We adopt an inner shell boundary dust temperature of 1000 K, a commonly assumed sublimation temperature for silicate grains. We assume that the outer radius of the dust shell is a factor of 10^3 larger than the inner radius. This temperature and size produce a shell extending out to approximately 2′, consistent with the extent of the nebula seen in the PACS 70 μm image. We explored DUSTY models that (1) reproduce μ Cep's observed spectral energy distribution (SED) and (2) predict an average intensity profile at 37.1 μm that follows the observed profile when convolved with the FORCAST PSF. For fitting μ Cep's SED in Figure 4.4 we combine visual & near-IR photometry from Lee (1970) and Heske (1990), which we de-redden assuming an interstellar extinction of $A_V = 2.0$ (Neckel et al., 1980; Levesque et al., 2005; Rowles & Froebrich, 2009). We also plot the ISO SWS (de Graauw et al., 1996) spectrum (Justtanont et al. (1997), Obs ID 08001274) and ISO LWS spectrum (Obs ID 22002005, PI: M. Barlow). For convolving the DUSTY model intensity profile in order

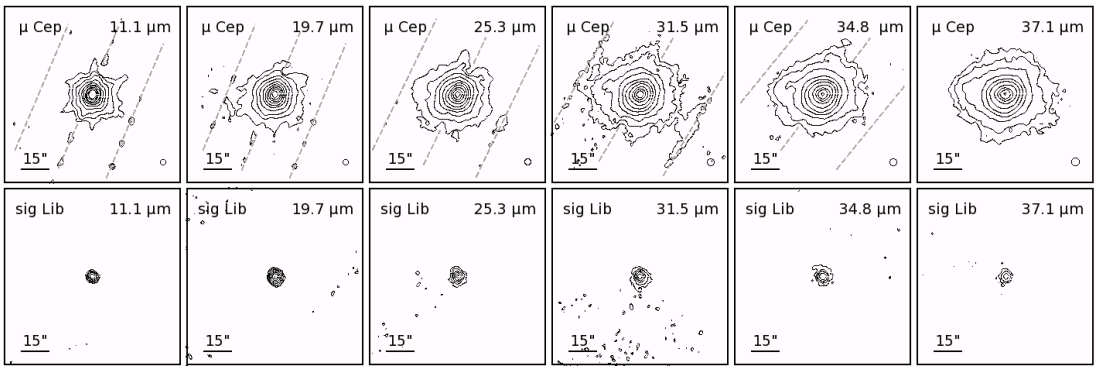

Figure 4.2 – μ Cep: Far-IR SOFIA/FORCAST images. **Top row:** Intensity contours of μ Cep in each of the FORCAST filters listed in Table 1, with central wavelengths indicated in each panel. Each f.o.v. is $90'' \times 90''$ with North up, East left. The lowest contour is at 3-σ above background, with each contour a factor of 2 above the preceding contour. From shortest to longest wavelength the surface brightness of the 3-σ contour is 45.9, 19.4, 7.4, 3.0, 2.8, and 1.9 $\times$ 10^{-20} W cm^{-2} arcsec^{-2}, respectively. The circle in the lower right of each frame represents the beam-size (FWHM of PSF) in that filter for that flight. The grey dashed lines in each of the 11.1 $-$ 34.8 μm images indicates horizontal on the array at the time of observation in that filter. Cross-talk from the negative images in the chop-nod pairs caused faint enhancement and/or suppression of intensity along these lines. It is mitigated but not completely removed by the data reduction pipeline. The enhancements/suppressions along these lines are distinguishable as point-like artifacts smaller than the beam size. **Bottom row:** Standard star σ Lib observed on the same flight (#167), with lowest contour at 3-σ above background, with each contour a factor of 2 above the preceding contour.

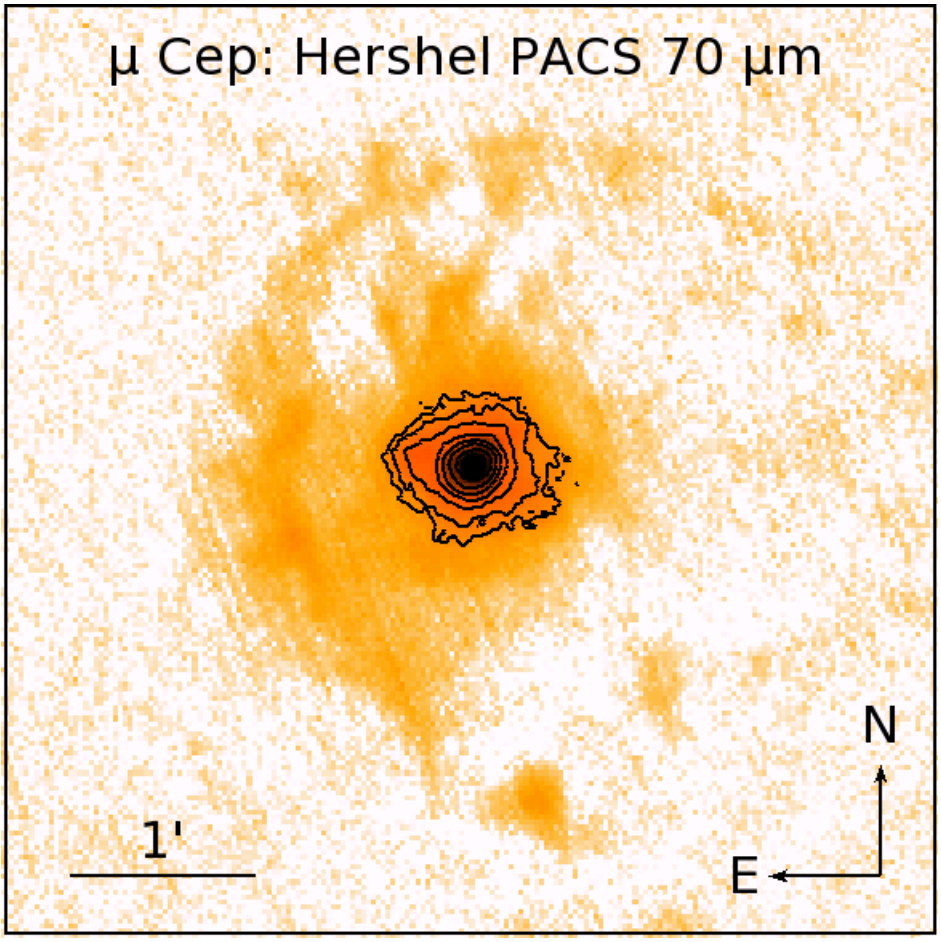

Figure 4.3 – μ Cep: *Herschel* PACS 70 μm image showing its extensive circumstellar nebula (previously published in Cox et al., 2012). The overlaid contours are from the SOFIA/FORCAST 37.1 μm image (see previous figure), which show the same preferential extension towards the East.

to compare it to the observed average 37.1 μm profile we construct a convolution kernel from observations of the asteroid Juno taken on subsequent FORCAST flights during the same flight series. This kernel better captures the wings of the FORCAST PSF at 37.1 micron than the observations of standard star σ Lib, due to the asteroid's higher flux in the far-IR. This helps ensure that we do not unnecessarily attribute the broad observed profile of μ Cep to enhanced mass-loss merely through underestimating the light profile of the star.

For the dust optical properties we use the "warm" circumstellar silicates from Ossenkopf et al. (1992), and assume the grain radii follow an MRN size distribution $n(a) \propto a^{-3.5}\ da$ (Mathis et al., 1977) with $a_{min} = 0.005$ μm and $a_{max} = 0.25$ μm. We assume a power law dust mass density distribution $\rho(r) \propto r^{-q}$ with a single index q throughout the shell. We scale model SEDs to match μ Cep's dereddened visual flux, adjusting the optical depth to achieve a satisfactory fit to the SED across the mid-to-far IR range while also reproducing the observed average intensity profile at 37.1 μm. We explored a range of optical depths and a range of power law indices $q \leq 2$. A power law index of $q = 2$ fits the SED very well through $\lambda \approx 12$ μm, but produces insufficient cooler dust to explain the long wavelength end of the observed SED (see Figure 4.4, blue dashed line). Moreover, the $q = 2$ case fails to adequately reproduce the broad radial profile of the 37.1 micron intensity image (see Figure 4.5, blue dashed line). We find that a density distribution of $\rho(r) \propto r^{-1.8}$ provides both a much better fit to the far-IR SED and the observed radial profile of the intensity (red solid lines in Figures 4.4 & 4.5).

Adopting an expansion velocity of $v_{exp} = 35$ km s^{-1} from the width of its CO lines (De Beck et al., 2010) yields a dynamical age of 13,000 yr for this shell model. If we assume this velocity is constant throughout the shell, then per §3.1 above for this best-fit case with density power law index $q = 1.8$ the mass-loss rate $\dot{M}(t)$ has *decreased* from 5×10^{-6} $M_\odot$ yr^{-1} to $\sim 1 \times 10^{-6}$ $M_\odot$ yr^{-1} over this time period. Alternately, if we simply integrate the density distribution throughout the shell to compute a total mass and divide by this age for the shell, we obtain an average mass-loss rate of $\langle \dot{M} \rangle \approx 4 \times 10^{-6}$ $M_\odot$ yr^{-1}. This rate exceeds the 9×10^{-7} $M_\odot$ yr^{-1} found from its IRAS 60 μm excess (Jura & Kleinmann, 1990a), and the 4.5×10^{-7} $M_\odot$ yr^{-1} found by de Wit et al. (2008), though it is in good agreement with the 2×10^{-6} $M_\odot$ yr^{-1} found by De Beck

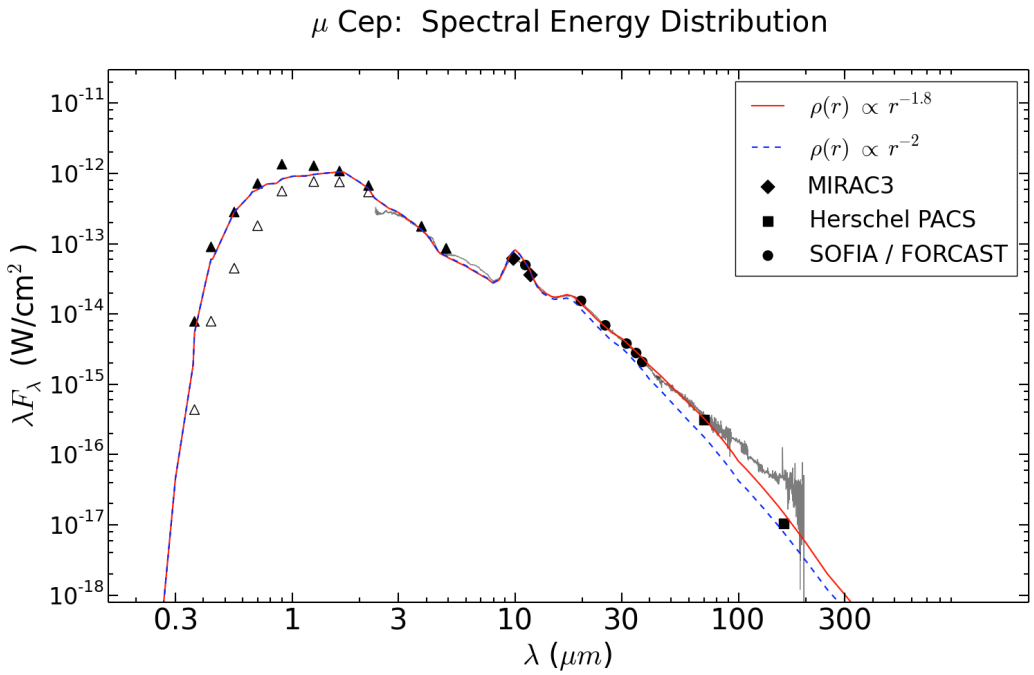

Figure 4.4 – μ Cep: Spectral Energy Distribution. The open triangles are observed (reddened) visual and near-IR photometry; the filled triangles are the same after dereddening for $A_V = 2.0$. The grey lines are ISO SWS and LWS spectra. The filled diamonds are fluxes from the MIRAC3 images (this work). The filled circles are the color-corrected SOFIA/FORCAST observations (this work), integrated out to the 3-σ level in each image to include the extended nebular emission. The filled squares at 70 and 160 μm are the color-corrected PACS fluxes obtained from integrating all nebular emission above the 3-σ level. The blue dashed line is a DUSTY model for dust density distribution $\rho(r) \propto r^{-2}$, i.e., a constant mass-loss rate $\dot{M}$. A better fit to the observed SED is obtained for a distribution $\rho(r) \propto r^{-1.8}$ (red solid line).

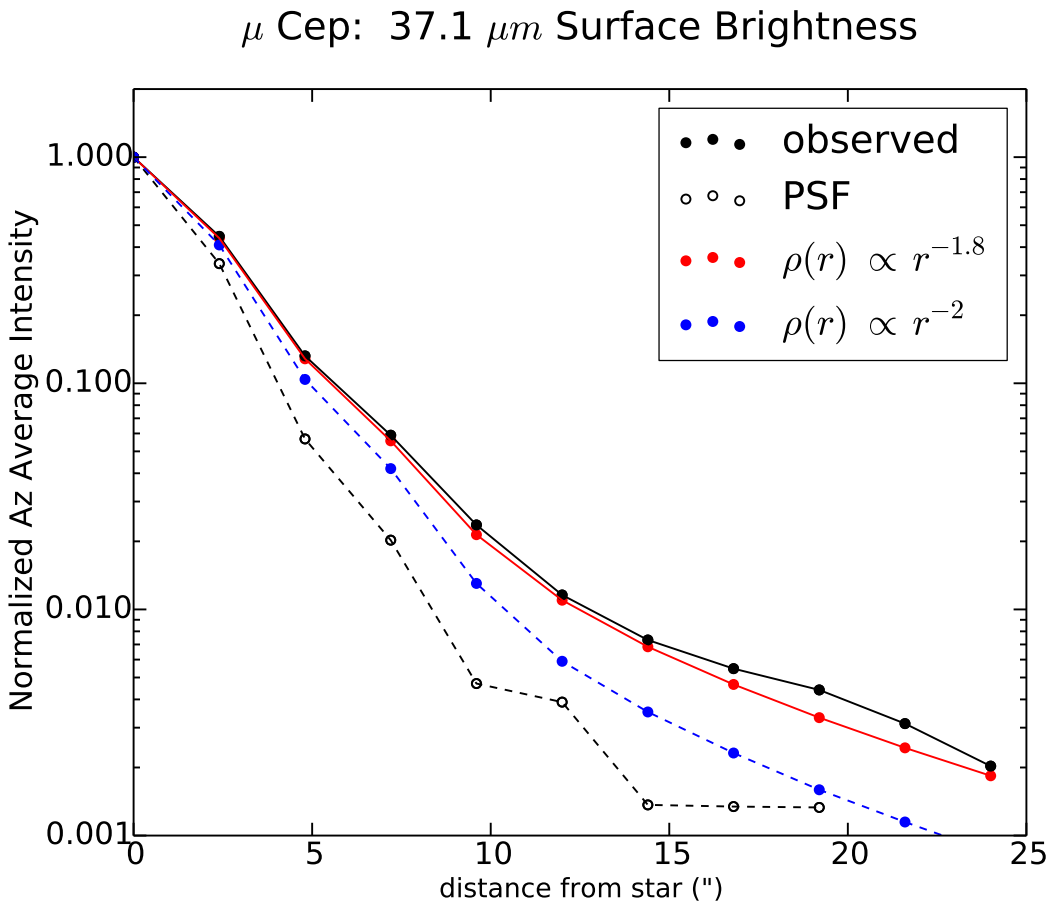

Figure 4.5 – μ Cep: Comparison of DUSTY model intensity profiles after convolution with PSF (black dashed line). The solid black line is the observed azimuthal average intensity in the SOFIA/FORCAST 37.1 μm filter. A $\rho(r) \propto r^{-2}$ density distribution (blue dashed line) does not predict sufficient intensity to match the observed profile. A better fit is obtained assuming a dust density distribution $\rho(r) \propto r^{-1.8}$ (red solid line). For the latter case the average mass-loss rate over the 13,000 yr age of the shell is $\langle \dot{M} \rangle \approx 4 \times 10^{-6}\ M_{\odot}\ \mathrm{yr}^{-1}$.

et al. from modeling its CO line emission. Our rate is about half that of the $10^{-5} M_{\odot}$ yr^{-1} found by Gehrz & Woolf (1971) based on modeling its 11 μm emission, with the difference most likely attributable to our model using a gas-to-dust ratio that is 40% of the value used in that work and/or differences in the grain opacity used. In general all investigations of μ Cep's mass-loss rate using various methods have found it is lower than average compared to other high-luminosity RSGs (see e.g., Figure 3 of Mauron & Josselin, 2011).

4.3.3 VY CMa

Multi-wavelength *HST* visual imaging of the red hypergiant VY CMa has revealed extensive, asymmetric mass-loss within the past 500 - 1000 years, dominated by multiple spatially and kinematically distinct features, indicating independent ejection events from highly localized regions of the star (Smith et al., 2001; Humphreys et al., 2005, 2007). Three of the most prominent ejections, the Northwest Arc, Arc 1 and Arc 2 (see Figures $1 - 4$ of Humphreys et al., 2007), each contain roughly 3×10^{-3} $M_{\odot}$ of gas and dust, which accounts for about 10% of the total ejected mass of $0.2 - 0.4$ $M_{\odot}$ in the nebula out to a radius of $6''$. At the same time, Keck/HIRES spectra showed that the more diffuse uniformly distributed gas and dust is surprisingly stationary, with little or no velocity relative to the star. On this basis Humphreys et al. (2005) argued that the high mass loss rate of $\sim 10^{-4}$ $M_{\odot}$ previously found for VY CMa is an average measure of the mass carried out by these specific ejections accompanied by streams or flows of gas through low-density regions in the dust envelope. The unusually diverse molecular chemistry of VY CMa's circumstellar envelope appears to be directly related to this history of independent, localized ejections, with certain species of molecules associated with the distinct blue-shifted and red-shifted features in the ejecta (Ziurys et al., 2007; De Beck et al., 2015). The star's recent history continues to show strong, discrete mass loss events. High resolution near-IR imaging and polarimetry found the more recently ejected "Southwest Clump" feature ($\sim 1\farcs5$ from the star) to be optically thick to scattering out to 5 μm with a total mass (gas + dust) of at least 5×10^{-3} $M_{\odot}$ (Shenoy et al., 2013, 2015). Most recently, ALMA sub-millimeter observations resolved prominent dust components even closer to the star, with the brightest component (dubbed component "C") having a total mass of gas and dust of at least 2.5×10^{-4} $M_{\odot}$ (O'Gorman et al.,

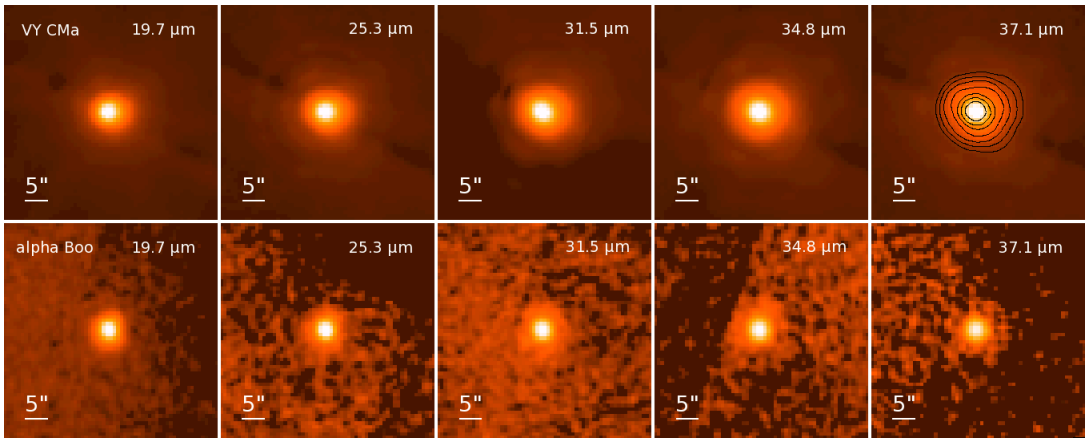

Figure 4.6 – VY CMa: Far-IR SOFIA/FORCAST images. **Top row:** VY CMa in each of the FORCAST filters listed in Table 1, with central wavelengths indicated in each panel. Each f.o.v. is $45'' \times 45''$ with North up, East left. The intensity is square-root scaled. **Bottom row:** Standard star α Boo observed on the same flight (#154). The contours on the 37.1 μm image of VY CMa are the same contours overlaid on the *HST* image in Figure 4.7.

2015).

VY CMa's appearance in the SOFIA/FORCAST images (Figure 4.6) is broader than a point-source, although in contrast to μ Cep we find no evidence of a long history of mass loss. Interestingly, the appearance of the FORCAST image follows the general shape seen in the visual. In Figure 4.7 we show intensity contours from the FORCAST 37.1 μm image overlaid on the *HST* visual image from Smith et al. (2001). The FORCAST images are extended towards the northwest and southwest in the same directions as the prominent Northwest Arc and Arc 1 seen in the scattered visual light, which were ejected $\sim$ 400 and 900 yr ago respectively. The NW Arc and Arc 1 are expanding at 40 and 50 km s^{-1} respectively relative to the star, into uniformly distributed gas and dust that is either stationary or only slowly expanding away (Humphreys et al., 2005). The extension of the longer wavelength FORCAST images in the same directions may indicate that cooler dust lost earlier is being swept up by these more recent, fast moving ejections. The 37.1 μm image is extended in the east and northeast directions as well, in the direction of a dark cloud where the extinction is especially high and is responsible for its asymmetric shape in the visual (see Figure 9 of Smith et al., 2001; Montez et al.,

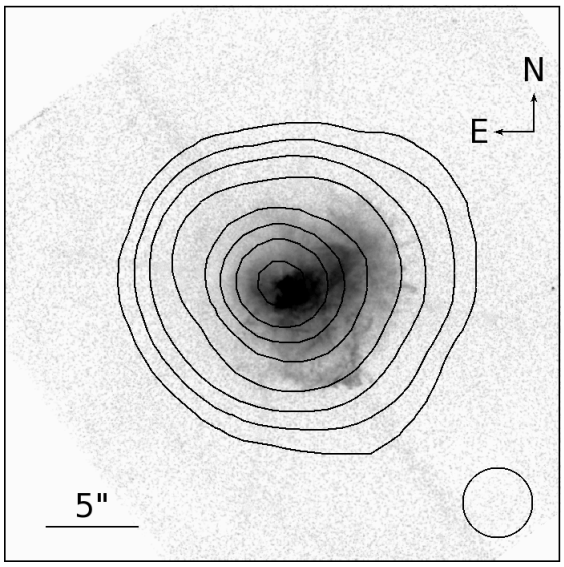

Figure 4.7 – VY CMa: FORCAST 37.1 μm total intensity contours from top right of Figure 4.6 overlaid on *HST* F547M ($\lambda_0 = 0.55$ μm) visual image reproduced from Smith et al. (2001). The f.o.v. is $30'' \times 30''$ with North up, East left. The circle in the lower right represents the FORCAST 37.1 μm beam size (PSF FWHM = $3\farcs7$). The extension towards both the northwest and southwest indicates cooler dust not detectable in scattered light. The extensions in these directions correspond to the directions of ejection of the features respectively named as the NW Arc and Arc 1 by Humphreys et al. (2007) (see their Fig. 3, the second-epoch *HST* F547M image).

2015). Thermal emission at 37.1 μm is able to penetrate this obscuring dust.

We estimate VY CMa's mass-loss rate with an elementary DUSTY model. Given VY CMa's highly asymmetric nebula seen in the optical and near-IR, the assumption of spherical symmetry is obviously a simplification. Previous studies have applied radiative transfer models that include a circumstellar disk and a variety of viewing angles, and/or a range of mineralogies for the dust, with a thorough exploration presented in Harwit et al. (2001). At the resolution of our FORCAST images, however, spherical symmetry is an acceptable assumption that should provide an accurate average mass-loss rate. As seen in Figure 4.8, VY CMa's SED is highly reddened. The interstellar reddening towards it is estimated at no more than $A_V = 1.5$, the value we have used to de-redden the optical and near-IR photometry (open triangles). It is thus clear that the very red energy distribution is mostly due to circumstellar extinction (see also Appendix of

Humphreys et al., 2007). For our DUSTY model we use an ATLAS9 stellar atmosphere with $T_\star = 3500$ K (Wittkowski et al., 2012). We find that we cannot fit the FORCAST and PACS fluxes with any model using silicate grains alone. We are able to fit the long-wavelength end of its spectrum if we assume a grain mixture that is 50-50 silicates and metallic Fe, with the same iron optical constants used by Harwit et al. (2001). We use a grain size distribution $\propto a^{-3.5}$, though we find that to account for the broad, rising spectrum beyond the near-IR we require large grains capable of scattering in the $2 - 5$ μm range. We use an upper-end grain radius of $a_{max} = 5$ μm. Increasing the maximum grain radius from the submicron scale has minimal impact on our computed mass-loss rate since the dominant contribution to the opacity comes from the smallest grains in the distribution. We first attempted to fit the SED assuming a constant mass-loss rate density distribution of $\rho(r) \propto r^{-2}$ but found it inadequate to explain the far-IR flux. Our best-fit model displayed in Figure 4.8 assumes $\rho(r) \propto r^{-1.5}$ throughout a shell with an outer radius of $10''$. Although it underpredicts the visual fluxes and strength of the $3 - 8$ μm region relative to the 10 μm silicate feature, our model fits reasonably well to the JHK range where the effect of ISM reddening is the least uncertain and provides a very good fit to the FORCAST and PACS fluxes.

For this best-fit model the optical depth $\tau(37.1\ \mu\text{m}) = 0.17$. Assuming a 100:1 gas-to-dust mass ratio, we compute a total mass of 0.7 $M_\odot$ in the nebula. To determine the average mass-loss rate, we estimate the age of the $10''$ radius model shell using a constant expansion velocity. Assuming a constant expansion velocity is an approximation, since the Keck/HIRES spectra showed that a single uniform expansion velocity is not found throughout the nebula (Humphreys et al., 2005). That work found the large arcs to the northwest and southwest expanding at $40 - 50$ km s^{-1}, while the more uniformly distributed gas showed little or no motion. Very close to the star ($< 0\farcs4$), the proper motion of H_2O masers indicates an expansion velocity of 27 km s^{-1} per Richards et al. (1998) (rescaled for $D = 1.2$ kpc per Zhang et al., 2012). De Beck et al. (2010) found an expansion velocity of ~ 47 km s^{-1} based on the widths of CO lines in the circumstellar envelope. We adopt this last value as an average velocity, since CO molecules are found throughout the circumstellar envelope. This yields an age of $\Delta t = 1200$ yr for the $10''$ radius model shell. The resulting average mass-loss rate is $\langle \dot{M}_{tot} \rangle \approx 6 \times 10^{-4}\ M_\odot$ yr^{-1}. Since this is an average rate, it does not capture the higher short-term rates on the order

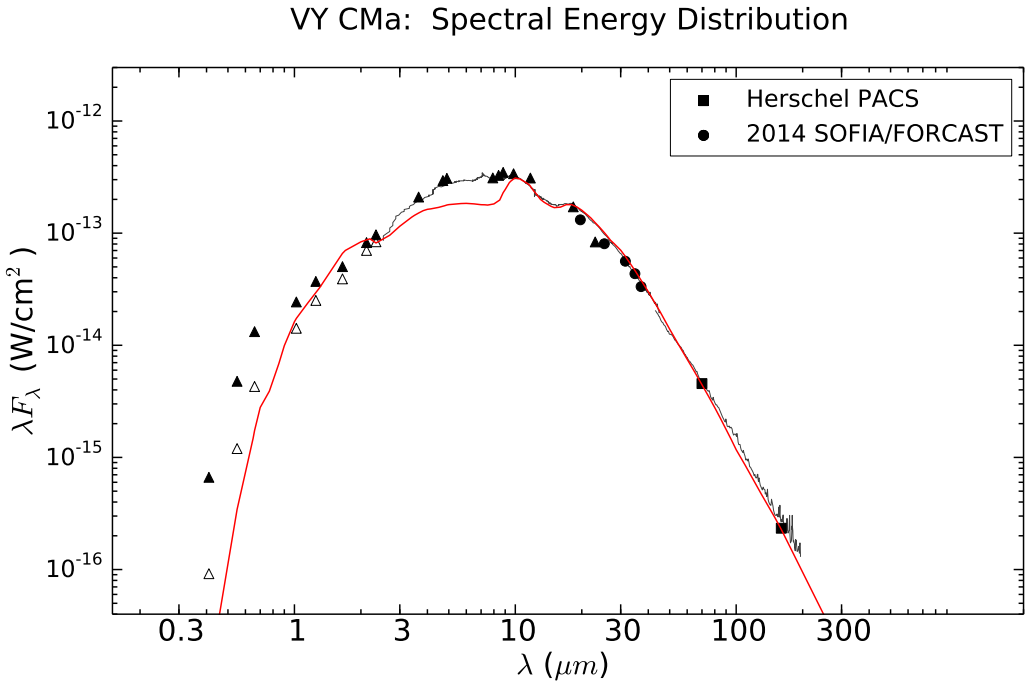

Figure 4.8 – VY CMa: Spectral Energy Distribution. The triangles are photometry from Smith et al. (2001), with the open triangles showing the observed values prior to de-reddening for $A_V = 1.5$. The grey solid lines are the ISO-SWS spectrum (Harwit et al., 2001) and the ISO-LWS spectrum (Polehampton et al., 2010). The black circles are the color-corrected fluxes measured from the SOFIA/FORCAST observations using an aperture of radius = 12″. The 6% uncertainty from the flux calibration is smaller than the plotted symbol. The black squares at 70 and 160 μm are the color-corrected fluxes from the PACS images. The red solid line is the DUSTY model fitted to the SED, yielding an average mass-loss rate of $\langle \dot{M} \rangle \approx 6 \times 10^{-4}\ M_\odot\ \mathrm{yr}^{-1}$.

of 10^{-3} $M_{\odot}$ yr^{-1} associated with the NW Arc and Arcs 1 and 2 (Humphreys et al., 2005). Our average rate is within the same range of several $\times$ 10^{-4} $M_{\odot}$ yr $^{-1}$ found by previous studies (Danchi et al., 1994; Knapp, 1985; De Beck et al., 2010).

4.3.4 IRC +10420

Previous Visual, Near-IR and Sub-Millimeter Studies

IRC +10420 is one of a few intermediate temperature stars defining the empirical upper luminosity boundary in the H-R Diagram. With $L \sim 5 \times 10^{-5} L_{\odot}$, its A-F type spectrum and extensive visible ejecta make it a special example of post-RSG evolution (Humphreys et al., 2002). Jones et al. (1993) used visual polarimetry to determine that most of the extinction towards IRC +10420 is interstellar; combining the polarimetry with the reddening of its optical SED and radial velocity they established a distance of $\sim$5 kpc. *HST* visual imaging reveal a very complex multi-stage mass loss history, with one or more reflection shells at $5'' - 6''$ that were probably ejected during the star's previous RSG stage (Humphreys et al., 1997), while the near environment within a radius of $2''$ shows many jet-like structures, rays and arcs in the ejecta. For radii from $2''$ to $5''$, Humphreys et al. used the surface brightness of the visual scattered light to estimate $\dot{M} \sim 2.4 \times 10^{-4} M_{\odot}$ yr^{-1}. Most interestingly, they found evidence of enhanced mass-loss at a rate of $\sim 10^{-3} M_{\odot}$ yr^{-1} based on the near-IR scattered light within $1''$ of the star, suggesting a very high mass loss stage within the past 400 years that has recently ceased. Second epoch *HST*/WFPC2 imaging combined with *HST*/STIS long-slit spectroscopy showed that the many numerous arcs, knots and condensations in the inner region were ejected at different times in different directions, but were all nearly in the plane of the sky (Tiffany et al., 2010). Thus we view IRC +10420 nearly pole-on. This geometry has been confirmed by interferometry of Brγ emission from neutral and ionized gas around the star (Oudmaijer & de Wit, 2013) and by high-resolution adaptive optics 2.2 μm imaging polarimetry (Shenoy et al., 2015).

Mass-Loss History: Mid-to-Far-IR Imaging

IRC +10420 has one of the strongest 10 μm silicate emission features among the hypergiants. With MIRAC4 we can probe the sub-arcsecond scales where this emission

originates. In Figure 4.9 we show the MIRAC4 8.7, 9.8 and 11.9 μm images of IRC +10420 along with comparisons to the PSF star α Her. Subtraction of the PSF leaves circularly symmetric extended emission out to a radius of $\sim 1\farcs5$ in all three filters. The extended emission does not show the NE-SW preference previously seen at the same wavelengths with similar resolution in Humphreys et al. (1997) and Meixner et al. (1999). It is likely that some of the strong 10 μm silicate emission arises from this extended envelope.

Farther from the star, the *HST* visual images showed the ejecta separated into distinct, approximately spherical shells at $5'' - 6''$ from the star. The long-exposure *HST* F675W image also showed evidence of more distant ejecta as much as $8'' - 9''$ away (see Figure 5 of Tiffany et al., 2010), which is also seen in the near-IR in J-band polarimetry (Kastner & Weintraub, 1995). Our FORCAST images in Figure 4.10 probe a similar angular extent in radius, with emission in the longest filters detected out to a radius of $\sim 10''$. The *HST* visual observations showed a pronounced enhancement of the mass-loss towards the southwest of the star. This morphology is seen in our FORCAST images as well, as shown in Figure 4.11 where we overlay the FORCAST 37.1 μm intensity contours on the *HST* visual image from Tiffany et al. (2010). Sub-millimeter observations find extension in the same direction as well (Dinh-V.-Trung et al., 2009).

To explore IRC +10420's mass-loss history we use DUSTY to model its SED, requiring the models to account for the substantial extended emission seen in the 11.9 μm MIRAC4 image out to a radius of $\sim 2''$. To build its SED, in Figure 4.12 we compile photometry from the optical through L$'$ (3.8 μm) from Jones et al. (1993), Oudmaijer et al. (1996) and Humphreys et al. (2002), which we de-redden assuming $A_V = 6$. For the mid-to-far IR we include color-corrected fluxes from the IRAS and MSX Point Source catalogs as well as the ISO SWS spectrum (Obs ID 12801311) as processed by Sloan et al. (2003) and the ISO LWS spectrum from Lloyd et al. (2003) (Obs ID 72400605). To this we add the photometry from our SOFIA/FORCAST images and the *Herschel*/PACS images.[6] The conventional stellar effective temperature is ill-defined for IRC +10420 (Humphreys et al., 2002), though a value between 8000 − 8500 K is

[6] The good agreement between the trend of our FORCAST photometry and the start of the LWS spectrum indicate that the discontinuity between the end of the SWS spectrum and the start of the LWS spectrum is an artifact of the (Sloan et al., 2003) reprocessing of the SWS spectrum, as previously noted by Ladjal et al. (2010).

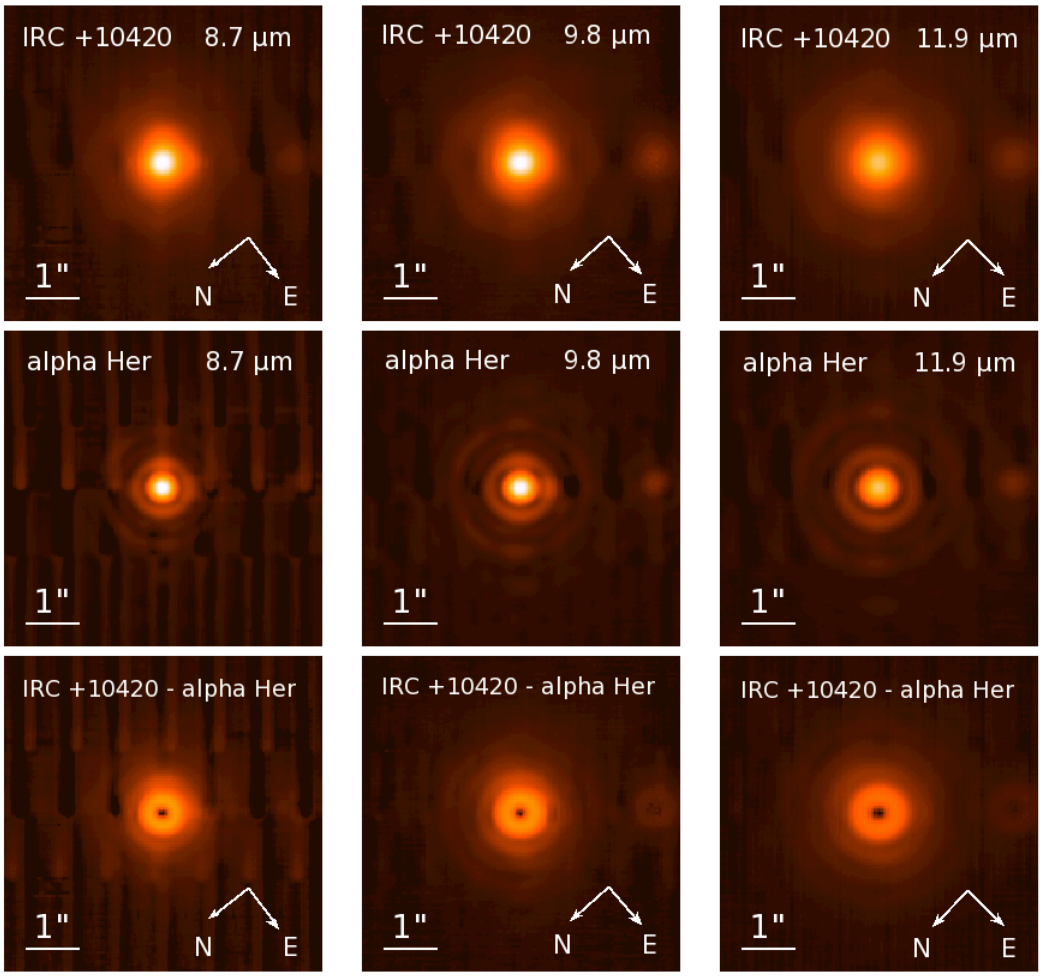

Figure 4.9 – IRC +10420: Mid-IR high resolution images. **Top row:** MMT/MIRAC4 adaptive optics thermal infrared images of IRC +10420 at 8.7, 9.8 and 11.9 μm taken on UT 2008 Jun 16. The intensity is square-root scaled. **Middle row:** Same, for the PSF star α Her observed immediately after IRC +10420 at similar airmass. The first minima in the Airy ring patterns occur at radii of $0\farcs40$, $0\farcs45$, and $0\farcs53$ in the 8.7, 9.8 and 11.9 μm filters respectively. For comparison the diffraction limits ($1.22\lambda/D$) are $0\farcs34$, $0\farcs38$, and $0\farcs46$ respectively at those wavelengths for the 6.5-m MMT aperture. **Bottom row:** IRC +10420 after subtraction of the scaled PSF image, stretched to the same maximum intensity as the corresponding top row image. A clear excess of extended emission around the star is present out to a radius of $\sim 2''$ in all three filters.

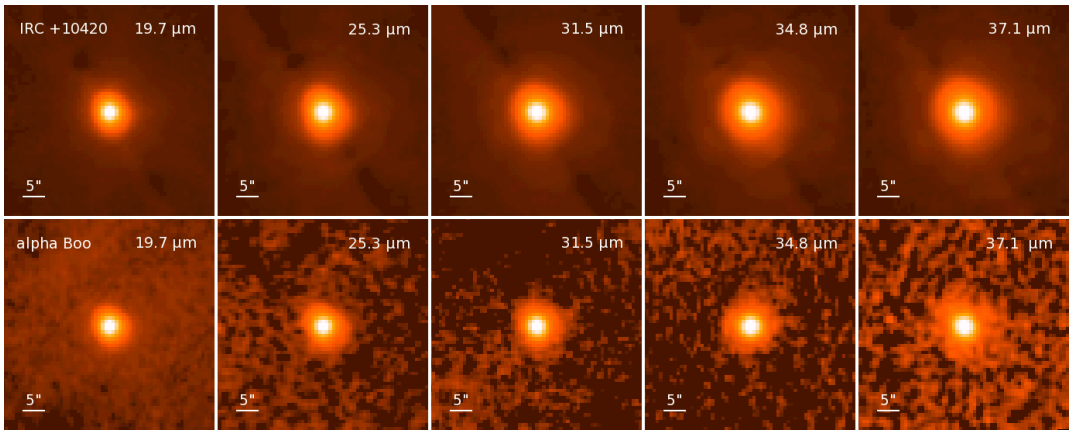

Figure 4.10 – IRC +10420: Far-IR SOFIA/FORCAST images. **Top row:** IRC +10420 in each of the FORCAST filters listed in Table 1, with central wavelengths indicated in each panel. Each f.o.v. is $45'' \times 45''$ with North up, East left. The intensity is square-root scaled. **Bottom row:** Standard star α Boo observed on the same flight (#177).

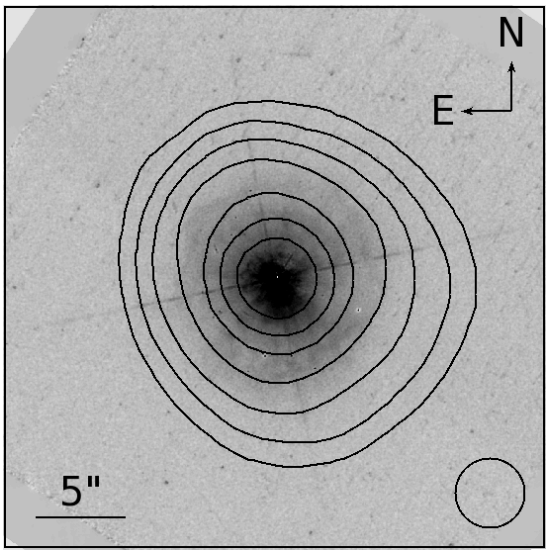

Figure 4.11 – IRC +10420 37.1 μm total intensity contours from top right of Figure 4.10 overlaid on *HST* F547M ($\lambda_0 = 0.55$ μm) visual image reproduced from Tiffany et al. (2010). The f.o.v. is $30'' \times 30''$ with North up, East left. The circle in the lower right represents the FORCAST 37.1 μm beam size (PSF FWHM = $3\farcs9$). The extension towards the southwest coincides with the enhancement in the mass loss in that direction seen in both the visual and sub-millimeter.

likely (see e.g., Klochkova et al., 1997). We therefore use a Castelli & Kurucz (2004) ATLAS9 model stellar atmosphere with $T_\star = 8250$ K. We find that to reproduce the broad, flat spectrum observed in the $\sim 2 - 7$ μm range we require the dust temperature at the inner radius of the shell be no hotter than 800 K; a hotter dust condensation temperature cannot account for this portion of the SED. We therefore adopt 800 K and again assume the dust to be the circumstellar silicates from Ossenkopf et al. (1992). We do not attempt to reproduce the exact shape of IRC +10420's wide, flat-topped 10 μm silicate feature seen in the ISO SWS spectrum. A flattened profile can indicate large grains with diameters approaching the micron size range (e.g., van Boekel et al., 2005), or self-absorption due to the optical depth approaching unity at this wavelength. IRC +10420's complex ejecta may combine regions of silicate emission and (self) absorption which are not captured by the assumption of spherical symmetry.

We first attempt to fit IRC +10420 with a constant mass-loss rate density distribution $\rho(r) \propto r^{-2}$ for a shell extending out to $\sim 10''$. Such a model is unable to account for the observed radial intensity profile out to $\sim 2''$ at 11.9 μm, in addition to failing to fit the SED beyond 12 μm. Previous studies applying radiative transfer models to IRC +10420 (Oudmaijer et al., 1996; Blöcker et al., 1999; Lipman et al., 2000) have similarly considered and rejected a constant mass-loss rate. We find that to fit the inner $2''$ profile at 11.9 μm requires a shallower slope to the density distribution. We obtain a good fit to this profile with a single density power law index of $q = 1.4$ throughout the shell. However, even with the shallower slope this still fails to produce sufficient flux in the FORCAST range and beyond. The total energy re-radiated in that range indicates there is a substantial amount of dust with temperatures of approximately 100 − 150 K. To account for this cooler component to our model, we introduce a factor of 5 enhancement in the dust density around the star at a radius of $\sim 3''$. This piece-wise density profile is depicted in Figure 4.13b with a red solid line. The actual distribution of cooler dust around the star is likely more complex than just a single second shell at this radius. We choose to use a single enhancement as the simplest way to explain the SED in the FORCAST range rather than attempting to introduce multiple shells. The resulting fits to the SED and 11.9 μm intensity profile are depicted with red solid lines in Figures 4.12 and 4.13a respectively.

The duration of the mass-loss period attributed to the formation of the ejecta for

this best-fit model depends on the expansion velocity adopted. As with VY CMa, assuming a single expansion velocity is a simplification in the case of IRC +10420 since the expansion velocity varies throughout its envelope. In particular, *HST*/STIS long-slit spectroscopy by Humphreys et al. (2002) demonstrated the H gas within 2″ is expanding at 50 − 60 km s^{-1} in a roughly spherical arrangement, while other spectral lines indicated a combination of outflow and infall of material at different velocities. With this caveat in mind, we adopt as an average expansion velocity the value of 40 km s^{-1} determined from CO line widths (Oudmaijer et al., 1996; De Beck et al., 2010), which yields an age $\Delta t = 6000$ yr for the 10″ radius model shell. We integrate each of the two parts of the density profile in Figure 4.13b with our assumed 100:1 gas-to-dust mass ratio, finding masses of 7.1 and 0.2 $M_\odot$ respectively in the outer and inner parts. The resulting average mass-loss rates are $\langle \dot{M} \rangle \approx 2 \times 10^{-3}$ $M_\odot$ yr^{-1} for the period from 6000 until about 2000 yr ago, with a lower rate of $\sim 1 \times 10^{-4}$ $M_\odot$ yr^{-1} within the past 2000 yr. These rates are indicated on Figure 4.13b for the two periods, with time plotted on the top axis. Exactly when the transition from a higher to a lower rate took place is admittedly somewhat uncertain; our introduction of a single, steep density enhancement 2000 yr ago is only an approximation to what was likely a more gradual transition. It is clear however that some substantial change in the rate of mass loss has occurred in the past several thousand years, since a single shell density profile that adequately accounts for the inner 2″ cannot explain the large excess flux in the FORCAST range (see blue-dashed line in Figure 4.12). This supports the view that IRC +10420 is a post-RSG hypergiant which shed considerable mass during its previous stage as an RSG and will continue to evolve rapidly blueward across the upper HR Diagram. For comparison, we note that our higher mass-loss rate for the outer ejecta is within a factor of 2 of the rate of 3.6×10^{-3} $M_\odot$ yr^{-1} found by De Beck et al. (2010) from modeling of multiple CO lines.

4.3.5 ρ Cas

The yellow hypergiant ρ Cas is famous for its historical and recent "shell" episodes in 1946, 1985, and 2000 during which it temporarily develops TiO bands in a cool, optically thick wind, after which it returns to its F supergiant spectrum (Popper, 1947; Bidelman & McKellar, 1957). During the 2000 event it shed mass at a high rate of

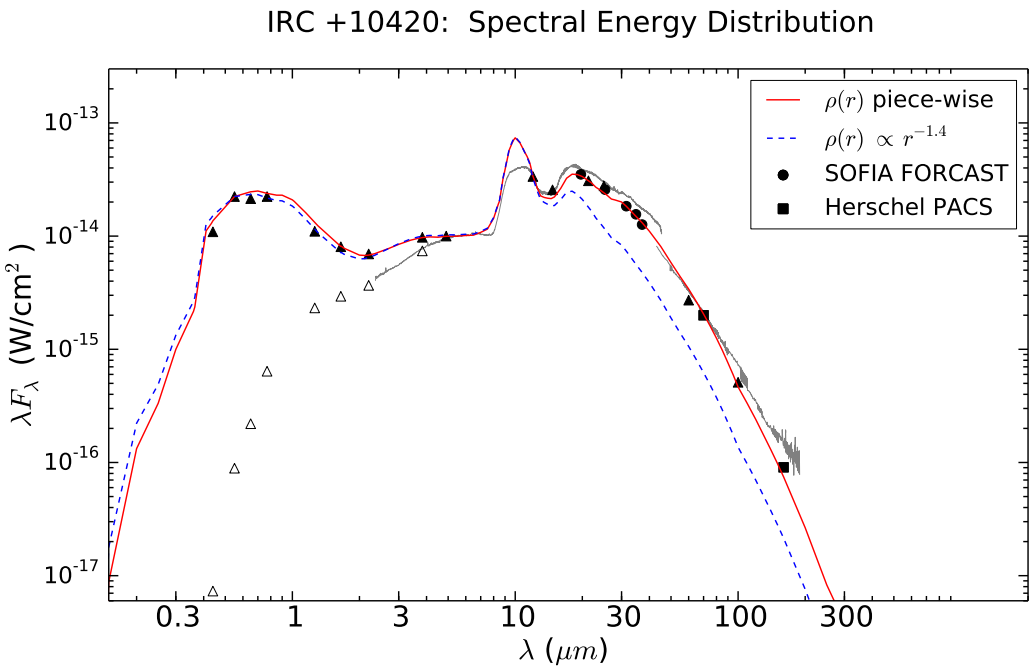

Figure 4.12 – IRC +10420: Spectral Energy Distribution. The black triangles are point-source photometry compiled from Jones et al. (1993), Oudmaijer et al. (1996), Humphreys et al. (2002) and the IRAS and MSX Point Source Catalogs (with color correction). The thin grey lines are the ISO SWS and LWS spectra. The black circles are the color-corrected fluxes measured from the SOFIA/FORCAST observations using an aperture of radius = 10″. The assumed 6% uncertainty from the flux calibration is smaller than the plotted symbol. The black squares at 70 and 160 μm are the color-corrected fluxes from the *Herschel*/PACS images. The blue dashed line is a DUSTY model for a density distribution $\rho(r) \propto r^{-1.4}$ throughout the shell, which adequately fits the SED through $\sim$ 12 μm but falls off too rapidly at longer wavelengths. The red solid line is the best-fit model, constructed using the same power-law index but with a density enhancement as depicted in the next figure.

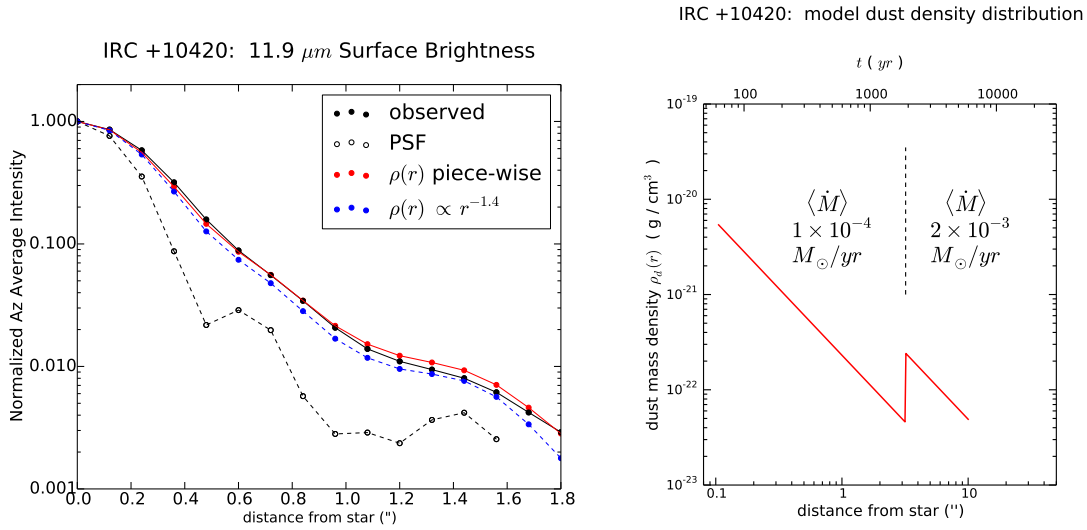

(a) (b)

Figure 4.13 – IRC +10420. **(a):** DUSTY model intensity profiles after convolution with PSF (dashed line). The solid black line is the observed azimuthal average intensity in the MIRAC4 11.9 μm filter. A constant mass-loss rate (not pictured) fails to produce sufficient intensity in the inner 2″ of IRC +10420's circumstellar environment. A density power law index of $q = 1.4$ provides a good fit to the observed profile in this inner region. **(b):** The best fit DUSTY model density profile $\rho(r) \propto r^{-1.4}$, for which a factor of 5 enhancement in density is added at a radius of 3″ to account for the long-wavelength flux on the SED. The average mass-loss rate for the earlier period spanned by the shell from 6000 to 2000 yr ago is $\langle \dot{M} \rangle = 2 \times 10^{-3}\ M_\odot\ \mathrm{yr}^{-1}$, while the average rate more recently is $1 \times 10^{-4}\ M_\odot\ \mathrm{yr}^{-1}$.

Table 4.3. DUSTY Model Inputs & Average Mass-Loss Rates

Target	D (kpc)	$T_\star$ (K)	r_1 (arcsec, AU)	r_2 (arcsec, AU)	$T_d(r_1)$ (K)	$\tau_{37.1}$	$\kappa_{37.1}$[a] (cm^2 g^{-1})	v_{exp}[b] (km s^{-1})	Δt[c] (yr)	$\langle \dot{M} \rangle$[d] ($M_\odot$ yr^{-1})
μ Cep	0.87	3750	0.″11 (96 AU)	110″ (96000 AU)	1000	0.0029	194	35	13000	$(3.8 \pm 0.3) \times 10^{-6}$
VY CMa	1.2	3500	0.″12 (140 AU)	10″ (12000 AU)	800	0.165	195	47	1200	$(5.6 \pm 0.6) \times 10^{-4}$
IRC +10420 (past 2000 yr)	5	8250	0.″10 (500 AU)	10″ (50000 AU)	800	0.026	194	40	2000	$(1.3 \pm 0.3) \times 10^{-4}$
IRC +10420 ($>$ 2000 yr)										$(1.8 \pm 0.3) \times 10^{-3}$

Note. — Columns r_1 and r_2 are the inner and outer radii of the model shell, with $T_d(r_1)$ being the assumed dust temperature at r_1.

[a] Opacity at 37.1 μm for the grain distribution used for each source as discussed in Sections 4.3.2 (μ Cep), 4.3.3 (VY CMa), and 4.3.4 (IRC +10420).

[b] Assumed average expansion velocity from widths of CO lines per De Beck et al. (2010).

[c] Dynamical age of the shell $\Delta t = r_2 \ / \ v_{exp}$. For IRC +10420 the average mass-loss rate is computed for two periods over the 6000 yr dynamical age of the shell, with the recent period spanning 2000 yr and the earlier period spanning 4000. See Figure 4.13b.

[d] Average mass-loss rate computed using the adopted gas-to-dust mass ratio of 100:1 (see footnote # 5 above). The uncertainty is estimated from the range of optical depths that reproduce the FORCAST $30 - 40$ μm fluxes to within $\pm$20%.

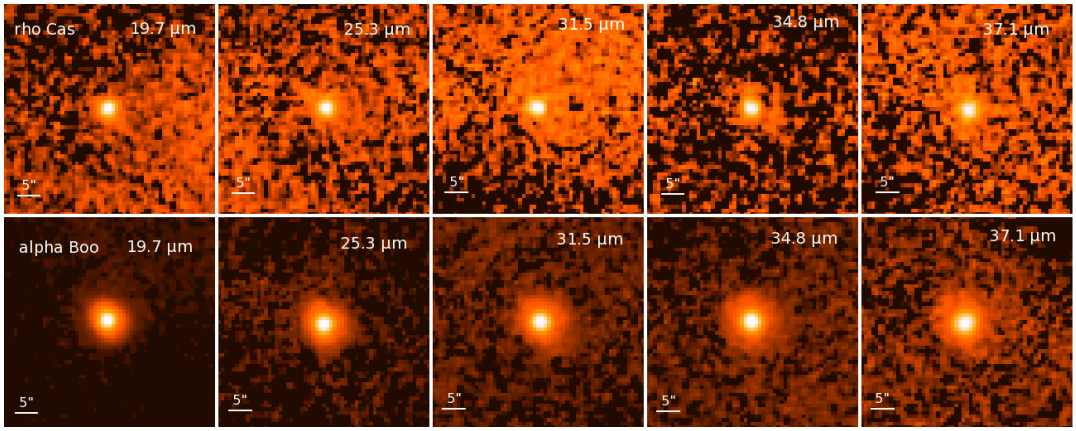

Figure 4.14 – ρ Cas: Far-IR SOFIA/FORCAST images. **Top row:** ρ Cas in each of the FORCAST filters listed in Table 4.1, with central wavelengths indicated in each panel. Each f.o.v. is $45'' \times 45''$ with North up, East left. The intensity is square-root scaled. **Bottom row:** Standard star α Boo observed on the same flight (#156).

3×10^{-2} $M_{\odot}$ for ~ 200 days (Lobel et al., 2003). The 1946 event was accompanied by a dimming in photographic magnitude of $\Delta m \approx 1.5$ for several months (Beardsley, 1961), believed to be associated with a burst of ejected material. With its spectroscopic and photometric variability, and enhanced abundances, ρ Cas is considered to be a post-RSG like IRC +10420. However, it is not a known strong infrared or maser source and *HST* images also did not reveal any extended ejecta (Schuster et al., 2006). Near-IR ground-based photometry from $2.2 - 12.6$ μm obtained between $1969 - 1973$ did not show any evidence of infrared excess above the photospheric level (Gillett et al., 1970; Hackwell & Gehrz, 1974). Subsequently, Jura & Kleinmann (1990b) analyzed IRAS observations taken in 1983 and found a measurable infrared excess above the photospheric level in the 12, 25 and 60 μm bands. Even after color-correction to account for the broad bandpasses of the IRAS filters the excess flux was twice that of the photospheric level at 12 and 25 μm. They modeled this IR excess as flux from an optically thin shell of dust, presumed to have condensed between 1973 and 1983 as a result of the 1946 ejection. Their fit to the IRAS 12, 25 and 60 μm fluxes indicated a dust temperature of 600 K for an assumed emissivity $\propto \lambda^{-0.5}$, corresponding to a shell radius of 270 AU.

We examine the time evolution of this shell model in comparison with photometry

from our FORCAST images (Figure 4.14), evolving the shell to predict its flux in 2014. The fraction of the star's luminosity absorbed and re-radiated by the shell (the absorption optical depth) decreases as 1 / r^2 as it expands, since the solid angle subtended by each grain at the star decreases by this factor. The shell's bolometric flux in 2014 is therefore determined by scaling its flux in 1983:

$$F_{bol,2014} = F_{bol,1983} \left(\frac{r_{1983}}{r_{2014}} \right)^2 \tag{4.1}$$

where radius $r_{2014} = r_{1983} + v_{exp} \times (31 \text{ yr})$. Jura & Kleinmann estimated an upper limit expansion velocity of $v_{exp} \approx 110$ km s^{-1}, for which the radius $r_{1983} = 270$ AU would have increased to approximately 1000 AU in 2014. $F_{bol,2014}$ would therefore be $\sim 7\%$ of $F_{bol,1983}$. The peak of the shell's λF_λ spectrum would have moved to about 10 μm due to cooling of the grains to $\sim$ 310 K, as their distance from the star increased. On the spectral energy distribution of ρ Cas in Figure 4.15 the blue-dashed line is the sum of the shell's 1983 SED (thin solid blue line) and pre-IRAS photosphere (thin black line). The red dashed-line line is the sum of the same photosphere and the predicted flux of the dust shell in 2014 (thin solid red line). The 2014 observed FORCAST 19.7 $-$ 37.1 μm fluxes are plotted in Figure 4.15 (red points). We also plot additional photometry taken within several years prior to the FORCAST observations: 8.9 and 9.8 μm fluxes from our MIRAC4 images in 2006; color-corrected 9 and 18 μm fluxes recorded by the AKARI satellite survey in 2007; and color-corrected fluxes at 12 and 22 μm fluxes recorded by WISE in 2010. The predicted total flux in 2014 is generally consistent with the observed fluxes through $\sim$25 μm, though it is slightly higher than the observed flux from 25 to 40 μm. Overall the new photometry is consistent with emission from the expanding dust shell ejected in its 1946 eruption, with no evidence of newer dust formation from its more recent eruptions. Future follow-up observations would be worthwhile to see if any new excess is found in the coming decades.

4.4 Summary & Conclusions

μ Cep: We present adaptive optics (AO) diffraction-limited 8 $-$ 12 μm MMT/MIRAC3 images which reveal a circumstellar envelope extending approximately East-West out to $\sim 0\farcs5$ (several tens of stellar radii). This envelope is the likely source of the 10

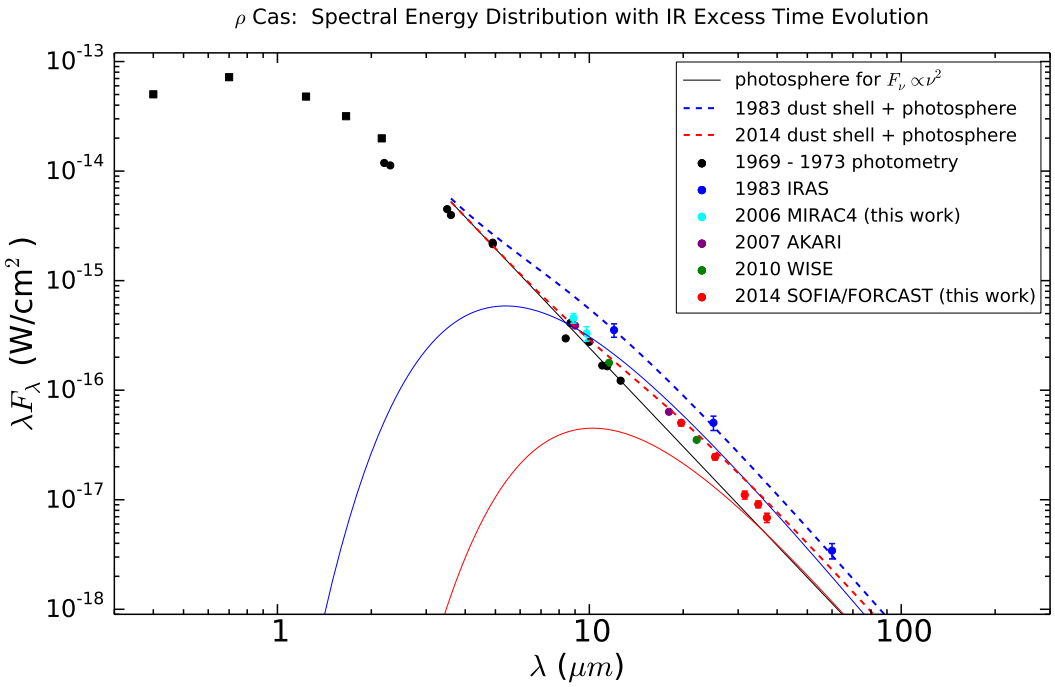

Figure 4.15 – ρ Cas: SED with time-evolution of the optically thin dust shell formed several decades after the 1946 eruption. The black squares are photometry from the US Naval Observatory and 2MASS catalogs. The black circles are 2 −12 μm ground-based photometry from Gillett et al. (1970) and Hackwell & Gehrz (1974). The thin black solid line is the pre-IRAS photosphere level, assumed to scale as $F_\nu \propto \nu^2$ into the far-IR. The blue circles are the color-corrected 1983 IRAS fluxes from Jura & Kleinmann (1990b). The thin blue solid line is the SED of the dust shell for those authors' best-fit model of dust with emissivity $\propto \nu^{0.5}$ and temperature $T_d = 600$ K in 1983. The blue dashed line is the sum of the photosphere and the shell's 1983 SED. The thin red solid line is the shell's predicted SED in 2014 per Equation (4.1), and the red-dashed line is the sum for the same photosphere. The red points are the 19.7 − 37.1 μm fluxes from the 2014 SOFIA/FORCAST observations. Along with photometry from our MIRAC4 images (2006), AKARI (2007) and WISE (2010), these are generally consistent with the continuing thinning (and cooling) of the shell, with no indication of new dust formation from more recent eruptions. The 1-σ uncertainties are smaller than the plotted symbols sizes except for the longest FORCAST wavelengths.

μm silicate feature in μ Cep's SED. Our SOFIA/FORCAST far-IR imaging of μ Cep shows extended emission from $25 - 37$ μm out to $\sim 20''$ around the star, with further extension to $\sim 25''$ to the East in the same direction as the extensive nebula previously revealed in *Herschel* PACS 70 & 160 μm images (Cox et al., 2012).

DUSTY radiative transfer modeling of the 37.1 μm profile and the SED indicate an average mass-loss rate of 4×10^{-6} $M_{\odot}$ yr $^{-1}$, with evidence for a slow decline in mass-loss rate over the 13,000 yr dynamical age of its shell. The range of mass-loss rates is consistent with previous studies finding μ Cep's rate is significantly lower than RSGs of comparable luminosity.

VY CMa: SOFIA/FORCAST images from $19.7 - 37.1$ μm display a morphology which coincides with the general shape of the highly asymmetric nebulae seen in the visual, suggesting thermal emission from dust associated with the expanding arcs to the northwest and southwest. Our best-fit DUSTY model indicates an average mass-loss rate of 6×10^{-4} $M_{\odot}$ yr^{-1}.

IRC +10420: We present adaptive optics (AO) diffraction-limited $8 - 12$ μm MMT/MIRAC4 images which reveal spatially extended, circularly symmetric emission out to a radius of $\sim 2''$. As with VY CMa, the extended shape of IRC +10420 in our SOFIA/FORCAST images coincides with the general shape of the asymmetric nebulae seen in the visual. Our best-fit DUSTY model indicates a change in the average mass-loss rate, with a high average rate of 2×10^{-3} $M_{\odot}$ yr^{-1} from $6000 - 2000$ yr ago during its presumed RSG stage, and a lower average rate of 1×10^{-4} $M_{\odot}$ yr^{-1} in the past 2000 yr.

ρ Cas: Our new $19.7 - 37.1$ μm SOFIA/FORCAST photometry of this yellow hypergiant are consistent with the continued expansion and thinning of the dust shell fitted to the infrared excess observed with IRAS, which was attributed to dust formed as a result of the 1946 eruption. There is no indication of new dust formation from more recent eruptions.

4.5 Acknowledgements

We thank Dr. Willem-Jan de Wit, Dr. Takuya Fujiyoshi and the Subaru/COMICS instrument team for consulting on the orientation of μ Cep's nebula as observed at

24.5 μm. This work has used unpublished data from Michael Schuster's PhD thesis, which is available through the SAO/NASA Astrophysics Data System (ADS) at http://adsabs.harvard.edu/abs/2007PhDT.....28S. Financial support for this work was provided by NASA through award # SOF-0091 to R. M. Humphreys issued by USRA.

Chapter 5

Summary & Future Work

The goal of this thesis was to study the mass-loss histories of hypergiants stars using new capabilities in near-IR imaging and polarimetry, and airborne mid-IR imaging. With LBT/LMIRCam and MMT-Pol on the MMT we have imaged the nebulae of VY CMa and IRC +10420 with sub-arcsecond resolution, revealing recent mass-loss in the close environments around these stars. To probe further into these hypergiants' past history, we have used mid-infrared imaging with SOFIA/FORCAST to search for cold dust and performed 1-D radiative transfer modeling of their SEDs and resolved profiles.

Our $2 - 5$ μm adaptive optics imaging of the cool hypergiant VY CMa penetrates deeper into its dusty nebula than in the optical, probing its recent mass-loss history. In Chapter 2 we analyzed the resolved images of its peculiar "Southwest" Clump, which has no obvious counterpart on the opposite side of the star. The distinct shape of the SW Clump is suggestive of a short-lived, localized event and may be analogous to a coronal mass ejection (CME) from a single location on the Sun's surface. A short-lived ejection event is consistent with the SW Clump appearing as a confined, coherent shape several hundred years after ejection. Using adaptive optics imaging polarimetry, in Chapter 3 we demonstrated the Clump is optically thick through at least 3.1 μm and reaffirmed the lower limit mass of 5×10^{-3} $M_{\odot}$ based on modeling its surface brightness as optically thick scattered light. Our 1.3 μm polarimetry detects several other prominent features of VY CMa's nebula include the NW Arc, Arc 2, S Knot, and S Arc. Using the polarized intensity as a lower limit on total scattered light intensity, we found each of these features to be optically thick as well. Their relatively high intrinsic polarizations

are consistent with their high scattering optical depths since the depolarizing effect of multiple scatters is reduced for typical silicate grain albedos. In Chapter 4, we used 20 $-$ 37 μm infrared imaging with SOFIA/FORCAST to search for evidence of earlier mass loss. VY CMa's morphology at the longest wavelengths coincides with the general shape of the highly asymmetric nebulae seen in the visual, suggesting thermal emission from dust associated with the expanding arcs to the northwest and southwest. Modeling its SED we computed an average mass-loss rate of 6×10^{-4} $M_{\odot}$ yr^{-1} over the past $\sim$1200 years, with no clear evidence of mass loss much farther in its past.

Our study of the warm hypergiant IRC +10420 similarly traced its mass-loss over a range of angular scales. At the sub-arcsecond scale using adaptive optics, in Chapter 3 we used 2.2 μm polarimetry to reveal a relatively uniform nebula largely in the plane of the sky extending out to $2\farcs5$ from the star. This low-latitude ejecta is optically thick. Combining the polarimetry with 3 $-$ 5 μm imaging that shows extended emission, we modeled the flux of this nebula and found its emission is an order of magnitude brighter than can be explained by simple extrapolation of the scattered light seen at 2.2 μm. We hypothesized grains warmed to a temperature higher than the expected grain equilibrium temperature, but consistent with the local gas temperature in this region. In Chapter 4 we presented 8 $-$ 12 μm adaptive optics images that reveal spatially extended emission spanning nearly the same range as the 2.2 μm polarimetry. Applying radiative transfer modeling to the intensity profile of this extended emission and the SED, we found that IRC +10420's mass-loss history is divided into two distinct periods. Our best-fit model showed that it lost mass at a high average rate of 2×10^{-3} $M_{\odot}$ yr^{-1} from 6000 $-$ 2000 yr ago during its presumed RSG stage, followed by an order of magnitude decrease to an average rate of 1×10^{-4} $M_{\odot}$ yr^{-1} in the past 2000 yr.

In addition to VY CMa and IRC +10420, our SOFIA/FORCAST program included the RSG μ Ceph and the warm hypergiant ρ Cas. Our study of μ Cep probes a mass-loss history extending back $\sim$13,000 yr. To match the observed intensity profile of its resolved nebula in FORCAST 25 $-$ 37 μm images, our radiative transfer modeling requires a declining mass-loss rate. We find that over the 13,000 yr dynamical age of the shell, its mass loss-rate has declined from 5×10^{-6} to 1×10^{-6} $M_{\odot}$ yr^{-1}. In contrast to the high mass-loss rate of VY CMa, μ Cep's rate is significantly lower than RSGs of comparable luminosity. In the case of ρ Cas, we demonstrated that our new 19.7 $-$

37.1 μm SOFIA/FORCAST photometry are consistent with the continued expansion and thinning of the dust shell formed as a result of the 1946 eruption. We did not find evidence of new dust formation from more recent eruptions.

In the future, infrared imaging over a range of angular scales will be used to expand the sample of RSGs and post-RSGs with resolved mass-loss. The SOFIA/FORCAST Cycle 3 program 03_0082 (PI: R. Humphreys) included three additional RSG targets (NML Cyg, VX Sgr and S Per) and contingent approval has been granted for observations of the yellow hypergiant HR 5171A during a Cycle 4 Southern deployment if flight scheduling permits. In Fall 2016, VY CMa is scheduled for observation with NOMIC, the $8 - 13$ μm imager on the Large Binocular Telescope. With NOMIC's $0\farcs27$ angular resolution (for single dish observing mode), VY CMa's SW Clump should be resolved. These observations will better sample the Clump's SED and could help resolve the puzzle of its non-detection by ALMA reported in O'Gorman et al. (2015).

The work presented in this thesis has demonstrated the capabilities of MMT-Pol and LMIRCam to resolve circumstellar ejecta around RSGs and post-RSGs. These capabilities will be extended to several recently identified RSG clusters, each of which contains substantial coeval RSG populations. These include RSGC1 (Figer et al., 2006; Davies et al., 2008), RSGC2 = Stephenson 2 (Davies et al., 2007), NGC 7419 (Marco & Negueruela, 2013) and the Per OB1 association, which contains many RSGs in its halo including S Per (Humphreys, 1978). Imaging these clusters of RSGs in polarized intensity in the near-infrared with MMT-Pol will cleanly separate light scattered by dusty nebulae from the stars' light, and when combined with adaptive optics imaging from $3 - 13$ μm with LMIRCam/NOMIC will enable us to trace the RSGs mass-loss. Since the RSG cluster populations are coeval, this will allow the role of high mass loss events on their evolution to be studied.

References

Asaki, Y., Deguchi, S., Imai, H., et al. 2010, ApJ, 721, 267

Barmby, P., Marengo, M., Evans, N. R., et al. 2011, AJ, 141, 42

Beardsley, W. R. 1961, ApJS, 5, 381

Bidelman, W. P., & McKellar, A. 1957, PASP, 69, 31

Biller, B. A., Close, L. M., Li, A., et al. 2005, ApJ, 620, 450

Blöcker, T., Balega, Y., Hofmann, K.-H., et al. 1999, A&A, 348, 805

Bohren, C. F., & Huffman, D. R. 1983, Absorption and Scattering of Light by Small Particles (Wiley-Interscience)

Castelli, F., & Kurucz, R. L. 2004, ArXiv Astrophysics e-prints, astro-ph/0405087

Castro-Carrizo, A., Quintana-Lacaci, G., Bujarrabal, V., Neri, R., & Alcolea, J. 2007, A&A, 465, 457

Chandrasekhar, S. 1950, Radiative Transfer (Dover Books)

Cox, N. L. J., Kerschbaum, F., van Marle, A.-J., et al. 2012, A&A, 537, A35

Cruzalebes, P., Lopez, B., Bester, M., Gendron, E., & Sams, B. 1998, A&A, 338, 132

Danchi, W. C., Bester, M., Degiacomi, C. G., Greenhill, L. J., & Townes, C. H. 1994, AJ, 107, 1469

Davies, B., Figer, D. F., Kudritzki, R.-P., et al. 2007, ApJ, 671, 781

Davies, B., Figer, D. F., Law, C. J., et al. 2008, ApJ, 676, 1016

De Beck, E., Decin, L., de Koter, A., et al. 2010, A&A, 523, A18

De Beck, E., Vlemmings, W., Muller, S., et al. 2015, A&A, 580, A36

de Graauw, T., Haser, L. N., Beintema, D. A., et al. 1996, A&A, 315, L49

de Wit, W. J., Oudmaijer, R. D., Fujiyoshi, T., et al. 2008, ApJ, 685, L75

Decin, L., Hony, S., de Koter, A., et al. 2006, A&A, 456, 549

Dinh-V.-Trung, Muller, S., Lim, J., Kwok, S., & Muthu, C. 2009, ApJ, 697, 409

Draine, B. T. 2003, ApJ, 598, 1017

Draine, B. T., & Lee, H. M. 1984, ApJ, 285, 89

Draine, B. T., & Li, A. 2007, ApJ, 657, 810

Esposito, S., Riccardi, A., Pinna, E., et al. 2012, in Society of Photo-Optical Instrumentation Engineers (SPIE) Conference Series, Vol. 8447, Society of Photo-Optical Instrumentation Engineers (SPIE) Conference Series

Figer, D. F., MacKenty, J. W., Robberto, M., et al. 2006, ApJ, 643, 1166

Fu, R. R., Moullet, A., Patel, N. A., et al. 2012, ApJ, 746, 42

Gehrz, R. D., & Woolf, N. J. 1971, ApJ, 165, 285

Gillett, F. C., Hyland, A. R., & Stein, W. A. 1970, ApJ, 162, L21

Hackwell, J. A., & Gehrz, R. D. 1974, ApJ, 194, 49

Harwit, M., Malfait, K., Decin, L., et al. 2001, ApJ, 557, 844

Herbig, G. H. 1972, ApJ, 172, 375

Herter, T. L., Adams, J. D., De Buizer, J. M., et al. 2012, ApJ, 749, L18

Herter, T. L., Vacca, W. D., Adams, J. D., et al. 2013, PASP, 125, 1393

Heske, A. 1990, A&A, 229, 494

Hinz, P., Arbo, P., Bailey, V., et al. 2012, in Society of Photo-Optical Instrumentation Engineers (SPIE) Conference Series, Vol. 8445, Society of Photo-Optical Instrumentation Engineers (SPIE) Conference Series

Hinz, P. M., Angel, J. R. P., Woolf, N. J., Hoffmann, W. F., & McCarthy, D. W. 2000, in Society of Photo-Optical Instrumentation Engineers (SPIE) Conference Series, Vol. 4006, Interferometry in Optical Astronomy, ed. P. Léna & A. Quirrenbach, 349–353

Hoffmann, W. F., Hora, J. L., Fazio, G. G., Deutsch, L. K., & Dayal, A. 1998, in Society of Photo-Optical Instrumentation Engineers (SPIE) Conference Series, Vol. 3354, Infrared Astronomical Instrumentation, ed. A. M. Fowler, 647–658

Humphreys, R. M. 1978, ApJS, 38, 309

Humphreys, R. M., & Davidson, K. 1979, ApJ, 232, 409

Humphreys, R. M., Davidson, K., Ruch, G., & Wallerstein, G. 2005, AJ, 129, 492

Humphreys, R. M., Davidson, K., & Smith, N. 2002, AJ, 124, 1026

Humphreys, R. M., Helton, L. A., & Jones, T. J. 2007, AJ, 133, 2716

Humphreys, R. M., Pennington, R. L., Jones, T. J., & Ghigo, F. D. 1988, AJ, 96, 1884

Humphreys, R. M., Smith, N., Davidson, K., et al. 1997, AJ, 114, 2778

Humphreys, R. M., Jones, T. J., Polomski, E., et al. 2006, AJ, 131, 2105

Ivezic, Z., & Elitzur, M. 1997, MNRAS, 287, 799

Jones, T. J., Humphreys, R. M., Helton, L. A., Gui, C., & Huang, X. 2007, AJ, 133, 2730

Jones, T. J., Humphreys, R. M., Gehrz, R. D., et al. 1993, ApJ, 411, 323

Jura, M., & Kleinmann, S. G. 1990a, ApJS, 73, 769

—. 1990b, ApJ, 351, 583

Justtanont, K., Yamamura, I., de Jong, T., & Waters, L. B. F. M. 1997, Ap&SS, 251, 25

Kamiński, T., Gottlieb, C. A., Young, K. H., Menten, K. M., & Patel, N. A. 2013, ApJS, 209, 38

Kastner, J. H., & Weintraub, D. A. 1995, ApJ, 452, 833

Klochkova, V. G., Chentsov, E. L., & Panchuk, V. E. 1997, MNRAS, 292, 19

Knapp, G. R. 1985, ApJ, 293, 273

Knapp, G. R., Sandell, G., & Robson, E. I. 1993, ApJS, 88, 173

Ladjal, D., Justtanont, K., Groenewegen, M. A. T., et al. 2010, A&A, 513, A53

Lee, T. A. 1970, PASP, 82, 765

Leisenring, J. M., Skrutskie, M. F., Hinz, P. M., et al. 2012, in Society of Photo-Optical Instrumentation Engineers (SPIE) Conference Series, Vol. 8446, Society of Photo-Optical Instrumentation Engineers (SPIE) Conference Series

Levesque, E. M., Massey, P., Olsen, K. A. G., et al. 2005, ApJ, 628, 973

Lipman, E. A., Hale, D. D. S., Monnier, J. D., et al. 2000, ApJ, 532, 467

Lloyd, C., Lerate, M. R., & Grundy, T. W. 2003, ISO Technical Note 17 (Madrid: ISO Data Centre)

Lobel, A., Dupree, A. K., Stefanik, R. P., et al. 2003, ApJ, 583, 923

Marco, A., & Negueruela, I. 2013, A&A, 552, A92

Marengo, M., Evans, N. R., Barmby, P., et al. 2010, ApJ, 709, 120

Mathis, J. S., Rumpl, W., & Nordsieck, K. H. 1977, ApJ, 217, 425

Mauron, N., & Josselin, E. 2011, A&A, 526, A156

Meixner, M., Ueta, T., Dayal, A., et al. 1999, ApJS, 122, 221

Merrill, P. W., & Wilson, O. C. 1956, ApJ, 123, 392

Meynet, G., Chomienne, V., Ekström, S., et al. 2015, A&A, 575, A60

Monnier, J. D., Tuthill, P. G., Lopez, B., et al. 1999, ApJ, 512, 351

Montez, Jr., R., Kastner, J. H., Humphreys, R. M., Turok, R. L., & Davidson, K. 2015, ApJ, 800, 4

Muller, S., Dinh-V-Trung, Lim, J., et al. 2007, ApJ, 656, 1109

Neckel, T., Klare, G., & Sarcander, M. 1980, A&AS, 42, 251

O'Gorman, E., Vlemmings, W., Richards, A. M. S., et al. 2015, A&A, 573, L1

Ossenkopf, V., Henning, T., & Mathis, J. S. 1992, A&A, 261, 567

Oudmaijer, R. D., Davies, B., de Wit, W.-J., & Patel, M. 2009, in Astronomical Society of the Pacific Conference Series, Vol. 412, The Biggest, Baddest, Coolest Stars, ed. D. G. Luttermoser, B. J. Smith, & R. E. Stencel, 17

Oudmaijer, R. D., & de Wit, W. J. 2013, A&A, 551, A69

Oudmaijer, R. D., Groenewegen, M. A. T., Matthews, H. E., Blommaert, J. A. D. L., & Sahu, K. C. 1996, MNRAS, 280, 1062

Packham, C., Jones, T. J., Warner, C., et al. 2012, in Society of Photo-Optical Instrumentation Engineers (SPIE) Conference Series, Vol. 8446, Society of Photo-Optical Instrumentation Engineers (SPIE) Conference Series

Pilbratt, G. L., Riedinger, J. R., Passvogel, T., et al. 2010, A&A, 518, L1

Planck Collaboration, Adam, R., Ade, P. A. R., et al. 2014, ArXiv e-prints, arXiv:1409.5738

Poglitsch, A., Waelkens, C., Geis, N., et al. 2010, A&A, 518, L2

Polehampton, E. T., Menten, K. M., van der Tak, F. F. S., & White, G. J. 2010, A&A, 510, A80

Popper, D. M. 1947, AJ, 52, 129

Rayner, J. T., Cushing, M. C., & Vacca, W. D. 2009, ApJS, 185, 289

Richards, A. M. S., Yates, J. A., & Cohen, R. J. 1998, MNRAS, 299, 319

—. 1999, MNRAS, 306, 954

Richards, A. M. S., Impellizzeri, C. M. V., Humphreys, E. M., et al. 2014, A&A, 572, L9

Rodigas, T. J., Hinz, P. M., Leisenring, J., et al. 2012, ApJ, 752, 57

Rowles, J., & Froebrich, D. 2009, MNRAS, 395, 1640

Schuster, M. T. 2007, PhD thesis, University of Minnesota

Schuster, M. T., Humphreys, R. M., & Marengo, M. 2006, AJ, 131, 603

Schuster, M. T., Marengo, M., Hora, J. L., et al. 2009, ApJ, 699, 1423

Sellgren, K., Werner, M. W., & Dinerstein, H. L. 1983, ApJ, 271, L13

—. 1992, ApJ, 400, 238

Shenoy, D. P., Jones, T. J., Packham, C., & Lopez-Rodriguez, E. 2015, AJ, 150, 15

Shenoy, D. P., Jones, T. J., Humphreys, R. M., et al. 2013, AJ, 146, 90

Skemer, A. J., Close, L. M., Hinz, P. M., et al. 2008, ApJ, 676, 1082

Skrutskie, M. F., Jones, T., Hinz, P., et al. 2010, in Society of Photo-Optical Instrumentation Engineers (SPIE) Conference Series, Vol. 7735, Society of Photo-Optical Instrumentation Engineers (SPIE) Conference Series

Sloan, G. C., Kraemer, K. E., Price, S. D., & Shipman, R. F. 2003, ApJS, 147, 379

Smith, N., Humphreys, R. M., Davidson, K., et al. 2001, AJ, 121, 1111

Suh, K.-W. 1999, MNRAS, 304, 389

Sylvester, R. J., Skinner, C. J., & Barlow, M. J. 1998, MNRAS, 301, 1083

Tiffany, C., Humphreys, R. M., Jones, T. J., & Davidson, K. 2010, AJ, 140, 339

Tinbergen, J. 1996, Astronomical Polarimetry (Cambridge University Press)

van Boekel, R., Min, M., Waters, L. B. F. M., et al. 2005, A&A, 437, 189

Verhoelst, T., van der Zypen, N., Hony, S., et al. 2009, A&A, 498, 127

Wallerstein, G. 1978, The Observatory, 98, 224

Wardle, J. F. C., & Kronberg, P. P. 1974, ApJ, 194, 249

White, R. L. 1979, ApJ, 230, 116

Wittkowski, M., Hauschildt, P. H., Arroyo-Torres, B., & Marcaide, J. M. 2012, A&A, 540, L12

Zhang, B., Reid, M. J., Menten, K. M., & Zheng, X. W. 2012, ApJ, 744, 23

Ziurys, L. M., Milam, S. N., Apponi, A. J., & Woolf, N. J. 2007, Nature, 447, 1094

Appendix A

Additional MIRAC4 Observations

The observing program with MIRAC included several late type (K through M) giants and supergiants in addition to the observations of μ Cep and IRC +10420 presented in Chapter 4 (see Table 4.2). The observing strategy and data reduction procedure was the same for the MIRAC4 images of IRC +10420 as discussed in §4.2.2. The data (previously unpublished) have been re-reduced and are presented in this Appendix.

Most of the targets have strong 10 μm silicate emission features in their spectra (seen in ISO-SWS and/or ground-based observations, e.g., Sylvester et al. (1998)). Of the seven additional targets imaged at high angular resolution with MIRAC4 in the 8 − 12 μm range, extended emission is seen in five of the sources (S Per, T Per, RW Cep, BD +24 3902, and RW Cyg), while two did not show noticeable extension (ρ Cas and W Per).

S Per: Extended Emission Similar to μ Cep

The RSG S Per (Sp. Type M3-4e Ia) is an OH/IR source and a member of the Per OB1 association (Humphreys, 1978), with a distance of 2.4 ± 0.1 kpc as determined by VLBI H_2O maser astrometry (Asaki et al., 2010). Schuster et al. (2006) presented *HST* images showing that the star is embedded in an elongated circumstellar envelope with a position angle of $\sim 20^\circ$ E of N with a FWHM of $\sim 0\farcs1$ (240 AU). Those authors

noted that the extent and orientation of this envelope match the regions of H_2O maser emission found by Richards et al. (1999), and that it could be explained by bipolarity in the ejecta or a flattened circumstellar halo. The MIRAC4 images at 8.9 and 9.8 μm presented in Figure A.1 show an extended shape as well, similar to that seen in the case of μ Cep (compare Figure 4.1). Fitting elliptical Gaussians to S Per's MIRAC4 images yields a mean position angle of 19° ± 2° E of N, matching very closely the orientation seen in the *HST* images.

Sources with Extended Emission Similar to IRC +10420: T Per, RW Cep, BD +24 3902, and RW Cyg

Four RSG sources appear extended with circularly symmetric emission: T Per, RW Cep, BD +24 3902 and RW Cyg. Their MIRAC4 images are displayed in Figures A.2, A.3, A.4, and A.5 respectively. T Per is an M2 Iab RSG belonging to the Per OB1 association (Humphreys, 1978). RW Cep is an irregular variable RSG with its reported spectral type ranging from M0 0-Ia (Merrill & Wilson, 1956) to K5 0-Ia (Humphreys et al., 1988) to K2 0-Ia (Rayner et al., 2009). BD +24 3902 (Sp. Type M1 Ia) is an RSG member of the Vul OB 1 association, and RW Cyg (Sp. Type M3-4 Ia-Iab) is an RSG member of the Cyg OB 9 association (Humphreys et al., 1988). The extended emission seen in varying degrees in these four sources resembles that of IRC +10420 (compare Figure 4.9). As shown in the case of IRC +10420 in §4.3.4 and Figure 4.13a, such broad profiles may indicate variation in the recent mass-loss history of these stars.

Sources With Little or No Apparent Extension: ρ Cas & W Per

Finally, included for comparison are the MIRAC4 images of two sources which did not reveal noticeable extended emission: the yellow hypergiant ρ Cas and the RSG W Per, displayed in Figures A.6 and A.7

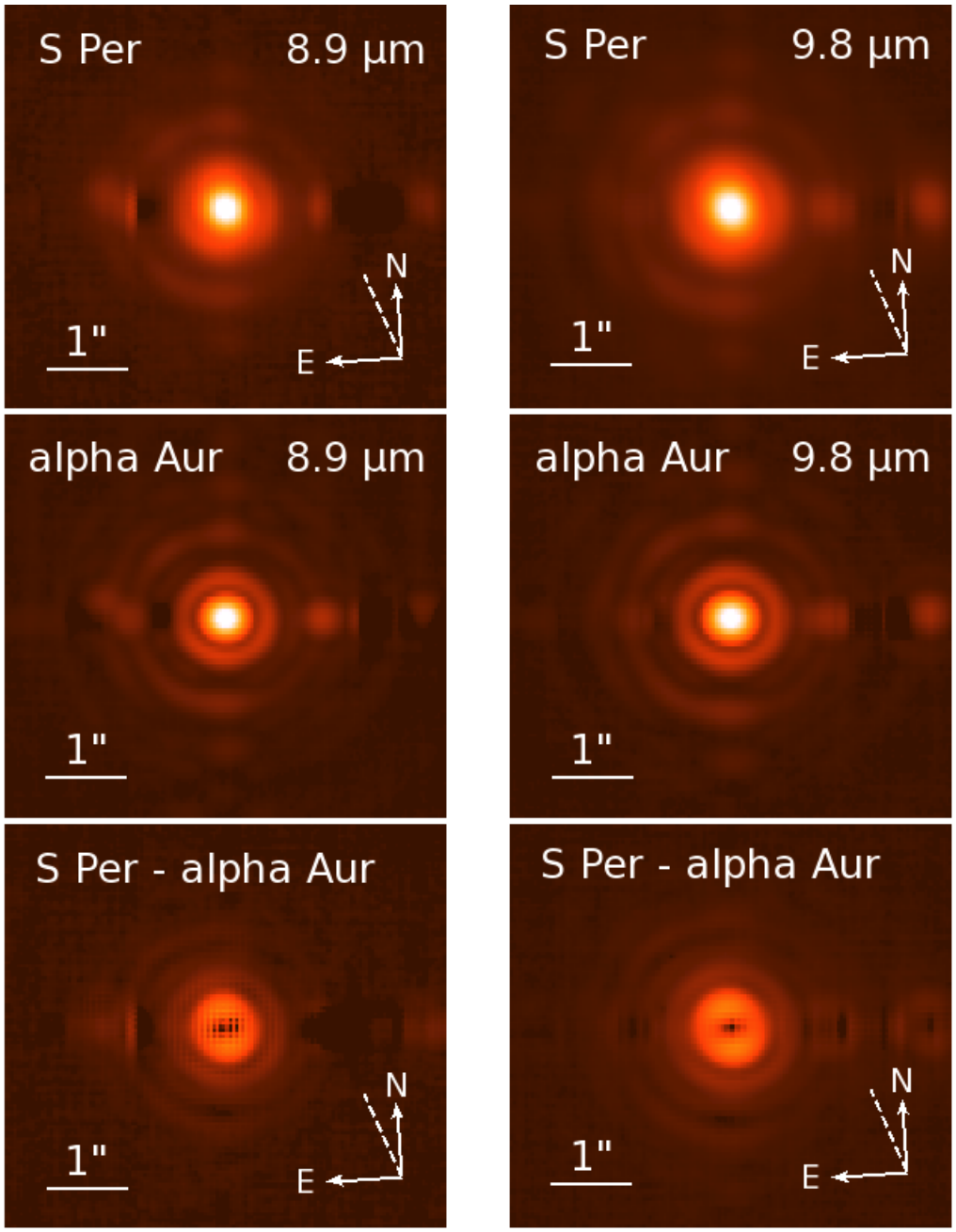

Figure A.1 – MIRAC4 images of S Per before and after PSF subtraction. The directions to North and East are indicated. The pixel scale is 0.037″ pix^{-1}. The dashed white line at position angle 20° E of N shows the approximate orientation of the extended envelope seen in the *HST* visual images (see Figure 8 of Schuster et al. (2006)), which coincides with the direction of extension seen with MIRAC.

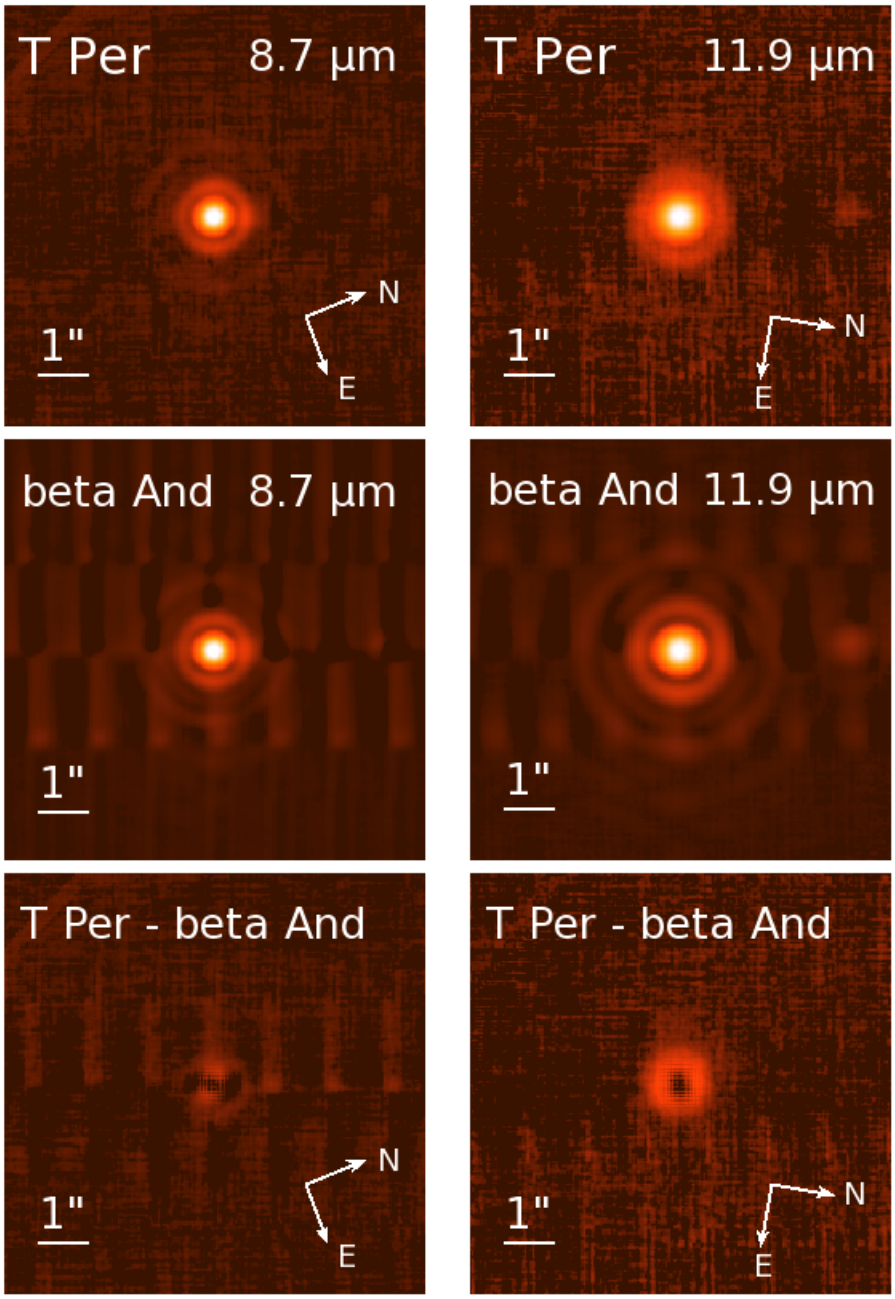

Figure A.2 – MIRAC4 images of T Per before and after PSF subtraction. The directions to North and East are indicated. The pixel scale is 0.027″ pix^{-1}.

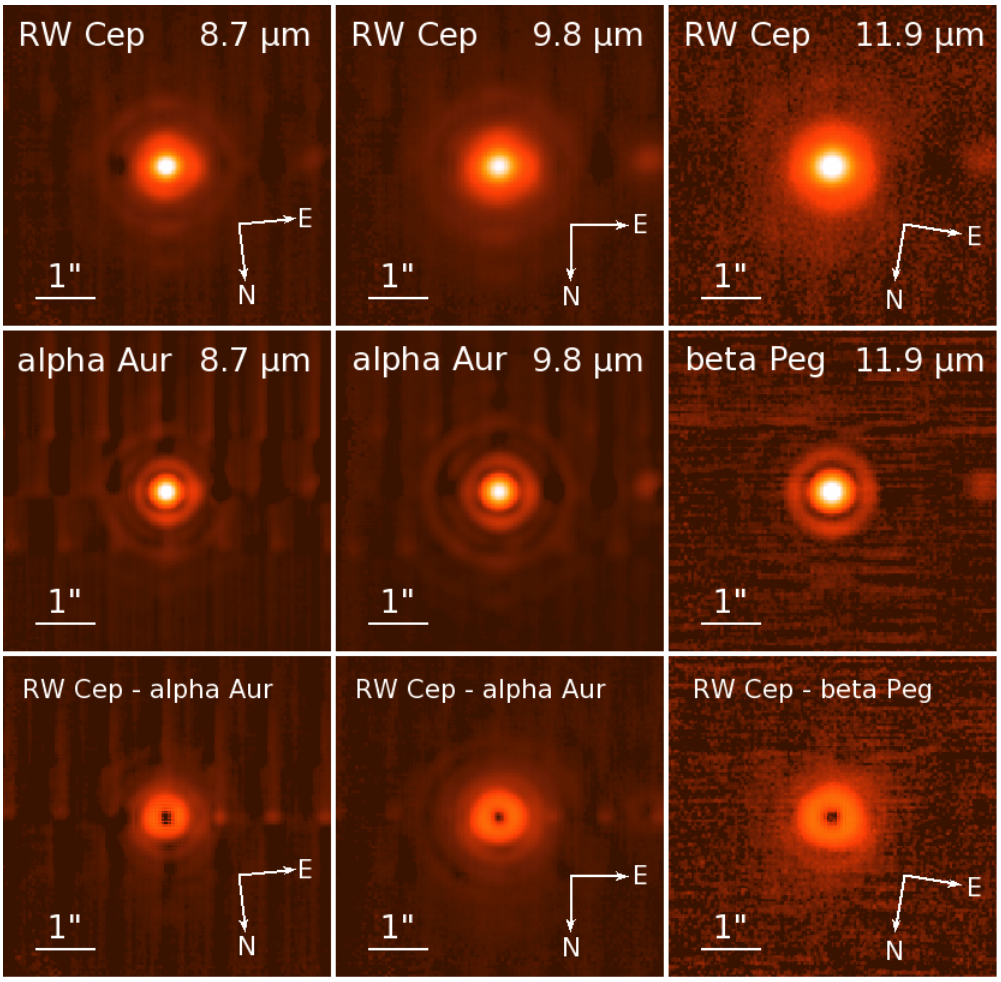

Figure A.3 – MIRAC4 images of RW Cep before and after PSF subtraction. The directions to North and East are indicated. The pixel scale is 0.027″ pix^{-1}.

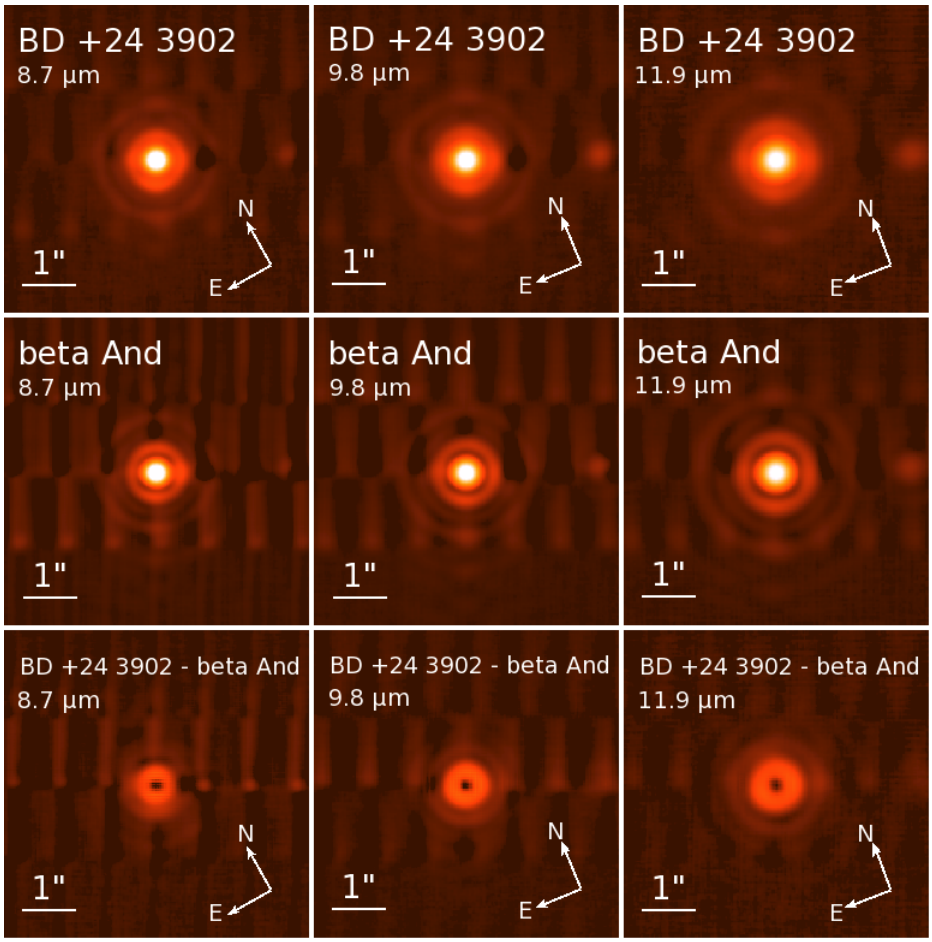

Figure A.4 – MIRAC4 images of BD +24 3902 before and after PSF subtraction. The directions to North and East are indicated. The pixel scale is 0.027″ pix^{-1}.

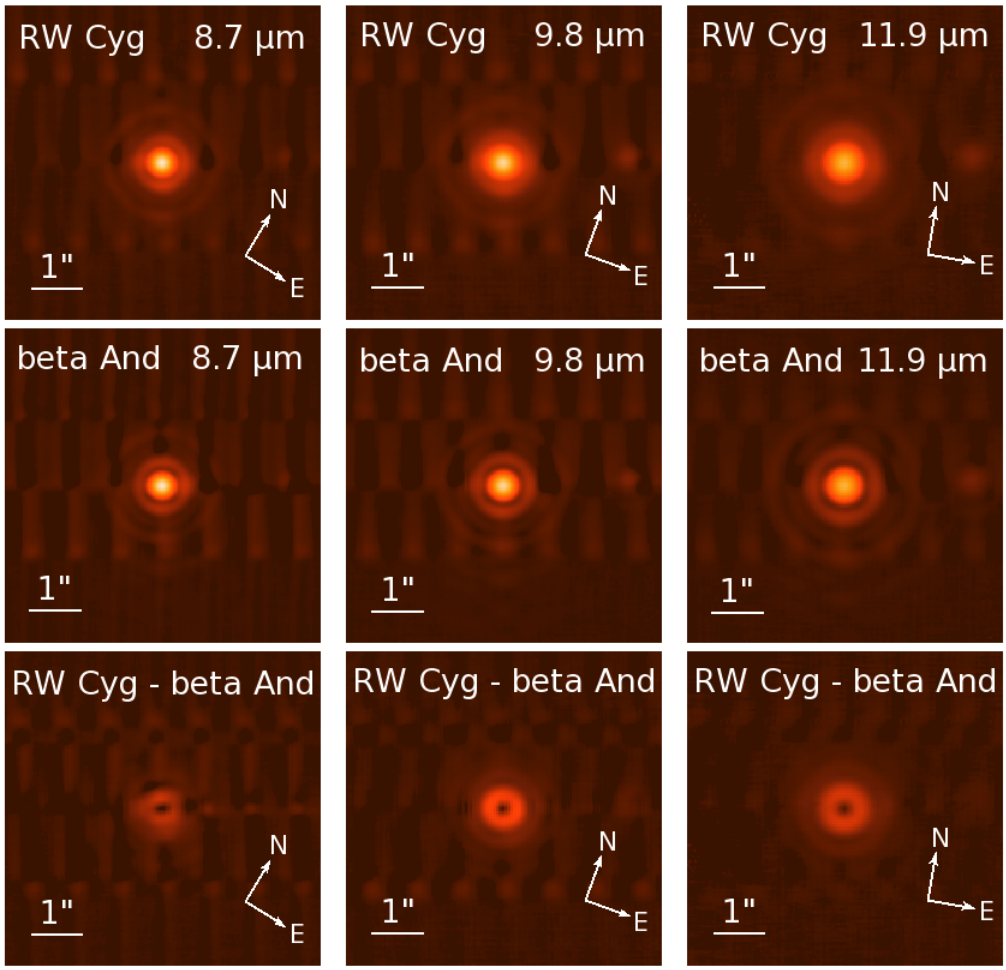

Figure A.5 – MIRAC4 images of RW Cyg before and after PSF subtraction. The directions to North and East are indicated. The pixel scale is 0.027″ pix^{-1}.

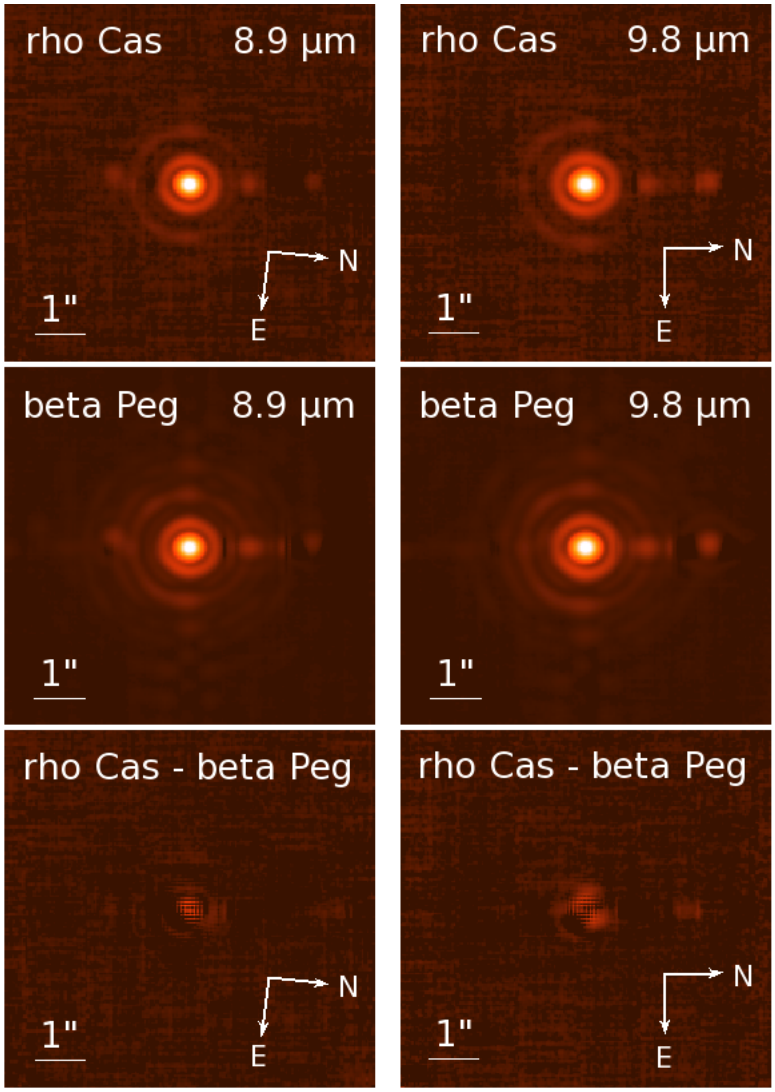

Figure A.6 – MIRAC4 images of ρ Cas before and after PSF subtraction. The directions to North and East are indicated. The pixel scale is 0.037″ pix^{-1}.

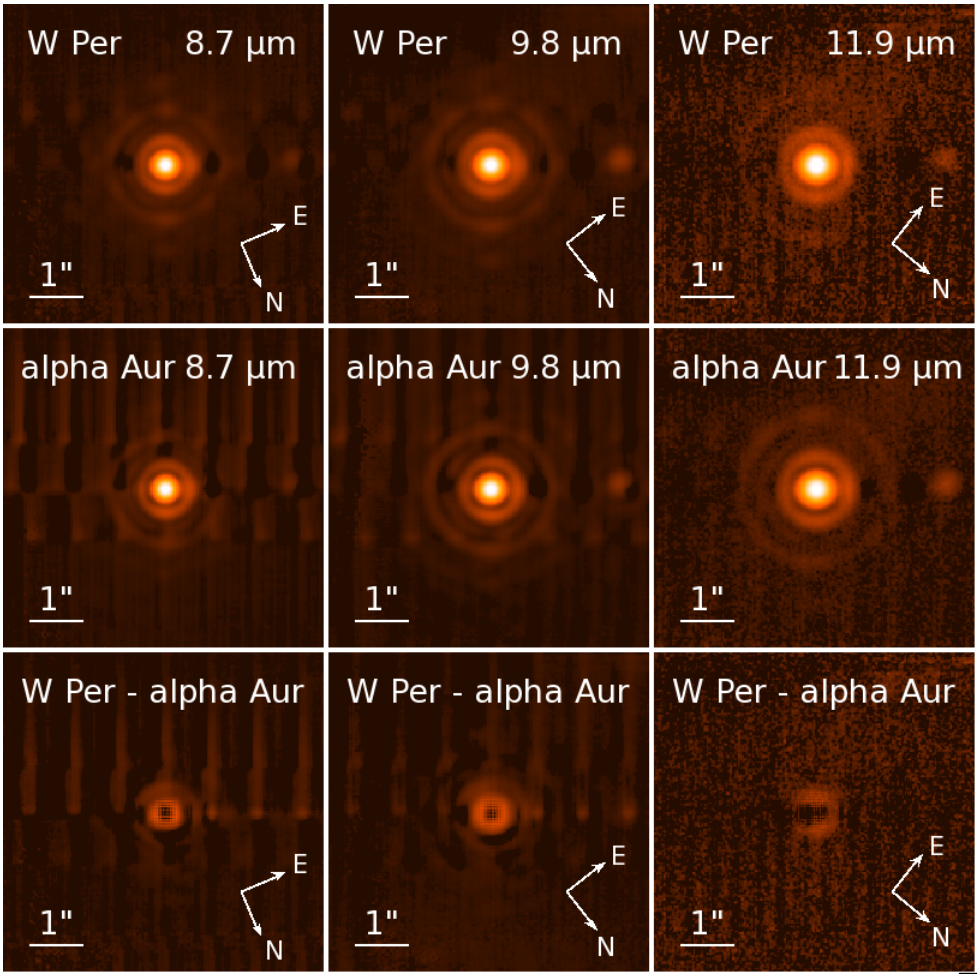

Figure A.7 – MIRAC4 images of W Per before and after PSF subtraction. The directions to North and East are indicated. The pixel scale is 0.027″ pix^{-1}.